

Summer 7-7-2017

A MULTISCALE MODELING STUDY OF THE MAMMARY GLAND

Joseph D. Butner
University of New Mexico

Follow this and additional works at: https://digitalrepository.unm.edu/bme_etds

 Part of the [Cancer Biology Commons](#), [Developmental Biology Commons](#), [Disease Modeling Commons](#), and the [Other Biomedical Engineering and Bioengineering Commons](#)

Recommended Citation

Butner, Joseph D.. "A MULTISCALE MODELING STUDY OF THE MAMMARY GLAND." (2017).
https://digitalrepository.unm.edu/bme_etds/15

This Dissertation is brought to you for free and open access by the Engineering ETDs at UNM Digital Repository. It has been accepted for inclusion in Biomedical Engineering ETDs by an authorized administrator of UNM Digital Repository. For more information, please contact disc@unm.edu.

Joseph D. Butner

Candidate

Biomedical Engineering

Department

This dissertation is approved, and it is acceptable in quality and form for publication:

Approved by the Dissertation Committee:

Dr. Andrew Shreve, Chairperson

Dr. Vittorio Cristini

Dr. Zhihui (Bill) Wang

Dr. Jeffrey Brinker

**A MULTISCALE MODELING STUDY OF THE MAMMARY
GLAND**

Using mathematical modeling and computer simulation to
study the roles of cell phenotypic dynamics and molecular
signaling in the pubertal end bud and postmenopausal DCIS
initiation

by

JOSEPH D. BUTNER

B.S., Mechanical Engineering, University of New Mexico, 2008

M.S., Mechanical Engineering, University of New Mexico, 2012

M.S., Biomedical Engineering, University of New Mexico, 2016

DISSERTATION

Submitted in Partial Fulfillment of the
Requirements for the Degree of

**Doctor of Philosophy
Biomedical Engineering**

The University of New Mexico
Albuquerque, New Mexico

July, 2017

DEDICATION

To my parents, who always encouraged me to pursue education and chase my dreams,
and to my wife Elya, your patience, understanding and encouragement has been
invaluable through this journey.

ACKNOWLEDGEMENTS

I would like to express my sincere gratitude to Dr. Zhihui Wang and Dr. Vittorio Cristini (University of Texas Health Science Center at Houston) for their excellent research guidance and financial support throughout this process. I would also like to thank Dr. Andrew P. Shreve and Dr. C. Jeffrey Brinker (University of New Mexico), Dr. Michael Lewis and Dr. Jeffrey Rosen (Baylor College of Medicine), Dr. John Lowengrub (University of California, Irvine), and Dr. Yao-Li Chuang (California State University, Northridge) for consultation in their areas of expertise. This research has been supported in part by the National Science Foundation (NSF) Grants DMS-1562068 (Z.W., V.C.), DMS-1716737 (Z.W., V.C.); the National Institutes of Health (NIH) Grants 1U01CA196403 (Z.W., V.C.), 1U01CA213759 (Z.W., V.C.), 1U54CA149196 (Z.W., V.C.), and 1U54CA151668 (V.C.); the Rochelle and Max Levit Chair in the Neurosciences (V.C.); the University of Texas System STARS Award (V.C.); the University of New Mexico Cancer Center Victor and Ruby Hansen Surface Professorship in Molecular Modeling of Cancer (V.C.); and the Houston Methodist Research Institute (V.C.).

A MULTISCALE MODELING STUDY OF THE MAMMARY GLAND

Using mathematical modeling and computer simulation to study the roles of cell phenotypic dynamics and molecular signaling in the pubertal end bud and postmenopausal DCIS initiation

By

Joseph D. Butner

B.S., Mechanical Engineering, University of New Mexico, 2008

M.S., Mechanical Engineering, University of New Mexico, 2012

M.S., Biomedical Engineering, University of New Mexico, 2016

Ph.D., Biomedical Engineering, University of New Mexico, 2017

ABSTRACT

Multiscale, hybrid computer modeling has emerged as a valuable tool in the fields of computational systems biology and mathematical oncology. In this work, we present an overview of the motivations for, and development and implementation of, three hybrid multiscale models of the mammary gland system and early stage ductal carcinoma in situ (DCIS) in the gland. Pubertal mammary gland development was described first using a two-dimensional, lattice-based hybrid agent-based model description of the mammary terminal end bud (TEB), and then with a three-dimensional lattice-free TEB model. Both models implement a discrete, agent-based description of the cell scale, and a continuum, finite element method description of tissue scale spatiotemporal molecular profiles, which

are explicitly linked into a hybrid model. This lattice-free pubertal development TEB model was then transitioned into a post-menopausal early stage DCIS model, used for study of the phenotypic dynamics and molecular signaling disruptions involved in development of the DCIS tumor mass. Both TEB and DCIS models implemented simplified, literature-based cellular phenotypic developmental hierarchies and endocrine and paracrine signaling pathways. All models provided valuable insights into the effects of these aspects on the development of both the healthy gland and the pre-invasive DCIS cancer state, and results from model outputs were found to be within literature supported ranges. Cells of both healthy and cancerous phenotypes were found to be sensitive to changes in molecular signaling intensities and phenotypic hierarchies, which played an important part in overall development in both cases, with all cases demonstrating a greater effect of upstream estrogen paracrine signaling relative to the downstream AREG-FGF epithelial to stromal pathway also tested. Here, we provide detailed descriptions of these studies and results, as well as other useful discoveries, and also an overview of the modeling approaches, techniques, and rationale for their specific designs and implementations.

TABLE OF CONTENTS

LIST OF FIGURES	xii
LIST OF TABLES	xiv
CHAPTER 1 INTRODUCTION	1
Mathematical Modeling Approaches	3
Discrete Modeling Methods	5
Continuum Modeling Methods	11
Hybrid Modeling Methods	14
Works Cited, Chapter 1	18
CHAPTER 2 OVERVIEW OF MODELS PRESENTED	23
Modeling the Mammary Terminal End Bud	24
Two-Dimensional TEB Model	25
Three-Dimensional TEB Model	27
Modeling Ductal Carcinoma in Situ	29
Future Directions Overview	30
Works Cited, Chapter 2	32
CHAPTER 3 A MODELING APPROACH TO STUDY THE NORMAL MAMMARY GLAND GROWTH PROCESS	33

Abstract.....	34
Introduction	34
Methods	37
Computational Domain	37
Continuum Component	38
Discrete Component.....	39
Model Parameters.....	40
Results and Discussion	41
Symmetric vs. Asymmetric Division	41
Differentiation	43
Acknowledgements	44
Works Cited, Chapter 3	45
CHAPTER 4 A HYBRID AGENT-BASED MODEL OF THE DEVELOPING MAMMARY TERMINAL END BUD	47
Abstract.....	49
Introduction	50
Hybrid Modeling Methods	56
Continuum partial differential equation component	57
Discrete agent-based modeling component	60

Results	64
Cell cycles before differentiation	66
Symmetric vs. asymmetric division	67
Signaling Thresholds.....	69
Cell types in each region	72
Discussion.....	74
Acknowledgements	79
Works Cited, Chapter 4	81
 CHAPTER 5 DEVELOPMENT OF A THREE DIMENSIONAL, LATTICE-FREE MULTISCALE MODEL OF THE MAMMARY TERMINAL END BUD	 85
Abstract.....	86
Introduction	87
Methods	88
Continuum Scale	88
Discrete Scale.....	90
Hybrid Modeling Methods.....	91
Results and Discussion	93
Acknowledgements	97
Works Cited, Chapter 5	98

CHAPTER 6 DEVELOPMENT OF A THREE DIMENSIONAL, MULTISCALE AGENT-BASED MODEL OF DUCTAL CARCINOMA IN SITU	100
Abstract.....	101
Introduction	101
Methods	103
Discrete Scale.....	103
Continuum Scale	105
Hybrid Modeling Method	106
Results and Discussion	109
Acknowledgements	112
Works Cited, Chapter 6	113
CHAPTER 7 A MULTISCALE, AGENT-BASED MODEL OF DUCTAL CARCINOMA IN SITU	115
Abstract.....	115
Introduction	116
Methods	124
Continuum Methods.....	124
Discrete Methods	130
Hybridization of Models	136

Results	137
Establishment of Baseline Values	138
The Number of EMT-generated Stem Cells in the CSC Niche has Minimal Effect on DCIS Invasion Rates	139
Early-stage DCIS Invasion Occurs in Two Distinct Growth Regimes.....	141
DCIS Axial Invasion Rates are Consistent over all Duct Sizes Tested	143
Necrosis Acts as a Hypoxia Relief Mechanism	145
Molecular Signaling Effects.....	147
Discussion.....	151
Acknowledgements	156
Works Cited, Chapter 7	157
CHAPTER 8 CONCLUSION AND FUTURE DIRECTIONS.....	161

LIST OF FIGURES

Figure 3.1: Cellular lineages and estrogen and AREG signaling pathways	35
Figure 3.2: Computational domain	37
Figure 3.3: Parameter analysis	42
Figure 4.1: Cellular phenotypic hierarchy and signaling pathways	52
Figure 4.2: TEB and schematic of computational domain	56
Figure 4.3: Agent phenotype decision flowchart	63
Figure 4.4: Effects of proliferation cycles before differentiation	65
Figure 4.5: Progenitor population within the TEB with different symmetric proliferation probabilities.....	68
Figure 4.6: Ductal elongation growth rates with 2x and 3x proliferation cycles before differentiation with symmetric proliferation probability perturbation	69
Figure 4.7: Effects of synchronized $\pm 10\%$ estrogen and AREG signaling threshold variation on ductal elongation rates	70
Figure 4.8: Effects of independent $\pm 10\%$ signaling threshold variation on ductal elongation rates	72
Figure 4.9: Cell types in each region for two and three cycles before differentiation.....	73
Figure 5.1: A schematic of the 3D computational domain of TEB	89

Figure 5.2: Cellular phenotypic types, differentiation pathways and signaling	92
Figure 5.3: Sample simulation output	94
Figure 5.4: Ductal elongation per cell cycle/time step	95
Figure 6.1: Computational domain	105
Figure 6.2: A section of simulated mature mammary gland duct.....	108
Figure 6.3: Total DCIS cell count in the duct cavity over time	109
Figure 6.4: DCIS axial invasion extent.....	110
Figure 7.1: Computational domain, cell phenotype hierarchy, and signaling pathways	120
Figure 7.2: Examples of continuum and discrete model components	125
Figure 7.3: Agent decision flowchart.....	131
Figure 7.4: Effects of variation in CSC count within the EMT-generated niche on DCIS invasion.....	140
Figure 7.5: DCIS cell population expansion occurs over two distinct regimes	142
Figure 7.6: Effect of duct diameter on DCIS axial duct invasion extent over time...	144
Figure 7.7: Necrosis acts as a partial relief mechanism for hypoxia	146
Figure 7.8: Effects of molecular signaling thresholds on DCIS axial invasion	148
Figure 7.9: Example simulation results with signaling effects	149

LIST OF TABLES

Table 3.1. Key Model Parameters.....	40
Table 4.1 Baseline values of key model parameters.....	79
Table 7.1 Important model parameter baseline values	155

CHAPTER 1

Introduction

Over the last decades, mathematical modeling has emerged as a valuable addition to the more traditional tools used in the study and characterization of biological systems. Traditional research methods involve the manipulation of living systems (cells, tissues, or even whole organisms) in clever ways to gain insights into the underlying mechanisms of their functionality, but these methods are often limited by the wet-lab tools used for experimental design and characterization, ethical concerns, and time and monetary restrictions, as well as complications within the living systems themselves. Nonetheless, traditional methods remain integral in the study and characterization of biological systems, as the biological system must remain the starting point for all study, and any new research methods must take inspiration from, and be validated against, data obtained from such methods.

Taking inspiration from published wet-lab research, mathematical modeling strives to generate equation-based descriptions of biological systems, often yielding many new and interesting insights that may not be obvious through bench-level experiments. Biological systems are bound by the same physical laws as non-biological systems, many of which have been well characterized and described mathematically through efforts in other fields. Indeed, the laws of physics, thermodynamics, mechanics, and chemistry (among others) are all intimately involved in the processes carried out within cells, tissues, organs, and whole-organism biological systems. Mathematical descriptions of these physical processes, though historically developed for solving problems in non-biological fields, have now been shown to be adaptable to biological descriptions as well.

Mathematical modelers have often strived to describe and quantify processes that are not easily determined through wet lab techniques. Inherently, the details of mechanisms within biological systems are often difficult to characterize, as they are 1) incredibly complex, and 2) occur on extremely small spatial and temporal scales. These limitations in themselves do not provide insurmountable obstacles to experimental study, but their occurrence within a living system further compounds these difficulties, often necessitating the invention of clever and novel experiments and laboratory techniques, which the experimentalist uses to draw out the desired information. Mathematical modeling has proven to be a useful addition to these methods, often elucidating the underlying mechanisms driving the behaviors observed at the benchtop, and providing information that is not easily obtainable from other methods.

More intriguing still is the potential for mathematical descriptions of biological systems to be used as predictive tools, especially in clinical settings. The underlying equations involved in these descriptions depend on parameters or variables whose values are measured quantitatively from the biological system. When correctly formulated, a mathematical description of a physical phenomenon does not change in its basic form – it describes all possible scenarios within the bounds of the assumptions involved in its derivation, dependent on the variable values it receives as inputs. By inputting correctly calibrated parameters that apply the governing mathematical description to a specific circumstance, the equation (or set of equations) may be tuned from a general, broadly applicable description to one specific to a particular organism, thereby allowing a general mathematical framework to describe many individualized scenarios.

To this end, mathematical modeling of biological systems offers the potential of an exciting new tool: the ability to predict the outcome of a set of system inputs, based on sound scientific principles and fundamental laws, in a quantified and exacting way. Accurate prediction reduces the need for trial and error in experimental and clinical studies. In the lab, researchers can readily identify the most important and promising experiments to conduct, reducing material and time costs. In the clinic, physicians can optimize treatment strategies, individualized for their patients, simultaneously reducing costs, treatment time, and patient, while increasing the likelihood of successful treatment outcome.

In this work, we will delve into the details of how mathematical models are developed and implemented, the underlying reasoning behind the selection of modeling approaches to describe the system of interest, and the motivations for doing so, all with a focus on modeling cancer and developmental biology. We will then look in detail at new models developed by the author that provide interesting insights into cell signaling and phenotypic contributions into the pubertal development of the human mammary gland, as well as in the post-menopausal initiation of a pre-invasive breast cancer, ductal carcinoma in situ (DCIS).

I. Mathematical Modeling Approaches

The selection of an appropriate mathematical modeling method is usually determined by the needs and desired outcomes of the modeler. Commonly, most modeling approaches of complex phenomena are computationally intensive, and are thus implemented in a computer-based environment, taking advantage of modern computing

resources. In biology, this type of computer-based modeling is an approach referred to as *in silico* (contrasting with the *in vivo* and *in vitro* methods of traditional experimental biology). Just like at the benchtop, experimental design and chosen methods *in silico* must be carefully examined and prioritized to design an experiment with the potential to provide the modeler with the desired information. Without the proper choice of modeling approach and implementation, the modeler cannot hope to gain useful information and. *In silico*, this choice is often accomplished through intelligent assessment of mathematical modeling techniques, the resolution (scale) the model implements, and the biological aspects deemed most important for inclusion to the model.

Generally speaking, the resolution of the model must match the resolution of the biological processes and/or the effects the modeler intends to study. For example, if a modeler desires information about the interplay of cell-cell interaction and dynamics of population phenotypic shifts, the implemented model should include these descriptions, at a cell-by-cell resolution. Models may even delve down to smaller and more refined scales, as is the case with the mathematical prediction of protein conformation based on a simulated reconstruction of the amino acid sequence at an atomic resolution (approaches include homology modeling, protein threading), or the study of enzyme/receptor-substrate interaction. When individual entities of interest are described explicitly and uniquely in a model, it is referred to as a discrete model. Conversely, modeling descriptions of large numbers of entities often employ coarser descriptions, commonly through a mathematical description of distributions of the entities of interest (atoms, molecules, cells, etc.) across a large spatial or temporal scale. These models accumulate information about large numbers of discrete entities into a single distribution function, whose behavior is described

mathematically. Such models are known as continuum models, and are often employed when a single-entity resolution description is either not desired, necessary, or computationally feasible. Often, discrete and continuum methods are combined together into a single multiscale or hybrid model that combine the best aspects of both to mitigate the weaknesses of each. For the interested reader, a more in-depth discussion of hybrid models than presented here may be found in [1-7].

i. Discrete Modeling Methods

Atoms, molecules, cells, and other building blocks of biological systems are, at a fine enough resolution, composed of discrete entities. This observation naturally leads to discrete descriptions, where each discrete entity is represented as an agent, in a method known as agent-based modeling (ABM). These methods are likely the most intuitive descriptions, as they are often based on observation, and mirror the structure seen by an observer in a modeling replication of the system. Indeed, rendered images of these models and their simulation results may resemble visually observable biological systems in many ways, providing the model's designer and users easily interpretable and understandable observations and insights. The model designer must choose the resolution implemented in the model, based on the features to be studied and the output needed to evaluate or use the model result. Generally speaking, this resolution and the modeling technique(s) implemented are chosen to be the coarsest possible without sacrificing the resolution needed for the intended study. For example, a model designed to study the dynamics of a cell population might logically choose the cells themselves as the finest resolution to be explicitly described in a discrete manner. Within this example cell population, sub-cellular

scale factors (for example, oxygen consumption or the genetic factors and biochemical mechanisms involved in cell phenotype selection and expression) are then lumped together (e.g. as a per volume or per surface area implementation, or through other approximations) into a “net” cell contribution into the model. In this way, a cell in this example may still express its phenotype and conduct cellular respiration, but the model avoids the intensive and often unnecessary computational costs of describing each molecule, organelle, and chemical reaction within the cell.

This example points to an important aspect of discrete modeling design: what should the modeler choose to incorporate into the model? While there is not a consensus on one standard template of what makes a “good” model (nor should there be, due to the wide range of modeling techniques and uses), generally the features included must describe, at least, the entities the modeler desires to study (in the case of the work presented here, the cells in the tissue), the most important literature-supported biologically relevant factors at this scale (in the case of individual cells, this is often oxygen or glucose, but may also include other factors), as well as other crucial aspects specific to the entity being studied (including phenotypic hierarchies, hormonal endocrine and paracrine signaling mechanisms, etc.). In all cases, the modeler identifies the most relevant factors to the intended study (e.g., the factors that the literature supports as the most influential in the behavior to be studied), and chooses these to incorporate into the model. Inherent in this decision is the exclusion of some (or even many) biological factors. In fact, the system the modeler wishes to study may not even be fully characterized biologically, limiting any modeling descriptions to the current threshold of knowledge on the system. Often, this limitation means that even the most complete modern modeling effort could not possibly

implement a complete description of the underlying biology! These considerations make the modeler's selection of factors to be included of utmost importance, as these are the factors that may influence the model and the results obtained. Overall, the model design must be done carefully in order to achieve biologically relevant results. Within discrete modeling methods, there are many well-established techniques, including lattice-based [8], lattice-free [7, 9], Cellular Potts [10], lattice gas/Boltzmann [11, 12], and subcellular methods.

Despite the simplified descriptions implemented in mathematical models, the inherent complexity of the modeled biological system of interest can quickly become sophisticated. A cell in a model must contain, at minimum: geographic coordinates, a cytoplasmic volume, a phenotype, a method of perceiving the passage of time, a way of determining the surrounding conditions within its microenvironment, a method of making decisions based on its characteristics and observed behaviors in living specimens, and an ability to implement the outcomes of its decisions. Describing even a simple action by a single cell can result in a complex calculation in a discrete model. For example, a cell in interphase (G phases) increases its cytoplasmic volume over time, expanding the plasma membrane and increasing the total cell volume and surface area. If this cell is in a cell population with adjacent neighbors, this expansion is not autonomous – its neighbors must move or deform to accommodate this volume change. This response can trigger a cascade, where they in turn deform or displace their neighbors, ultimately resulting in the disturbance of many cells. In a living system, the laws of physics “solve” this problem automatically, and the system will naturally adjust on its own; but in a model, these processes must be represented mathematically and explicitly solved.

In practice, the complex problem of movement of a discrete entity (continuing our example from the previous paragraph, a cell) is solved by either restricting agent movement to a lattice (like a chess board, where the agent may move from the center of one square to a neighboring square, but not to positions in between, which simplifies the calculation at the cost of providing a somewhat artificial agent distribution), or through a Newton's laws description of the physics of agent interaction, allowing agents to move based on the forces of interaction through solution of a series of linked equations. In the lattice-based approach, a lattice space might hold one cell (or more specifically, a coordinate associated with the cell, commonly its center of mass, may be at the lattice coordinate), and a cell may only move to an adjacent lattice coordinate. In this way cells may not occupy any arbitrary coordinate within the modeled area, but are restricted to a finite set of points within the computational domain. Thus, in this approach, if a cell moves to an adjacent lattice point, it must displace the cell that was already occupying that location, should there be a cell there. The result is often a displacement cascade, where cells continue to be displaced until one moves into a free lattice coordinate or out of the computational domain. If each lattice cell is the size of a mature cell, then the effects of a daughter cell growing in interphase will not be observed, as the cell simply grows to occupy the entire lattice location. However, some models overcome this limitation by defining the lattice to be smaller than a cell, effectively refining the model's resolution, and allowing for observations of cell movement on a scale smaller than a cell diameter. If the modeler wants to see the effects of cell growth, such a refined lattice must be implemented (at a potential cost of more complicated calculations of total cell movement). If cell growth is not of interest in the model, then the larger lattice can be used with the approximation that each cell is the size

of an adult cell. This spatially less refined model may be a reasonable approximation, since the cell will grow to this size at the end of interphase and the details of how it gets there may not be of interest to the study.

This simple example shows one way a model may be customized to the specific questions the model is designed to address, and the potential tradeoffs the designer makes for increased complexity. Relative to a coarser lattice, a finer lattice may be more computationally complex, or require more calculations per time step, to solve the discrete movement of all modeled entities. This design consideration may be even avoided all together by removing the lattice-based movement restriction, but at an even greater computational cost, both in terms of algorithm complexity and in time to solve the system. In short, even the simple action of a cell growing presents a potentially complex problem. Fortunately, as we have seen, the modeler possesses several options to address the problem, but must make an informed choice well-suited for the particular applications of interest.

In a tissue, cells can also divide, lyse, die, and enter quiescence or senescence (among other physical changes), and there are often many thousands of cells within a model (all of which may do one or more of these actions each time step). This range of behavior means that the process of tracking cell movements quickly explodes into a very complicated problem. Each time a modeler adds a new parameter, the calculations increase in complexity. Even the example given above of cell-cell interaction physics was relatively simplified – in fact, cells can also adhere to each other, adhere to the basement membrane or extra cellular matrix, experience conformational remodeling through cytoskeletal actions, and have many other physical effects on and in response to their surroundings. To incorporate each one of these behaviors into the model may require the addition of one or

more equations per cell, or per contact point between a cell and the entities it interacts with (possibly as many as 10+ contact points per cell in 3D configurations, applied to each of thousands of cells).

Despite these challenges, modelers have made great accomplishments through development of complex and interesting descriptions of biological systems. Gerlee and Anderson used ABM to yield interesting insights into the evolutionary dynamics of tumor growth and the interplay between cells in the tumor and their microenvironment [13-15]. Wynn *et al.* observed the dynamics between leading metastatic cancer cells and the resulting metastatic movement of contacting follower cells [16], which accurately reproduced the observed biological behavior [17]. In each case, the ABM description of the cell population showed successful replication of the biological system, and provided interesting insights into the mechanisms involved. Wang and Deisboeck *et al.* implemented an ABM to explore the roles of the ERK and EGFR pathways in non-small cell lung cancer, and observed that an interplay between the EGFR-ERK pathway and microenvironmental factors resulted in a phenotypic transition that favored a migratory phenotype over a proliferative phenotype [18]. This work was later expanded to include the TGF β pathway, requiring a system of 26 ordinary differential equations (ODEs), and demonstrating that ERK and ERK+TGF increased sensitivity to microenvironmental-induced invasive phenotype transition [19]. Simulating the cell signaling EGFR-ERK and TGF β pathway interactions required more than just the discrete agents, (as do some other models mentioned here); the mathematical description of the movement of these signaling molecules between cells and throughout the computational domain is often best described using continuum methods.

ii. Continuum Modeling Methods

The distribution of a molecule of interest within a tissue, organ, or even at a system-wide scale is often better suited to an equation-based description, as are large (i.e. tissue or organ scale) distributions of cells when a cell-level resolution is unnecessary. These models are known as continuum descriptions, and are often implemented using one or more ordinary or partial differential equations (ODEs, PDEs). Continuum descriptions are well suited for applications when the spatiotemporal description of a quantity of interest is desired, but describing each individual within the quantity may not be useful or computationally feasible. For example, oxygen or nutrient distributions (described in both space and time) within a system (tissue, organ, etc.) are often described as continuums, as knowledge of the exact location of each molecule is often superfluous, and the large number of molecules within the system would introduce significant and unnecessary computational costs (and, in fact, may not be possible at all, depending on the size and scale of the system).

Pharmacokinetic (PK) and pharmacodynamics (PD) methods (or, when combined into a single model, referred to as PK/PD) are commonly included as important parts of continuum modeling, as they help link the continuum field to the underlying biology; these relationships are crucial to the continuum modeling approach. For example, a mathematical solution describing the continuum distribution of a molecule of interest may have limited scientific applications in and of itself, but, when the solution is linked quantitatively to the overlying biological system in a way that it may influence and be influenced by the system, it becomes a more powerful modeling tool; this is the role of PK-PD. Pharmacokinetics

refers to the ways in which the body (or system) affects the drug molecules (i.e. absorption and distribution, metabolism, etc.); conversely, pharmacodynamics describes the ways the drug affects the body (for example, in the case of chemotherapy, this might refer to the effective drug induced killing of tumor cells) [20, 21]. As many of these effects are system or tissue wide (although noting that PK and PD methods are not restricted to this scale, and may describe small regions as well), often they may be described using temporal, but not necessarily spatial, mathematical descriptions. Simply put, PK commonly describes the time course of the drug concentration over time in the system, while PD describes drug concentration vs. its effectiveness. When combined, PK-PD provides a description of the drug effect over time [22]. The link between dosage and response is often complicated, and there may exist various degrees of ambiguity in the understanding of the underlying biological mechanisms that link the drug dosage with system response. To account for this challenge, PK-PD models are usually either *empirical*, where they provide good correlation between dosage and response without including the underlying biology, or *mechanistic*, where the underlying biological methods that link dosage and response (as currently understood, or as known to be most important to the system) are explicitly and quantitatively described mathematically, providing a biological mechanism-based link between model input and output. Whenever possible, mechanistic models are usually preferred to empirical models, as they provide a more complete description of the underlying biology, as well as provide useful tools to study the effects of changes in these biological mechanisms. For the interested reader, more information on PK-PD methods and exciting accomplishments in the field may be found in [21, 23].

Models employing continuum methods have made great strides in elucidating quantitative information and insights into the underlying mechanisms and causal links in biological systems. Modelers have successfully described solid tumors as continuums [24], both to study the growth of solid tumors and the PK of tumor response to chemotherapeutic treatment [25, 26]. PK-PD methods have yielded insights into anticancer treatment with antibody-drug conjugates, both in HER2-overexpressing BT474 murine xenografts [27] and Hodgkin's lymphoma patients [28]. In fact, the well-known Norton-Simon hypothesis (that cancer treatment efficacy may be increased by increasing dose intensity to reduce cancer regrowth between treatments) was generated using PK-PD methods [29, 30], and later validated in clinical trials [30]. Other notable PK-PD modeling accomplishments include modeling treatment of acute lymphoblastic leukemia [31, 32], drug interactions [33], and the effects of immune-stimulatory agents [34]. Continuum methods have demonstrated the ability to predict the outcome and treatment efficacy of a patient-specific chemotherapy regimen based on a single time point clinical measurement, using a single but powerful equation in closed form [35]. Notably, the model in [35] has been demonstrated to transcend tumor type and drug treatment, demonstrating its predictive ability in vivo using patient data (colorectal cancer metastatic to the liver and glioblastoma multiforme [35]). Continuum modeling has even been shown to be adaptable to novel, cutting-edge cancer therapies. Recently, PK-PD modeling was successfully implemented to describe and predict drug uptake when delivered using a functionalized, targeted, mesoporous protocell delivery mechanism [36] to deliver chemotherapy agents (cisplatin and 5-fluorouracil, doxorubicin (DOX), and gemcitabine, respectively) to HCC, breast cancer MCF-7, and pancreatic adenocarcinoma PANC-1 cells in vitro [37].

iii. Hybrid Modeling Methods

The mechanistic links between model inputs and outputs often span many scales in time and space. Drugs are often delivered intravenously, and are quickly distributed organism-wide through the circulatory system. Drugs and other intravenously delivered treatment vessels must leave circulation and enter the tissue where they are intended to act, diffuse through the tissue to where they are needed, and interact with the cells of interest at a cell or even molecular scale. This wide range of processes (in both space and time) is poorly suited to description by only one modeling method; hence the development of hybrid modeling methods, which combine and explicitly link modeling methods of multiple scales into a more complete system description. Through hybridizing multiple methods, modelers may tease out an optimal combination of the best aspects of each, while using the strengths of one method to compensate the weakness of another [38]. For example, hybrid models are often developed that describe tissue scale parameters (e.g. molecular distributions) as continuums, and cell-level scales with agent-based methods, where each cell is described individually. By explicitly linking the scales through mathematically based feedback systems, the two scales are hybridized into a single model. This approach provides a finer level of detail, resulting in what is often considered to be a more complete (and, hopefully, correct) description of the system.

Hybrid methods are also implemented to overcome restrictions and limitations encountered in the form of finite computer resources and computational power. Any computing system is limited in terms of number of computations per time. Inherently, this fact imposes a limitation on the resolution any model may contain, and thus a modeler must

trade a finer resolution (in either time or space) for a smaller total modeled system. As a general rule, the spatial size of the modeled components determines the size of the total system modeled, as the total system is a sum of parts. If a hypothetical modeling system implemented on a particular computer can model a total of 1,000 parts, then it may be used to model a system of 1,000 atoms (perhaps a single molecule, and maybe even the immediately surrounding solvent molecules), or the same model (albeit with far different rules) may be used to describe a species population that represents each individual organism as a unique entity, and thus could describe 1,000 total individuals. This limitation in maximum individual “pieces” within the model has resulted in another kind of hybrid model: one that describes different regions of the same parameter using different, hybridized methods.

A common example of this method is solid tumors, which often consist of a fast-growing population on the outer edge, where oxygen and nutrients are plentiful (referred to as the *viable rim*), and an inner core which consists of cells which are much less active due to nutrient and/or oxygen restrictions (hypoxia), and may even be dead (necrotic) due to prolonged exposure to resource-limited conditions. Further, depending on the size of the solid tumor, the total cell population in the viable rim may be small relative to the population in the other regions. If the modeler wishes to gain insights into the cell-scale invasive behaviors in the viable rim, his or her model might be greatly hindered by calculating a complete description of each dead cell in the necrotic core for every time point. Modelers may work around this limitation by describing the total cell population with a hybrid approach: describing the viable rim as unique cells, through an agent-based model approach, while describing the dense center region of the tumor as a continuum.

These descriptions are hybridized with a set of rules governing when a particular cell (agent) transitions to become part of the continuum (or vice-versa) [39]. This approach has been used in other clever ways, such as a discrete description of vasculature invasion (angiogenesis) through tissue (represented as a continuum) in a collaborative effort by Frieboes, Lowengrub, and Cristini *et al.* [40-42].

The complex interplay of factors involved in cancer initiation, development, and treatment often span many scales in space and time, and are thus well-suited to hybrid modeling methods. Cancer cells profoundly affect their microenvironment, including through acidosis from glycolytic metabolism [43] and extracellular matrix (ECM) remodeling (often through acidosis-induced ECM degradation), both of which may impact phenotypic selection within, and metastasis out of, the tumor [44]. Gattenby *et al.* have extensively explored the complex interplay of glycolysis and acidosis within the tumor environment using hybrid ABM techniques [45, 46], demonstrating the effects of acidosis-induced phenotypic selection to a phenotype that further decreased microenvironment pH, further favoring the acid-resistant phenotype and perpetuating an invasive phenotype. Gerlee and Anderson saw a similar effect in a different model that also included the effects of ECM [13], where they observed the ECM resisted metastasis out of the acidic environment, again perpetually favoring the phenotypic selection to an acid resistant phenotype. In yet another model, Anderson further demonstrated the importance of cell-ECM interactions in cancer cell invasiveness and metastasis [47]. Other modeling work has further elucidated the complex interplay of tumor microenvironment and phenotypic selection, both through random selection [48] and neural network governed microenvironment-directed evolutionary dynamics [13-15]. Notable hybrid modeling in

cancer applications includes the study of tumor angiogenesis [49-51], molecular signaling in the tumor environment [52-55], cancer stem cells [56-59], and cancer treatment [54] through ionizing radiation [60] and post-surgical adjuvant radiation therapy [61], chemotherapy [62], and even the immune response to tumors as induced through anticancer vaccines [63, 64].

II. Works Cited, Chapter 1

1. Deisboeck, T.S., Wang, Z., Macklin, P., and Cristini, V., *Multiscale Cancer Modeling*. Annual review of biomedical engineering, 2011. **13**: p. 10.1146/annurev-bioeng-071910-124729.
2. Johnson, D., McKeever, S., Stamatakos, G., Dionysiou, D., Graf, N., Sakkalis, V., Marias, K., Wang, Z., and Deisboeck, T.S., *Dealing with Diversity in Computational Cancer Modeling*. Cancer Informatics, 2013. **12**: p. 115-124.
3. Lowengrub, J.S., Frieboes, H.B., Jin, F., Chuang, Y.L., Li, X., Macklin, P., Wise, S.M., and Cristini, V., *Nonlinear modelling of cancer: bridging the gap between cells and tumours*. Nonlinearity, 2010. **23**(1): p. R1-R9.
4. Rejniak, K.A. and Anderson, A.R.A., *Hybrid Models of Tumor Growth*. Wiley interdisciplinary reviews. Systems biology and medicine, 2011. **3**(1): p. 115-125.
5. Schnell, S., Grima, R., and Maini, P.K., *Multiscale Modeling in Biology: New insights into cancer illustrate how mathematical tools are enhancing the understanding of life from the smallest scale to the grandest*. American Scientist, 2007. **95**(2): p. 134-142.
6. Tracqui, P., *Biophysical models of tumour growth*. Reports on Progress in Physics, 2009. **72**(5): p. 056701.
7. Wang, Z., Butner, J.D., Kerketta, R., Cristini, V., and Deisboeck, T.S., *Simulating Cancer Growth with Multiscale Agent-Based Modeling*. Seminars in cancer biology, 2015. **0**: p. 70-78.
8. Butner, J.D., Chuang, Y.L., Simbawa, E., Al-Fhaid, A.S., Mahmoud, S.R., Cristini, V., and Wang, Z., *A hybrid agent-based model of the developing mammary terminal end bud*. J Theor Biol, 2016. **407**: p. 259-70.
9. Butner, J.D., Cristini, V., and Wang, Z., *Development of a Three Dimensional, Multiscale Agent-Based Model of Ductal Carcinoma in Situ*. Conf Proc IEEE Eng Med Biol Soc, 2017. **In Press**.
10. Li, J.F. and Lowengrub, J., *The effects of cell compressibility, motility and contact inhibition on the growth of tumor cell clusters using the Cellular Potts Model*. J Theor Biol, 2014. **343**: p. 79-91.
11. Liu, Y., *A lattice Boltzmann model for blood flows*. Applied Mathematical Modelling, 2012. **36**(7): p. 2890-2899.
12. Motta, S., Castiglione, F., Lollini, P., and Pappalardo, F., *Modelling vaccination schedules for a cancer immunoprevention vaccine*. Immunome Research, 2005. **1**: p. 5-5.
13. Gerlee, P. and Anderson, A.R., *A hybrid cellular automaton model of clonal evolution in cancer: the emergence of the glycolytic phenotype*. J Theor Biol, 2008. **250**(4): p. 705-22.
14. Gerlee, P. and Anderson, A.R.A., *An Evolutionary Hybrid Cellular Automaton Model of Solid Tumour Growth*. Journal of theoretical biology, 2007. **246**(4): p. 583-603.
15. Gerlee, P. and Anderson, A.R., *Evolution of cell motility in an individual-based model of tumour growth*. J Theor Biol, 2009. **259**(1): p. 67-83.

16. Wynn, M.L., Kulesa, P.M., and Schnell, S., *Computational modelling of cell chain migration reveals mechanisms that sustain follow-the-leader behaviour*. J R Soc Interface, 2012. **9**(72): p. 1576-88.
17. Cheung, K.J., Gabrielson, E., Werb, Z., and Ewald, A.J., *Collective invasion in breast cancer requires a conserved basal epithelial program*. Cell, 2013. **155**(7): p. 1639-51.
18. Wang, Z., Zhang, L., Sagotsky, J., and Deisboeck, T.S., *Simulating non-small cell lung cancer with a multiscale agent-based model*. Theoretical Biology & Medical Modelling, 2007. **4**: p. 50-50.
19. Wang, Z., Birch, C.M., Sagotsky, J., and Deisboeck, T.S., *Cross-scale, cross-pathway evaluation using an agent-based non-small cell lung cancer model*. Bioinformatics, 2009. **25**(18): p. 2389-96.
20. Meibohm, B. and Derendorf, H., *Basic concepts of pharmacokinetic/pharmacodynamic (PK/PD) modelling*. Int J Clin Pharmacol Ther, 1997. **35**(10): p. 401-13.
21. Wang, Z., Butner, J.D., Cristini, V., and Deisboeck, T.S., *Integrated PK-PD and agent-based modeling in oncology*. J Pharmacokinet Pharmacodyn, 2015. **42**(2): p. 179-89.
22. Derendorf, H. and Meibohm, B., *Modeling of Pharmacokinetic/Pharmacodynamic (PK/PD) Relationships: Concepts and Perspectives*. Pharmaceutical Research, 1999. **16**(2): p. 176-185.
23. Zhou, Q. and Gallo, J.M., *The Pharmacokinetic/Pharmacodynamic Pipeline: Translating Anticancer Drug Pharmacology to the Clinic*. The AAPS Journal, 2011. **13**(1): p. 111-120.
24. Cristini, V., Lowengrub, J., and Nie, Q., *Nonlinear simulation of tumor growth*. J Math Biol, 2003. **46**(3): p. 191-224.
25. Frieboes, H.B., Edgerton, M.E., Fruehauf, J.P., Rose, F.R., Worrall, L.K., Gatenby, R.A., Ferrari, M., and Cristini, V., *Prediction of drug response in breast cancer using integrative experimental/computational modeling*. Cancer Res, 2009. **69**(10): p. 4484-92.
26. Sinek, J.P., Sanga, S., Zheng, X., Frieboes, H.B., Ferrari, M., and Cristini, V., *Predicting drug pharmacokinetics and effect in vascularized tumors using computer simulation*. J Math Biol, 2009. **58**(4-5): p. 485-510.
27. Wada, R., Erickson, H.K., Lewis Phillips, G.D., Provenzano, C.A., Leipold, D.D., Mai, E., Johnson, H., and Tibbitts, J., *Mechanistic pharmacokinetic/pharmacodynamic modeling of in vivo tumor uptake, catabolism, and tumor response of trastuzumab maytansinoid conjugates*. Cancer Chemother Pharmacol, 2014. **74**(5): p. 969-80.
28. Shah, D.K., Haddish-Berhane, N., and Betts, A., *Bench to bedside translation of antibody drug conjugates using a multiscale mechanistic PK/PD model: a case study with brentuximab-vedotin*. J Pharmacokinet Pharmacodyn, 2012. **39**(6): p. 643-59.
29. Norton, L., *A Gompertzian model of human breast cancer growth*. Cancer Res, 1988. **48**(24 Pt 1): p. 7067-71.
30. Citron, M.L., Berry, D.A., Cirincione, C., Hudis, C., Winer, E.P., Gradishar, W.J., Davidson, N.E., Martino, S., Livingston, R., Ingle, J.N., Perez, E.A., Carpenter, J.,

- Hurd, D., Holland, J.F., Smith, B.L., Sartor, C.I., Leung, E.H., Abrams, J., Schilsky, R.L., Muss, H.B., and Norton, L., *Randomized trial of dose-dense versus conventionally scheduled and sequential versus concurrent combination chemotherapy as postoperative adjuvant treatment of node-positive primary breast cancer: first report of Intergroup Trial C9741/Cancer and Leukemia Group B Trial 9741*. *J Clin Oncol*, 2003. **21**(8): p. 1431-9.
31. Noble, S.L., Sherer, E., Hannemann, R.E., Ramkrishna, D., Vik, T., and Rundell, A.E., *Using adaptive model predictive control to customize maintenance therapy chemotherapeutic dosing for childhood acute lymphoblastic leukemia*. *J Theor Biol*, 2010. **264**(3): p. 990-1002.
 32. Mackey, M.C., *Unified hypothesis for the origin of aplastic anemia and periodic hematopoiesis*. *Blood*, 1978. **51**(5): p. 941-56.
 33. Rocchetti, M., Del Bene, F., Germani, M., Fiorentini, F., Poggesi, I., Pesenti, E., Magni, P., and De Nicolao, G., *Testing additivity of anticancer agents in pre-clinical studies: a PK/PD modelling approach*. *Eur J Cancer*, 2009. **45**(18): p. 3336-46.
 34. Parra-Guillen, Z.P., Berraondo, P., Ribba, B., and Troconiz, I.F., *Modeling tumor response after combined administration of different immune-stimulatory agents*. *J Pharmacol Exp Ther*, 2013. **346**(3): p. 432-42.
 35. Pascal, J., Bearer, E.L., Wang, Z., Koay, E.J., Curley, S.A., and Cristini, V., *Mechanistic patient-specific predictive correlation of tumor drug response with microenvironment and perfusion measurements*. *Proceedings of the National Academy of Sciences*, 2013. **110**(35): p. 14266-14271.
 36. Ashley, C.E., Carnes, E.C., Phillips, G.K., Padilla, D., Durfee, P.N., Brown, P.A., Hanna, T.N., Liu, J., Phillips, B., Carter, M.B., Carroll, N.J., Jiang, X., Dunphy, D.R., Willman, C.L., Petsev, D.N., Evans, D.G., Parikh, A.N., Chackerian, B., Wharton, W., Peabody, D.S., and Brinker, C.J., *The targeted delivery of multicomponent cargos to cancer cells by nanoporous particle-supported lipid bilayers*. *Nat Mater*, 2011. **10**(5): p. 389-397.
 37. Pascal, J., Ashley, C.E., Wang, Z., Brocato, T.A., Butner, J.D., Carnes, E.C., Koay, E.J., Brinker, C.J., and Cristini, V., *Mechanistic modeling identifies drug-uptake history as predictor of tumor drug resistance and nano-carrier-mediated response*. *ACS Nano*, 2013. **7**(12): p. 11174-82.
 38. Sanga, S., Frieboes, H.B., Zheng, X., Gatenby, R., Bearer, E.L., and Cristini, V., *Predictive oncology: a review of multidisciplinary, multiscale in silico modeling linking phenotype, morphology and growth*. *Neuroimage*, 2007. **37 Suppl 1**: p. S120-34.
 39. Wang, Z. and Deisboeck, T.S., *Computational modeling of brain tumors: discrete, continuum or hybrid?* *Scientific Modeling and Simulation SMNS*, 2008. **15**(1): p. 381.
 40. Frieboes, H.B., Jin, F., Chuang, Y.L., Wise, S.M., Lowengrub, J.S., and Cristini, V., *Three-dimensional multispecies nonlinear tumor growth-II: Tumor invasion and angiogenesis*. *J Theor Biol*, 2010. **264**(4): p. 1254-78.
 41. Macklin, P., McDougall, S., Anderson, A.R., Chaplain, M.A., Cristini, V., and Lowengrub, J., *Multiscale modelling and nonlinear simulation of vascular tumour growth*. *J Math Biol*, 2009. **58**(4-5): p. 765-98.

42. Wu, M., Frieboes, H.B., McDougall, S.R., Chaplain, M.A., Cristini, V., and Lowengrub, J., *The effect of interstitial pressure on tumor growth: coupling with the blood and lymphatic vascular systems*. J Theor Biol, 2013. **320**: p. 131-51.
43. Pelicano, H., Martin, D.S., Xu, R.H., and Huang, P., *Glycolysis inhibition for anticancer treatment*. Oncogene, 2006. **25**(34): p. 4633-46.
44. Estrella, V., Chen, T., Lloyd, M., Wojtkowiak, J., Cornnell, H.H., Ibrahim-Hashim, A., Bailey, K., Balagurunathan, Y., Rothberg, J.M., Sloane, B.F., Johnson, J., Gatenby, R.A., and Gillies, R.J., *Acidity generated by the tumor microenvironment drives local invasion*. Cancer Res, 2013. **73**(5): p. 1524-35.
45. Smallbone, K., Gatenby, R.A., Gillies, R.J., Maini, P.K., and Gavaghan, D.J., *Metabolic changes during carcinogenesis: potential impact on invasiveness*. J Theor Biol, 2007. **244**(4): p. 703-13.
46. Gatenby, R.A., Smallbone, K., Maini, P.K., Rose, F., Averill, J., Nagle, R.B., Worrall, L., and Gillies, R.J., *Cellular adaptations to hypoxia and acidosis during somatic evolution of breast cancer*. British Journal of Cancer, 2007. **97**(5): p. 646-653.
47. Anderson, A.R., *A hybrid mathematical model of solid tumour invasion: the importance of cell adhesion*. Math Med Biol, 2005. **22**(2): p. 163-86.
48. Anderson, A.R., Weaver, A.M., Cummings, P.T., and Quaranta, V., *Tumor morphology and phenotypic evolution driven by selective pressure from the microenvironment*. Cell, 2006. **127**(5): p. 905-15.
49. Sun, X., Zhang, L., Tan, H., Bao, J., Strouthos, C., and Zhou, X., *Multi-scale agent-based brain cancer modeling and prediction of TKI treatment response: Incorporating EGFR signaling pathway and angiogenesis*. BMC Bioinformatics, 2012. **13**: p. 218-218.
50. Anderson, A.R. and Chaplain, M.A., *Continuous and discrete mathematical models of tumor-induced angiogenesis*. Bull Math Biol, 1998. **60**(5): p. 857-99.
51. Olsen, M.M. and Siegelmann, H.T., *Multiscale Agent-based Model of Tumor Angiogenesis*. Procedia Computer Science, 2013. **18**: p. 1016-1025.
52. Wang, Z., Birch, C.M., and Deisboeck, T.S., *Cross-scale sensitivity analysis of a non-small cell lung cancer model: linking molecular signaling properties to cellular behavior*. Biosystems, 2008. **92**(3): p. 249-58.
53. Wang, Z., Bordas, V., and Deisboeck, T.S., *Identification of Critical Molecular Components in a Multiscale Cancer Model Based on the Integration of Monte Carlo, Resampling, and ANOVA*. Front Physiol, 2011. **2**: p. 35.
54. Wang, Z., Bordas, V., Sagotsky, J., and Deisboeck, T.S., *Identifying therapeutic targets in a combined EGFR-TGFbetaR signalling cascade using a multiscale agent-based cancer model*. Math Med Biol, 2012. **29**(1): p. 95-108.
55. Wang, Z., Deisboeck, T.S., and Cristini, V., *Development of a sampling-based global sensitivity analysis workflow for multiscale computational cancer models*. IET Syst Biol, 2014. **8**(5): p. 191-7.
56. Biava, P.M., Basevi, M., Biggiero, L., Borgonovo, A., Borgonovo, E., and Burigana, F., *Cancer cell reprogramming: stem cell differentiation stage factors and an agent based model to optimize cancer treatment*. Curr Pharm Biotechnol, 2011. **12**(2): p. 231-42.

57. Enderling, H., Anderson, A.R., Chaplain, M.A., Beheshti, A., Hlatky, L., and Hahnfeldt, P., *Paradoxical dependencies of tumor dormancy and progression on basic cell kinetics*. Cancer Res, 2009. **69**(22): p. 8814-21.
58. Enderling, H., Hlatky, L., and Hahnfeldt, P., *Migration rules: tumours are conglomerates of self-metastases*. British Journal of Cancer, 2009. **100**(12): p. 1917-1925.
59. Enderling, H., Hlatky, L., and Hahnfeldt, P., *The promoting role of a tumour-secreted chemorepellent in self-metastatic tumour progression*. Math Med Biol, 2012. **29**(1): p. 21-9.
60. Mukhopadhyay, R., Costes, S.V., Bazarov, A.V., Hines, W.C., Barcellos-Hoff, M.H., and Yaswen, P., *Promotion of variant human mammary epithelial cell outgrowth by ionizing radiation: an agent-based model supported by in vitro studies*. Breast Cancer Res, 2010. **12**(1): p. R11.
61. Enderling, H., Chaplain, M.A., Anderson, A.R., and Vaidya, J.S., *A mathematical model of breast cancer development, local treatment and recurrence*. J Theor Biol, 2007. **246**(2): p. 245-59.
62. Powathil, G.G., Gordon, K.E., Hill, L.A., and Chaplain, M.A., *Modelling the effects of cell-cycle heterogeneity on the response of a solid tumour to chemotherapy: biological insights from a hybrid multiscale cellular automaton model*. J Theor Biol, 2012. **308**: p. 1-19.
63. Pennisi, M., Pappalardo, F., Palladini, A., Nicoletti, G., Nanni, P., Lollini, P.-L., and Motta, S., *Modeling the competition between lung metastases and the immune system using agents*. BMC Bioinformatics, 2010. **11**(Suppl 7): p. S13-S13.
64. Lollini, P.-L., Motta, S., and Pappalardo, F., *Discovery of cancer vaccination protocols with a genetic algorithm driving an agent based simulator*. BMC Bioinformatics, 2006. **7**(1): p. 352.

CHAPTER 2

Overview of Models Presented

In this work, we will explore the development and implementation of three different but related hybrid models of the human mammary gland system. Through creation of a hybrid continuum/agent-based model, a model system was generated that describes the human mammary gland, both at an individual cell scale, and also at molecular and tissue scales through a continuum description of molecular movement, consumption, and production within the tissue. This model system incorporates appropriate, biologically supported cell phenotypic hierarchies and types, and signaling pathways, in order to provide cell-by-cell insights into the subtle cell population dynamics involved in organ development and maintenance. Following validation, the model was further adapted to describe both the developing gland (which occurs during female puberty), and also a post-menopausal representation of the mature gland, which experiences an induced transition to a precancerous DCIS phenotype, disrupting gland homeostasis and resulting in simulated initiation and development of early stage breast cancer. In the following chapters, we will explore the development of these models, some results and insights from model simulations, and plans for the next future step: further model development. These models were inspired, in part, by previous modeling work in the mammary gland and DCIS; these are reviewed in detail in the appropriate sections in the following chapters.

I. Modeling the Mammary Terminal End Bud

Our modeling efforts on the pubertal terminal end bud (TEB) to date have been split into two distinct but related models: a two-dimensional, lattice-based model, and a three-dimensional lattice-free model. Each method presents its own set of advantages and challenges, which are briefly discussed here. Biologically, the TEB is a three-dimensional structure, which possesses a rough axial symmetry. To this end, we initially assumed an axial symmetry of the structure, and thus implemented a “slice” of the TEB in two-dimensions as a reasonable approximation of the biological structure. A two-dimensional approximation, although a simplification of the structure as it occurs in nature, offers some distinct advantages over a model that provides a complete three-dimensional representation.

Each time an additional level of complexity is added to a model, the modeler gains a more complete description of the biological system, and possibly a model that may more completely and accurately replicate or even predict the biological system behavior. This new information is not free, however, and needs additional computational power, commonly resulting in increased simulation run times or even requiring the acquisition or implementation of new computational resources. Additional complexity is introduced into a model through the inclusion of new variables, equations, or other factors- all of which may introduce additional sources of error (for more information, see Chapter 1, section I). Placing the ABM portion of the model into a lattice-based structure further reduces computational costs, as the complexities of solving the physics of cell-cell interaction are reduced to a greatly simplified description of cell movement. In these early stages of model development, computational efficiency is especially important, as faster model run times

allow for extensive testing in a shorter time, so the model may be tested, calibrated, and validated in a reasonable time frame. By starting with a simple model, *in silico* researchers are able to focus on only the biologically factors thought to play the greatest role in the system, and to confirm their importance by a model that only examines their effects. In this way, the model is limited to a few (but important) parameters, which may later be expanded upon, if the model is validated successfully in the simplified state.

Each new variable added into a model runs the risk of being a confounding variable (introducing accidental bias to the system) or introducing unanticipated variable interaction effects, and may lead to incorrect assessment of the importance each parameter plays in the overall system. The number of parameters included in a model, and the corresponding number of equations, must also be constrained by available information. One cannot include too many unknown parameters, or parameters that may only be quantified through model fitting. This situation can result in overfitting, where too many unknowns have been fit to a particular set of data, often imparting unwarranted weight to some variables and hindering, if not completely eliminating, any predictive power of the model. For these reasons (among others), models are often first validated at a simpler implementation before being expanded into more complex and detailed versions.

i. Two-dimensional TEB Model

By first studying the TEB in a two-dimensional, lattice-based hybrid model, we were able to address and account for many of these factors while simultaneously developing a platform that would later be expanded out into a more complex, three-dimensional description. Many of the biological descriptions, computational methods,

model validation rubrics, and parameter calibrations used in and tested with the two-dimensional model were directly or easily translatable to the three-dimensional model as well. More importantly, however, the two-dimensional model was able to successfully replicate literature-supported parameters, including cell-cell phenotypic hierarchy behaviors, replication cycle statistics, mammary gland development rates, and the phenotypic distribution as observed in the biological mature gland. By finding a set of model parameter ranges that resulted in model outputs with good correlation to these values as reported in the literature, we were able to successfully calibrate the model parameters, simultaneously providing insights into quantified ranges of the behaviors in nature and establishing parameter baseline values for future modeling efforts.

Chapters 3 and 4 detail the development of this two-dimensional model of the pubertal terminal end bud (TEB). **Chapter 3** presents initial model development, as presented at the 36th Annual International Conference of the IEEE Engineering in Medicine and Biology Society (EMBC, 2015), and reproduced with permission from [1]. This initial effort was improved upon, through inclusion of more literature supported data, including biologically-measured TEB geometry data, calibrated cell cycle statistics (including refined symmetric proliferation probability data, and model calibrated and literature supported maximum number of mitosis cycles), as well as endocrine and paracrine signaling methods and associated discrete-continuum scale feedback. When properly calibrated, this improved version of the model showed good agreement with literature supported values, and provided interesting insights about the time-dependent dynamics of phenotypic distribution within the TEB. Of note, the model results showed the importance of phenotype hierarchies and endocrine and paracrine signaling in the resulting phenotype

distribution within the mature mammary gland, an important factor in gland homeostasis maintenance subsequent to development. It was also demonstrated that, under biologically relevant conditions, the gland has the potential to develop at even faster rates than those observed *in vivo*, indicating that endocrine and paracrine signaling mechanisms play important roles in not only initiation and perpetuation of gland development, but also important regulatory roles in controlling gland development rates. The details of these important steps are elaborated in **Chapter 4**, alongside detailed model results, our observations, and the important information we gleaned from this effort (i.e. that which was deemed pertinent to future modeling efforts of the TEB), as published in *The Journal of Theoretical Biology*, reproduced with permission from [2].

ii. Three-dimensional TEB Model

Building on the successful implementation of the two-dimensional TEB model, we moved forward into a more biologically complete three-dimensional model of the TEB; the results of which to-date are presented in **Chapter 5** (as presented at EMBC, 2016), reproduced with permission from [3]. Notable improvements over the previous model include removal of the lattice-based agent movement restriction (allowing for explicit modeling of cell-cell physical interaction, repulsion and inelastic cell deformation (modeled implicitly through a coefficient of restitution between cells), cytoplasmic expansion induced growth during interphase, and cell-cell and cell-basement membrane (BM) adhesion), and implementation of a more complex (and more biologically correct) epithelial to stromal paracrine signaling pathway (more detail on this topic is provided in Chapter 6, Introduction, and Chapter 7, Introduction). Implementing a three-dimensional

representation of the TEB allowed for the removal of the axial symmetry approximation which was inherently necessary in the two-dimensional approximation, resulting in more accurate correlation between model output and biologically reported values.

A three-dimensional representation also improves the biological representation of calculated molecular descriptions within the gland, as the two-dimensional representation fails to impart correct weights to ABM imparted molecular modifications onto the continuum scale. For example, in a three dimensional representation of a mammary duct (a roughly cylindrical structure, composed of two concentric cell layers), the outermost cell “layer” will contain more cells than a “layer” closer to the duct axis (assuming all cells are of roughly equal cytoplasmic volume and radius), and the larger number of cells in the outermost layer would be expected to have a greater effect on molecular profiles, e.g. more cells may consume more oxygen. However, in two dimensions, our symmetry assumption results in the same number of cells at both radii (in this case, perhaps in a “slice” of a duct). This restriction artificially imparts an equal contribution to oxygen concentration reduction for cells in both regions – contrary to the actual biological structure, where the outer layer in this example would be expected to consume more total oxygen. A three-dimensional representation also correctly describes the surface-to-volume ratio of the structure, a parameter that has an effect on molecular parameters, including molecular influx, efflux, and distribution through the structure. Lastly, the removal of the lattice-based restriction on agents allows for inclusion of additional important parameters, including the effects of cytoplasmic volume changes through the cell cycle, and the effect of cell-cell interactions.

II. Modeling Ductal Carcinoma in Situ

Chapter 6 details the development of a three-dimensional, lattice free model of the mature mammary gland for the study of initiation of post-menopausal DCIS, and presents some initial results from the model validation process, reproduced with permission from [4]. This model was accomplished using a simulated length of mature, post-menopausal mammary duct, which we assumed to be cylindrical for ease of implementation and to remove any unintended effects of a variable duct cross section on reported model outputs. In the model, cancer is initiated at time $t=0$ through spontaneous epithelial to mesenchymal (EMT) transition to a DCIS phenotype in one or more luminal cells, resulting in a cancer stem cell (CSC) phenotype and subsequent DCIS invasion into the luminal cavity. This model is built upon the previous model of the developing mammary gland, and includes many of the same aspects, including the literature-based phenotype hierarchy, and signaling pathways – although both are perturbed from the healthy state, in order to accurately represent a cancer phenotype.

Modeling a cancer state required the model to be altered from the conditions included in the previously mentioned healthy development models. Molecular pathways were “broken” from the healthy state, allowing cells to experience more intense molecular signaling or to undergo a mutation which made them more sensitive to the signaling, resulting in unregulated proliferation. Cancer cells also consume oxygen at higher rates, based on literature reported values [5]. Phenotypically, non-stem progenitive cells may now undergo many more mitosis cycles than in the healthy gland, based on values reported in [6, 7].

Subsequent to the model validation presented in Chapter 6, we sought to improve the model to better represent the cancer environment. We imposed a cell density proliferation limitation for progenitor cells, where proliferative cells become proliferation-restricted should their local cell density rise above a defined threshold, resulting in a transition into a reversible quiescent state (the quiescent state is reversed should local cell density drop below this threshold at a later time). Due to the higher oxygen consumption rates within the DCIS population (and a lack of vasculature in this region), hypoxic conditions may occur within the DCIS tumor. Under these conditions, cells will become hypoxic and then necrotic after a period of time, unless they are displaced into a region of higher oxygen concentration, or the local oxygen concentration rises back above the threshold. Transition to necrosis is taken to be irreversible, and cells that become necrotic will die and undergo a cell lysis process, where the cell swells until membrane rupture, leaking its cytoplasmic contents out into the duct cavity space. These regions are then calcified, resulting in hydroxyapatite accumulation in regions of extended hypoxia. The details of this process, quantified parameter values, and simulation results are detailed and discussed in **Chapter 7**.

III. Future Directions Overview

Finally, we will discuss the presented results and explore the next steps, where we present our plans for future model development and studies in **Chapter 8**. Both three-dimensional models will be further improved in order to gain a more complete understanding into quantified behaviors of the underlying biology. We will briefly examine the reasons for, and possible implementation methods of, these ideas. This discussion will

serve as a guide to direct interested readers towards upcoming publications of the results of these efforts, and hopefully also inspire others to implement new and interesting aspects into their models as well.

IV. Works Cited, Chapter 2

1. Butner, J.D., Cristini, V., and Zhihui, W., *A modeling approach to study the normal mammary gland growth process*. Conf Proc IEEE Eng Med Biol Soc, 2015. **2015**: p. 1444-7.
2. Butner, J.D., Chuang, Y.L., Simbawa, E., Al-Fhaid, A.S., Mahmoud, S.R., Cristini, V., and Wang, Z., *A hybrid agent-based model of the developing mammary terminal end bud*. J Theor Biol, 2016. **407**: p. 259-70.
3. Butner, J.D., Cristini, V., and Zhihui, W., *Development of a three dimensional, lattice-free multiscale model of the mammary terminal end bud*. Conf Proc IEEE Eng Med Biol Soc, 2016. **2016**: p. 6134-6137.
4. Butner, J.D., Cristini, V., and Wang, Z., *Development of a Three Dimensional, Multiscale Agent-Based Model of Ductal Carcinoma in Situ*. Conf Proc IEEE Eng Med Biol Soc, 2017. **In Press**.
5. Wagner, B.A., Venkataraman, S., and Buettner, G.R., *The rate of oxygen utilization by cells*. Free Radic Biol Med, 2011. **51**(3): p. 700-12.
6. Wang, J., Hannon, G.J., and Beach, D.H., *Risky immortalization by telomerase*. Nature, 2000. **405**(6788): p. 755-6.
7. Wang, J., Xie, L.Y., Allan, S., Beach, D., and Hannon, G.J., *Myc activates telomerase*. Genes & Development, 1998. **12**(12): p. 1769-1774.

CHAPTER 3

Development of an Agent-Based Model for Simulating Normal Mammary Gland Growth

Joseph D. Butner, Vittorio Cristini, and Zhihui Wang, *Member, IEEE*

This work has been supported in part by the National Science Foundation (NSF) Grant DMS-1263742 (V.C., Z.W.), the National Institutes of Health (NIH) Grant 1U54CA143837, 1U54CA151668, and 2P50GM085273 (V.C.), King Abdulaziz University grant 54-130-35-HiCi (V.C.), and the University of Texas System STARS Award (V.C.).

J.D.B. is with the Department of Chemical Engineering and Center for Biomedical Engineering, University of New Mexico, Albuquerque, NM 87131, USA.

V. C. and Z.W. are with the Department of NanoMedicine and Biomedical Engineering, and Brown Foundation Institute of Molecular Medicine, University of Texas Medical School at Houston, Houston, TX 77054, USA, and also with Department of Imaging Physics, University of Texas MD Anderson Cancer Center, Houston, TX 77230, USA (corresponding author, phone: 713-486-5427; fax: 713-500-3672; e-mail: wzhlfp@gmail.com).

V.C. is also with Department of Mathematics, Faculty of Science, King Abdulaziz University, Jeddah 21589, Saudi Arabia.

I. Abstract

Terminal end buds (TEBs) are bulb-like structures at the growing tips of elongating mammary ducts, and the growth of a TEB is a complex, organized biological process. In this paper, we present a hybrid continuum-discrete agent-based model to provide quantitative insight into the properties of cell symmetric and asymmetric division on the spatial and developing cell rearrangement within the TEB during ductal elongation. An interplay of endocrine-paracrine signaling and cell lineage has been implemented in the model. Our results show that higher symmetric division rates resulted in more progenitor cells remaining in the TEB, while lower rates resulted in more differentiated cells in the TEB. Moreover, pure proliferation alone was enough to result in ductal elongation in the absence of any cellular migration, a result consistent with current experimental data. This model can also serve as a platform to study how mutation-induced phenotypic changes contribute to developmental defects in mammary gland development.

II. Introduction

Pubertal development of the mammary gland is characterized by epithelial invasion of the mammary ductal tree away from the nipple and into the stromal fat pad. The mammary gland is primarily composed of basal and luminal cells, with myoepithelial cells and a few intermittent stem cells in the basal region surrounding an inner layer of luminal cells [1]. Individual branches are advanced by a terminal end bud (TEB) structure,

a bulbous region characterized by high cellular proliferation rates and thought to be capped with oligopotent stem cells [2].

The mammary gland development process is initiated and regulated in part by endocrine and paracrine signaling [3]. A well-studied endocrine-paracrine signaling cascade is shown in **Figure 3.1**. Briefly, estrogen induces upregulation of amphiregulin (AREG) production in luminal estrogen receptor alpha positive (ER+) cells [4], which induces progesterone-mediated proliferation [5] in estrogen receptor negative (ER-), epidermal growth factor receptor (EGFR) positive basal and luminal cells. This signaling cascade is directly involved in ductal elongation due to cellular proliferation, both in growth of primary ducts and ductal branches [6]. TEB growth and cellular proliferation is induced by estrogen signaling, with AREG playing a mediation role, and both estrogen and AREG are necessary for mammary gland development [3]. It has also been reported that a single stem cell can give rise to both luminal and myoepithelial lineages, resulting in a

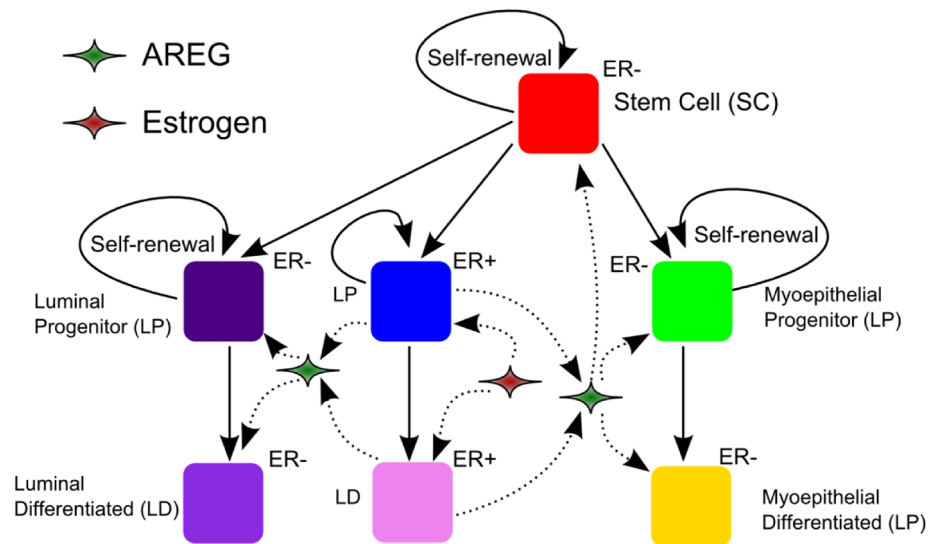


Figure 3.1: Cellular lineages and estrogen and AREG signaling pathways. Estrogen upregulates AREG production in ER+ cells, which induces proliferation in ER-/EGFR+ myoepithelial and luminal cells.

complete mammary gland structure [7]. Mammary stem cells are capable of self-renewal for many cell cycles, as well as asymmetric division into epithelial progenitor cells, both of which are shown to be rapidly proliferative. Progenitor cells are more numerous in the mammary gland than stem cells, and both are found in regions of the mammary gland distinct from the TEB [7], with stem cell niches found in the duct regions and proliferative cells in mammary gland lobules.

Mathematical modeling has been used to quantitatively represent and simulate normal mammary gland development [8, 9] and ductal carcinoma *in situ* (DCIS) [10-12]. However, models developed to date do not account for the dominant TEB contribution in the mammary developmental process during puberty. Here, we develop a hybrid continuum-discrete ABM to provide quantitative insight into how the interplay of endocrine-paracrine signaling and cell lineage within the TEB affects mammary gland growth during pubertal development. While a complete description of the known pubertal TEB signaling cascade is beyond the scope of this work, we select an important piece of the endocrine-paracrine signaling as shown in **Figure 3.1**, where ER⁺ luminal cells are stimulated by estrogen and produce AREG, resulting in downstream stimulation of ER⁻ cells in the basal and luminal layers of the TEB. This model can serve as a platform to study the mechanisms through which mutation-induced phenotypic changes contribute to developmental defects in the TEB and mammary gland development.

in **Figure 3.2**. The internal ductal cavity represents the apoptotic zone (i.e., region 0). Within the proliferative zones, agents only divide symmetrically into progenitive daughter cells, but may differentiate after several divisions. Within the differentiation zone, agents may divide symmetrically or asymmetrically, giving rise to differentiated daughter cells. Agents may move out of the computational domain from regions 4 & 8, at which point they are considered part of the fully mature duct and removed from the simulation.

ii. *Continuum Component*

Continuum profiles of molecular gradients are described using a general reaction-diffusion equation:

$$\frac{\partial u}{\partial t} = D\nabla^2 u + R(u), \quad (1)$$

where u is the molecular concentration (of estrogen, AREG, and oxygen, respectively), D the corresponding diffusion constant, and $R(u)$ a reaction term (here specifically referring to molecular degradation), taken to be a constant in this case. This equation is solved numerically using finite element methods (FEM) for each time step. Time-dependent solutions are then obtained on a tetragonal mesh in C++ using Sundance [13], a FEM solver package included in the Trilinos Project, a numerical toolset developed by Sandia National Laboratory. Exact FEM solution values are passed to the agents, who use them to make behavioral decisions (see next Section). Agent modifications to the FEM solutions are imposed by imposition of Dirac delta functions onto the nearest node to the appropriate agent as determined through Voronoi tessellation. Molecular profiles for molecules that enter the mammary ductwork from surrounding tissues (O_2 and estrogen) are imposed as

normalized Dirichlet boundary conditions, while molecules that are produced inside the mammary ductwork are allowed to diffuse freely without boundary conditions.

iii. Discrete Component

Each cell in the TEB and mature mammary duct (**Figure 3.2**) is represented as a discrete entity (agent), complete with its own unique location, phenotype, and cell lineage (also see **Figure 3.1**). On a hexagonally close packed grid, agents can move, undergo symmetric or asymmetric mitosis, differentiate, and enter necrosis and subsequent lysis as a result from hypoxic conditions. Cells make their phenotypic decision changes according to a specific algorithm. Briefly, for an agent at each time step, if the oxygen threshold is below the necrosis threshold, the agent attempts to undergo chemotaxis towards higher oxygen concentration; if there is not a space to move, it undergoes necrosis and lysis. ER+ agents also query the estrogen concentration, and ER-/EGFR+ agents probe the AREG concentration at their location. Throughout each cell cycle, we check every 30 minutes to determine which agents may proliferate (i.e. it has been at least one full cell cycle since their last proliferation), and agents that are eligible to proliferate may do so. Agents also modify the continuum solutions, either by consuming molecules and lowering the concentration at their location or by producing molecules and increasing their concentration at their location. Agents which have the appropriate proliferation signaling molecule above the minimum threshold (i.e., estrogen for ER+ and AREG for ER- cells) may proliferate if there is room, or they may differentiate as shown in **Figure 1**. A maximum number of proliferation cycles is imposed on all cell types except for stem cells, which may proliferate indefinitely, again provided they have room to do so. When cells

have undergone the maximum number of proliferation cycles they automatically differentiate.

iv. *Model Parameters*

Most parameters, including initial concentrations and diffusion rates of signaling molecules, are obtained from the literature or estimated when unavailable. For example, while the diffusion constant for oxygen in tissue is well established in the literature, diffusion constants for estrogen and AREG are not as well characterized, and thus are estimated based on relative molecular weights. The molecular weight of estrogen is approximately 17 times larger than O_2 , while the four isoforms of AREG vary from over 560 to almost 2,700 times larger molecular weight [16], so it is established that diffusivity constants are $D_{\text{oxygen}} > D_{\text{estrogen}} > D_{\text{AREG}}$.

TABLE 3.1 KEY MODEL PARAMETERS.

Parameter	Value	Reference
Necrosis threshold	0.2	[11]
D_{oxygen}	$2.5 \times 10^{-6} \text{ cm}^2 \text{ s}^{-1}$	[14]
D_{estrogen}	$< D_{\text{oxygen}}$	
D_{AREG}	$< D_{\text{estrogen}}$	
Cell cycle time	16 hours	[11]
Cell death (+ lysis) time	< 16 hours	[15]
Proliferation rate	≤ 1 per 16 hours	
Maximum cycles before differentiation	2-3	
Asymmetric division probability	Varies	
Stem cell differentiation probability	0.10	
Probability of spontaneous differentiation	0.001	

We take cell cycle time to be 16 hours based on observed cell cycle time in the TEB. Investigations on the mechanisms of cellular death resultant from hypoxia have indicated that it is a combination of both necrosis and apoptosis, which is dependent on cell type [15]. We lump both mechanisms together, and consider apoptosis times that have been established on the order of hours, with onset of pyknosis within 12 hours and commencement of cellular lysis within 24 hours. Normalized threshold for cellular death due to hypoxia is taken to be 0.2 as in [11]. A list of key model parameters can be found in **Table 3.1**.

IV. Results and Discussion

We examined the impact of (1) symmetric (and asymmetric) division rates and (2) maximum cell cycles before differentiation (see **Table 3.1**) on mammary gland growth rates. We varied symmetric (and asymmetric) division probability through a range of [0.2, 0.3, ..., 0.9]; note that the sum of both division probabilities should always be 1.0. Since progenitor cells (that are not stem) may only divide a limited number of times before they differentiate, we only focused on two cases: 2 and 3 maximum cell cycles before differentiation.

i. Symmetric vs. Asymmetric Division

Figure 3.3 shows the simulation results. Higher symmetric division probability results in more progenitor cells remaining in the TEB, while lower rates result in more differentiated cells in the TEB. In **Figure 3.3B** and **3.3C**, agents divide symmetrically in

the proliferative zone (regions 1 and 5), asymmetrically or symmetrically in the differentiation zone (regions 2 and 6), have a higher chance of asymmetric division to give rise to differentiated daughter cells in the immature duct (regions 3 and 7), and any progenitors remaining in the mature duct may only give rise to differentiated daughters. When symmetric division rates are high, fewer differentiated cells are seen in the computational domain, even in the mature duct region. Conversely, when symmetric rates are low, the TEB differentiation region becomes predominantly filled with differentiated cells, reducing growth rates. This effect is mitigated by the population of mostly progenitor cells in the proliferative zone, however, as this region contains the majority of proliferating

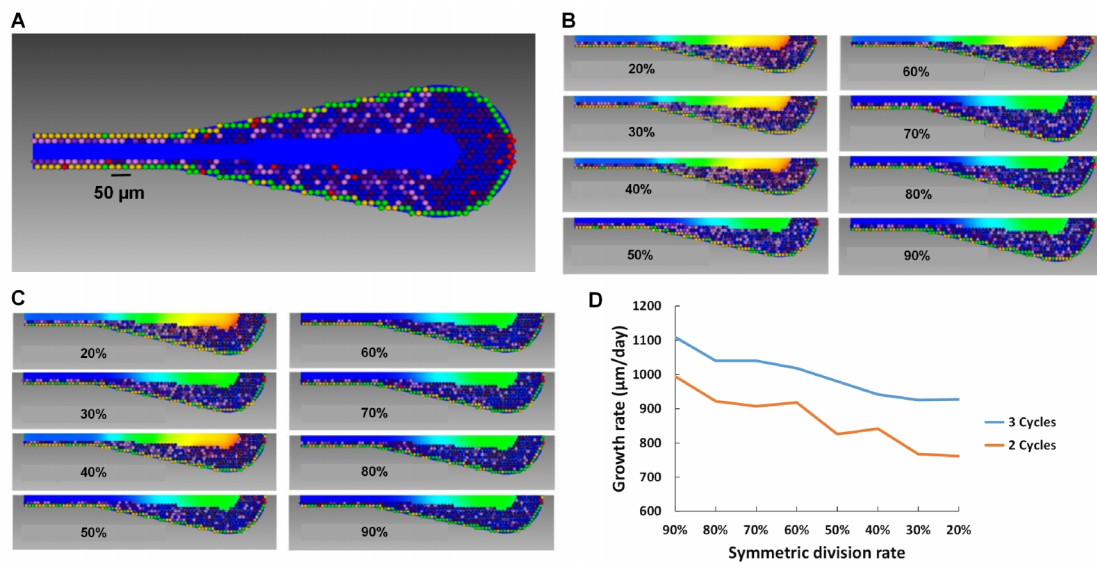


Figure 3.3: Parameter analysis. (A) Initial seeding of agents within the TEB domain. (B) Simulation results showing 2 cycles before differentiation at various symmetric division probabilities. Low symmetric division probabilities are seen to result in large numbers of differentiated cell in both the proliferation and differentiation zones. Even at 90% symmetrical division, large numbers of differentiated cells are seen in the proliferation region, indicating a need for more cell cycles before differentiation. (C) Three cell cycles before differentiation. Differentiated cells are again observed in all regions, but at higher symmetric division probability progenitor cells still occupy most of the region, resulting in higher growth rates. (D) Growth rates observed from the cases shown in (B) and (C). Higher symmetric division rates and more cell cycles before differentiation both increase ductal elongation growth rate. See **Figure 3.1** for color scheme.

cells. Additionally, cells in the differentiating region are rapidly moving towards the mature duct and away from the proliferative region. Whether a daughter is differentiated or a progenitor cell, it may or may not remain in this region for a full cell cycle. In the case of exiting the proliferative or differentiation region before the next cell cycle, daughter type has no influence on ductal elongation rate. The differentiation zone experiences an influx of agents from the proliferative zone, which may have proliferated before entering the differentiation zone. These agents may become differentiated due to reaching the maximum cycles before differentiation limit, contributing to the population of differentiated cells in the TEB.

ii. *Differentiation*

A more complete description of the relationship between growth rates and differentiation rates is shown in **Figure 3.3D**. Differentiation and asymmetric division are interrelated, and that higher rates of asymmetric division or lower number of cell cycles before differentiation have similar consequences: higher percentages of differentiated cells in the TEB. Cell cycles before differentiation has a large impact on growth rates. For example, with 80% symmetric differentiation, 1 cell cycle before differentiation results in large numbers of differentiated cells in the proliferation region of the TEB and arrested growth rates, while initial testing indicates 3 cell cycles is optimal for biologically accurate simulation results.

From our parameter analysis, we observe that pure proliferation was enough to result in ductal elongation in the absence of any cellular migration. In the future, we will break the signaling and behavioral rules governing normal ductal morphogenesis and

maintenance either individually or in defined combinations to predict what happens to the relative proportion of cell types in the gland in abnormal growth and development situations.

V. Acknowledgements

We thank M Lewis and J Rosen (Baylor College of Medicine), J Lowengrub (University of California, Irvine), and Y-L Chuang (California State University, Northridge). We also acknowledge the University of New Mexico Cancer Center Victor and Ruby Hansen Surface Professorship in Molecular Modeling of Cancer (V.C.), and the Methodist Hospital Research Institute (V.C.).

© 2015 IEEE. Reprinted and adapted, with permission, from Butner, J.D., V. Cristini, and W. Zhihui, *A modeling approach to study the normal mammary gland growth process*. Conf Proc IEEE Eng Med Biol Soc, 2015. **2015**: p. 1444-7.

VI. Works Cited, Chapter 3

1. Macias, H. and Hinck, L., *Mammary Gland Development*. Wiley interdisciplinary reviews. Developmental biology, 2012. **1**(4): p. 533-557.
2. Smalley, M. and Ashworth, A., *Stem cells and breast cancer: A field in transit*. Nat Rev Cancer, 2003. **3**(11): p. 832-844.
3. Ciarloni, L., Mallepell, S., and Brisken, C., *Amphiregulin is an essential mediator of estrogen receptor α function in mammary gland development*. Proceedings of the National Academy of Sciences of the United States of America, 2007. **104**(13): p. 5455-5460.
4. Sternlicht, M.D., Sunnarborg, S.W., Kouros-Mehr, H., Yu, Y., Lee, D.C., and Werb, Z., *Mammary ductal morphogenesis requires paracrine activation of stromal EGFR via ADAM17-dependent shedding of epithelial amphiregulin*. Development, 2005. **132**(17): p. 3923-33.
5. Aupperlee, M.D., Leipprandt, J.R., Bennett, J.M., Schwartz, R.C., and Haslam, S.Z., *Amphiregulin mediates progesterone-induced mammary ductal development during puberty*. Breast Cancer Research : BCR, 2013. **15**(3): p. R44-R44.
6. Wiesen, J.F., Young, P., Werb, Z., and Cunha, G.R., *Signaling through the stromal epidermal growth factor receptor is necessary for mammary ductal development*. Development, 1999. **126**(2): p. 335-44.
7. Stingl, J., Eirew, P., Ricketson, I., Shackleton, M., Vaillant, F., Choi, D., Li, H.I., and Eaves, C.J., *Purification and unique properties of mammary epithelial stem cells*. Nature, 2006. **439**(7079): p. 993-7.
8. Deisboeck, T.S., Wang, Z., Macklin, P., and Cristini, V., *Multiscale cancer modeling*. Annu Rev Biomed Eng, 2011. **13**: p. 127-55.
9. Tang, J., Enderling, H., Becker-Weimann, S., Pham, C., Polyzos, A., Chen, C.Y., and Costes, S.V., *Phenotypic transition maps of 3D breast acini obtained by imaging-guided agent-based modeling*. Integr Biol (Camb), 2011. **3**(4): p. 408-21.
10. Xu, Y. and Gilbert, R., *Some inverse problems raised from a mathematical model of ductal carcinoma in situ*. Mathematical and Computer Modelling, 2009. **49**(3-4): p. 814-828.
11. Macklin, P., Edgerton, M.E., Thompson, A.M., and Cristini, V., *Patient-calibrated agent-based modelling of ductal carcinoma in situ (DCIS): from microscopic measurements to macroscopic predictions of clinical progression*. J Theor Biol, 2012. **301**: p. 122-40.
12. Bankhead Iii, A., Magnuson, N.S., and Heckendorn, R.B., *Cellular automaton simulation examining progenitor hierarchy structure effects on mammary ductal carcinoma in situ*. Journal of Theoretical Biology, 2007. **246**(3): p. 491-498.
13. Long, K., Kirby, R., and Waanders, B.v.B., *Unified Embedded Parallel Finite Element Computations via Software-Based Fréchet Differentiation*. SIAM Journal on Scientific Computing, 2010. **32**(6): p. 3323-3351.
14. Sidell, B.D., *Intracellular oxygen diffusion: the roles of myoglobin and lipid at cold body temperature*. J Exp Biol, 1998. **201**(Pt 8): p. 1119-28.
15. Shimizu, S., Eguchi, Y., Kamiike, W., Itoh, Y., Hasegawa, J., Yamabe, K., Otsuki, Y., Matsuda, H., and Tsujimoto, Y., *Induction of apoptosis as well as necrosis by*

- hypoxia and predominant prevention of apoptosis by Bcl-2 and Bcl-XL. Cancer Res, 1996. 56(9): p. 2161-6.*
16. Brown, C.L., Meise, K.S., Plowman, G.D., Coffey, R.J., and Dempsey, P.J., *Cell surface ectodomain cleavage of human amphiregulin precursor is sensitive to a metalloprotease inhibitor. Release of a predominant N-glycosylated 43-kDa soluble form. J Biol Chem, 1998. 273(27): p. 17258-68.*

CHAPTER 4

A Hybrid Agent-based Model of the Developing Mammary Terminal End Bud

Joseph D. Butner,¹ Yao-Li Chuang,² Eman Simbawa,³ A.S. AL-Fhaid,³ S.R.

Mahmoud,³ Vittorio Cristini^{3,4,5,6}, and Zhihui Wang,^{4,5,6,*}

¹Department of Chemical and Biological Engineering and Center for Biomedical Engineering, University of New Mexico, Albuquerque, NM 87131;

²Department of Mathematics, California State University, Northridge, CA 91330;

³Department of Mathematics, Faculty of Science, King Abdulaziz University, Jeddah 21589, Saudi Arabia;

⁴Department of NanoMedicine and Biomedical Engineering, University of Texas Medical School at Houston, Houston, TX 77054;

⁵Brown Foundation Institute of Molecular Medicine, University of Texas Medical School at Houston, Houston, TX 77030;

⁶Department of Imaging Physics, University of Texas MD Anderson Cancer, Houston, TX 77230.

Short title: Hybrid modeling of the terminal end bud

Keywords: agent-based modeling, cell lineage, ductal elongation rate, hybrid modeling, mammary gland

*To whom correspondence should be addressed:

Zhihui Wang, Ph.D.

Department of Nanomedicine and Biomedical Engineering

The University of Texas Health Science Center at Houston McGovern Medical School

Houston, TX 77054, USA

Tel: 713-486-5425

Fax: 713-796-9697

Email: Zhihui.Wang@uth.tmc.edu

I. Abstract

Mammary gland ductal elongation is spearheaded by terminal end buds (TEBs), where populations of highly proliferative cells are maintained throughout post-pubertal organogenesis in virgin mice until the mammary fat pad is filled by a mature ductal tree. We have developed a hybrid multiscale agent-based model to study how cellular differentiation pathways, cellular proliferation capacity, and endocrine and paracrine signaling play a role during development of the mammary gland. A simplified cellular phenotypic hierarchy that includes stem, progenitor, and fully differentiated cells within the TEB was implemented. Model analysis finds that mammary gland development was highly sensitive to proliferation events within the TEB, with progenitors likely undergoing 2-3 proliferation cycles before transitioning to a non-proliferative phenotype, and this result is in agreement with our previous experimental work. Endocrine and paracrine signaling were found to provide reliable ductal elongation rate regulation, while variations in the probability a new daughter cell will be of a proliferative phenotype were seen to have minimal effects on ductal elongation rates. Moreover, the distribution of cellular phenotypes within the TEB was highly heterogeneous, demonstrating significant allowable plasticity in possible phenotypic distributions while maintaining biologically relevant growth behavior. Finally, simulation results indicate ductal elongation rates due to cellular proliferation within the TEB may have a greater sensitivity to upstream endocrine signaling than endothelial to stromal paracrine signaling within the TEB. This model provides a useful tool to gain quantitative insights into cellular population dynamics

and the effects of endocrine and paracrine signaling within the pubertal terminal end bud.

II. Introduction

Development of the mammary gland begins in the embryo but occurs primarily postnatally, subsequent to pubertal expansion of the fat pad. The rudimentary mammary ductal tree present at birth remains relatively dormant until puberty, when estrogen receptor positive (ER+) progenitor cells respond to estrogen signaling upregulation, in part, by proliferating and increasing local membrane-bound amphiregulin (AREG) cleavage into the extracellular space; AREG serves as a paracrine signal that promotes proliferation of estrogen receptor negative (ER-)/epidermal growth factor receptor positive (EGFR+) neighbors [2]. During pubertal gland development, each actively growing branch is terminated with and advanced by a terminal end bud (TEB), a bulbous structure composed primarily of progenitor cells. A TEB is capped with a layer rich in stem and regenerative cells, although it has been demonstrated that stem cells are not exclusively at the tip of the TEB [3].

Stem cells within the TEB are fundamental in mammary gland development through maintenance of the progenitor population. Work by Shackleton *et al.* demonstrated that a fully functional mammary gland could be developed from a single Lin⁻ CD29^{hi}CD24⁺ highly proliferative mammary stem cell (MaSc) [4], which was isolated from a stem cell population later determined to be ER- [5]. More recent studies into the stem cell population within the TEB have indicated that the stem cell niche in the TEB is composed of cells with different proliferation potentials, where stem cells can be either

multipotent (able to give rise to daughters of all phenotypes found within the TEB) or unipotent (able to give rise to only one daughter phenotype [3, 6]. MaScs are able to divide symmetrically, resulting in two phenotypically similar daughters, or to divide asymmetrically giving rise to one stem and one progenitor daughter, both of which can proliferate symmetrically or differentiate towards a more lineage-restricted phenotype [2, 7], together giving rise to luminal and myoepithelial lineages. This provides a mechanism for maintenance of stem and progenitor cell populations within a population of rapidly developing mature, differentiated cells during organogenesis. Furthermore, the dynamics of symmetric vs. asymmetric divisions within the progenitor population (where a mitosis event results in both mother and daughter having the same phenotype (either proliferative or differentiated; symmetric division) or the mother retains a proliferative phenotype while giving rise to a terminally differentiated daughter (asymmetric division)) plays a critical role in proper organogenesis, and is likely involved in mammary ductal elongation rates during this process. Efforts to quantify the rates of symmetric vs. asymmetric proliferation of stem cells indicate that they proliferate primarily asymmetrically. Investigations of stem cell symmetric division probability have shown 16% symmetric division in mammalian epithelial cells in vivo [8], 25% symmetric division in CD34⁺CD39^{lo} human severe combined immunodeficiency mouse-repopulating cells in vivo [9], and 13% symmetric division in primitive human hematopoietic stem cells in vitro [10], which are in agreement with mathematical modeling studies as well [8, 11]. Daughter phenotypes resulting from progenitor proliferation are more uncertain where symmetric proliferation has been reported from 10-70% [12-18]. Specific to the mammary gland, cell cycle time in MCF-

10A immortalized human mammary epithelial cells in the presence of epidermal growth factor has been reported as approximately 15.5 hours [19].

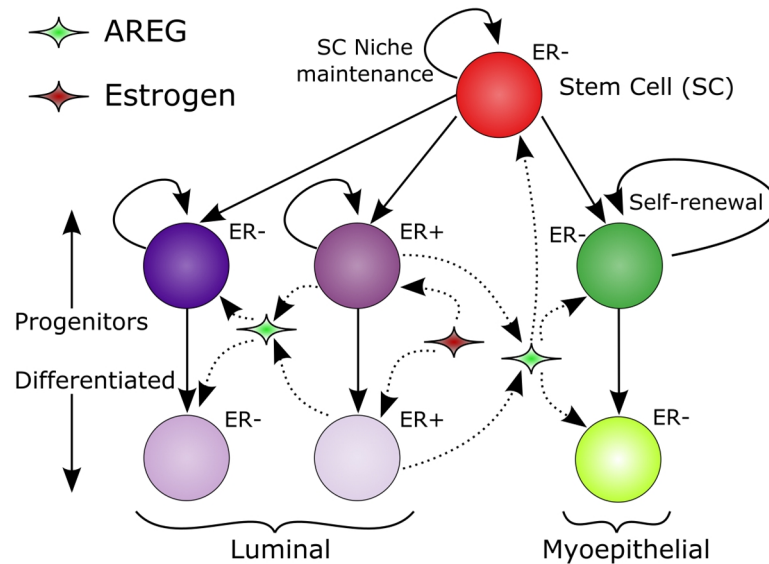


Figure 4.1: Cellular phenotypic hierarchy and signaling pathways. Stem cells may be unipotent or multipotent, and may self-renew or contribute to the myoepithelial or luminal progenitor populations when undergoing proliferation events. Progenitor populations are maintained primarily through symmetric progenitor proliferations. Progenitors may also give rise to differentiated daughters, and may differentiate upon reaching the proliferation cycle threshold. ER⁺ cells are stimulated to proliferate and produce AREG by upregulation of estrogen endocrine signaling, while AREG

It is well-established that AREG production increases in response to binding of ER alpha in the TEB epithelium [20], that ER⁻ mice fail to initiate pubertal mammary gland development in response to hormonal signaling at the onset of puberty [21], and that loss of AREG results in gross stunting in pubertal mammary gland development [20, 22]. AREG is involved in epithelial to stromal paracrine signaling through its interaction with EGFR [23], is connected to cellular differentiation and carcinogenesis in the mammary gland [7], and has been demonstrated to play a required role in development of TEBs, epithelial growth, and ductal elongation in the pubertal murine mammary gland [24].

We note that pubertal mammary gland development, and the resulting glandular architecture, is induced and regulated by a complex network of endocrine, paracrine, and autocrine signaling pathways [25]. The complexity of these signaling networks is beyond the scope of this work, and in fact remains partially uncharacterized, both in terms of all molecular players involved and in terms of quantification of molecular signaling thresholds necessary for upregulation of cellular proliferation. Accordingly, we have chosen to focus on only a small portion of the signaling network, namely endocrine system estrogen signaling and subsequent epithelial to stromal AREG signaling, as shown in **Figure 4.1**. For an excellent review of the more complete known signaling regulation pathways in development of the mammary gland, the reader is referred to [25].

While signaling events are responsible for induction and maintenance of gland development (as described above), gland growth is also a direct result of stem and progenitor population's proliferation within the TEBs. In addition, progenitor population size, distribution, and proliferation capacity play key roles in glandular development, phenotypic distribution within the mature duct, and ductal elongation rates. Hence, in this work, we examine how cellular phenotypic distribution and behavior within the TEB, as well as pubertal estrogen upregulation to stimulate ER⁺ cellular proliferation, in collaboration with downstream AREG paracrine signaling to ER⁻ cells, affect cellular proliferation, as well as how these signaling pathways play a role in overall cellular proliferation within the TEB during active pubertal mammary ductwork development.

Mathematical modeling and computer simulation have emerged as promising tools to help understand cellular phenotypic transitions and molecular signaling kinetics at different stages of tissue development. In study of the mammary gland, mathematical

modeling has made impressive strides, often with a focus on ductal carcinoma in situ (DCIS), the most common non-invasive cancer of the breast. In some mathematical studies of DCIS, the tumor is modeled as a continuum, allowing for calculation of estimated tumor size based on diffusion and mitotic/apoptotic indices [26] and examination of DCIS growth tendencies [27]. In other models, each cell is represented as a unique entity, an approach known as agent-based modeling (ABM) [28-30], which allows for information such as individual phenotype, cellular state, and cell-cell interactions to be included in the model. ABM has provided valuable insight into the apoptosis mechanisms that are known to play an instrumental role in mammary gland lumen formation [10, 31], and how the morphologies of DCIS can be influenced by cellular proliferation and apoptosis [32]. Other modeling approaches include aspects from both continuum and ABM methods to form hybrid models [33, 34]. Hybrid methods allow interaction and feedback between the different scales, with cells responding to the surrounding environment and modifying it. For example, the tumor environment is known to be hypoxic, low in pH, and have high glycolytic rates associated with high cellular proliferation (for more information the reader is referred to [35]), where limited concentration of available molecular resources can result in cell-cell competition and selection of more aggressive phenotypes. These phenomena are often incorporated into hybrid models, with feedback between the agents and the continuum solutions that account for both time-dependent movement of relevant molecules and their cellular uptake or production. In fact, hybrid models of DCIS have been used to provide insight into contact inhibition in the formation of the four morphologies of DCIS [36], and examine how acidosis and hypoxia influence phenotypic selection [37].

Furthermore, recent advances in modeling capabilities have resulted in highly complex, patient calibrated models of DCIS [38, 39].

While modeling has helped elucidate mechanisms involved in several mammary gland related processes, much has focused on formation of and transition to DCIS in a fully formed duct, instead of the behavior of the normal TEB and mammary gland ductal development. Recently, an experimentally-validated population-based continuum model to study mammary ductal elongation during pubertal development has been presented [1]. While this baseline model presents the first work on modeling ductal elongation using actual experimental data, it lacks a description of spatial heterogeneity, specific cell type localizations, cell-cell interactions and signaling. Here, we have implemented a hybrid ABM to study how endocrine and paracrine signaling within the normal TEB environment is involved in cellular proliferation and differentiation during pubertal development of the mammary gland, and how apoptosis events are involved in the formation of the lumen and influence ductal elongation rates. By gaining a more complete picture of how the healthy TEB functions, we are able to quantitatively examine how cellular phenotypic distribution, population size, proliferation and differentiation potentials, and the influence of endocrine and paracrine signaling systems and their effects on observed ductal elongation rates. Here, we describe methods for developing the model and provide biological insights we have observed. In the future, we plan to use this model to study how perturbations in endocrine and paracrine signaling and cellular phenotype proliferation and differentiation probabilities may contribute to developmental abnormalities observed in the pubertal mammary gland.

III. Hybrid Modeling Methods

We have developed a framework for multiscale hybrid modeling in C++ through implementation of a hybrid of partial differential equations (PDEs) and ABM. PDEs are solved with the finite element method (FEM), and used to model biologically relevant molecular distributions, including diffusion of important molecules from the surrounding tissue (oxygen and estrogen) and diffusion of growth factor (i.e., AREG) produced in the TEB by cells. Agents represent cells discretely, and have the capability to model many aspects of cellular function, including proliferation, migration, differentiation, apoptosis, and cell-cell signaling. Agents also modify the environment around them; for example, agents probe the oxygen concentration at their physical location from the FEM solution, and either undergo hypoxia induced necrosis (if oxygen concentration is insufficient to maintain cellular function; however, in our mammary gland model, necrosis does not occur (or is very rare) because all possible locations a cell may occupy within the TEB are well within the Krogh length from the oxygen supply at the TEB outer boundary) or consume some of the available oxygen as necessary to maintain homeostasis, modifying the FEM

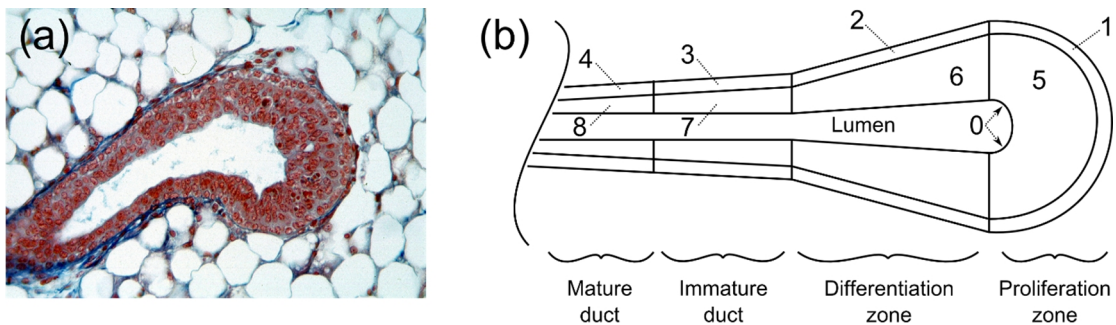


Figure 4.2: TEB and schematic of computational domain. (a) Microscopic view of the TEB (courtesy of Dr. Helen Hathaway, University of New Mexico). (b) Schematic of regions within the TEB. Regions 1-4 compose the myoepithelium, 5-8 compose the lumen, and 0 is the lumen-formation region. Definition of the regions was adapted from [1].

solution at their location accordingly. **Figure 4.2** describes the computational domain, with TEB geometry based on measurements from murine models [1].

i. Continuum partial differential equation component

Small molecule movement within the computational domain is described according to the reaction-diffusion equation form:

$$\frac{\partial u}{\partial t} = D\nabla^2 u + R(u), \quad (1)$$

Where u is a substrate concentration normalized by its maximum/saturation level, D is the diffusion coefficient of the molecule of interest and $R(u) = U(u) - L(u)$ is a reaction term to account for molecular production/consumption $U(u)$ and degradation $L(u)$. The diffusion coefficient of oxygen in tissue has been reported over a wide range, from 10^{-4} to 10^{-8} cm²/s [40]. In light of this large reported range, we take the somewhat central value of $2.57 \cdot 10^{-6}$ cm²/s from [41] in our specific model. Diffusion coefficients of estrogen and AREG are estimated (as corresponding data are not available in the literature) from reported diffusion coefficients of similar molecules (See **Table 4.1**). Briefly, AREG diffusion coefficient was estimated relative to published values for similar molecules (i.e. EGFR), while estrogen diffusion coefficient was estimated using both Graham's law and linear interpolation, as these methods gave estimates that were reasonable relative to other values. We note that these estimated values, while estimates, are taken to be reasonable relative to the large reported range of diffusion coefficient for oxygen. For the reaction

term $R(u)$, we assume negligible molecular degradation comparing to the primary molecular production/consumption by cells, i.e., $|L u| \ll |U u|$. More specifically,

$$R(x, u) = U(x, u) - L(u) = \pm \sum_{i=1}^N \lambda_i H(r_i - |x - a_i|) u - L(u), \quad (2)$$

where a_i and r_i are the central position and radius of cell i , respectively, $H(x)$ is the Heaviside function, and λ_i is a defined consumption or production per-volume rate of the substrate by cell. The positive sign represents production, and the negative sign consumption. In the current model implementation, we have made the assumption that all cells of similar phenotypes have the same λ values for each molecule of interest (i.e. all ER+ cells uptake estrogen at the same volume rate, and all cells have the same per volume oxygen consumption). In future modeling efforts, this assumption will be relaxed in order to study the effects of cell heterogeneity and the loss of function within healthy cells to study the effects of changes in signaling intensity in the transition to a cancerous disease state.

Biologically, $L(u)$ represents molecular sinks separate from molecular consumption in routine cellular functionality, i.e. unconsumed molecules in/on cells lost to apoptotic processes or molecular consumption by receptors/pathways other than the primary pathways in the model. We include $L(u)$ in the model for completeness of the mathematical description of the biological process and for future considerations where the primary consumption pathway may possibly be blocked. Molecular concentration profiles are also modified locally by agents due to molecular production or consumption, which are imposed discretely on the solution (as described in Eq. 3 below), as determined separately from the reaction term. For externally supplied molecules (i.e. oxygen and estrogen), we assume constant and homogeneous saturated concentrations in the surrounding tissue through

blood. These molecules enter the computational domain through imposition of Dirichlet boundary conditions ($u = 1$) at the outer boundary of the TEB. On the other hand, we assume that molecules produced by agents within the TEB (i.e., AREG) are free to diffuse throughout the simulated domain based on the conditions specified in the associated reaction-diffusion equation. Hence, far-field homogeneous Neumann boundary conditions have been implemented in this case, and molecular concentration attenuates towards a steady-level at the far field.

Time-dependent solutions for diffusion profiles of oxygen, AREG, and estrogen are obtained numerically using FEM. FEM solutions are obtained with Sundance [42], a finite element solver available as part of the Trilinos Project developed by Sandia National Laboratory. Solutions are obtained in two dimensions on a triangular mesh generated with Telis meshing software. The Dirichlet and Neumann boundary conditions are implemented as essential and natural boundary conditions in FEM, respectively. Continuum FEM solutions are modified discretely based on local agent consumption or production of the corresponding molecule across the computational domain. Molecular consumption and production by the whole volume of an agent are assigned to its center of mass and quantified phenomenologically (when unavailable from the literature) in normalized units. This hybridization of contributions from the discrete component into the continuum solutions is accomplished numerically by imposing Dirac delta modifications to the continuum solution profile at the mesh nodes. The magnitude of node modifications is determined by sorting agents in a Voronoi tessellation (a method of sorting where all agents that are closer to a node than any other node are associated with that node, and noting that the entire cytoplasmic volume of each agent is assigned to the Voronoi cell that contains

the agent's center of mass) around the node and then averaging the FEM modification magnitude (calculated as a per volume rate) of each agent nearest to that node, as described in the following equation:

$$U u = \frac{\sum_{i=1}^n \lambda_i u \int_{-\infty}^{\infty} \delta(x - a_i) dx}{n}, \quad (3)$$

where n is the number of agents in a Voronoi cell. Here we assume that the agents equally divide the Voronoi volume, and thus contributions from agents (cells) of different phenotypes in the same Voronoi cell are averaged. The computational domain was discretized in the same order of magnitude as agent radius, as the simple TEB geometry (which does not vary much over time and from animals to humans [43, 44]) does not possess any features requiring local mesh refinement, while both numerical and ABM time step discretization are equal (set to be 30 minutes of simulated time in all results shown; at each time step, the PDE is solved first; thus we integrate the hybrid model using a semi-implicit method by lagging the cell positions). A separate FEM solution is obtained for each molecule of interest.

ii. *Discrete agent-based modeling component*

Agent distribution is lattice-based in a hexagonal close packed conformation in two dimensions. Growth within the TEB is proliferation-driven, where proliferating agents must displace their neighbors to create room for the new daughter (if there is not already room to divide left by an agent that has undergone apoptosis). To keep our focus on the TEB, we describe the model on a moving frame that moves at the same speed as the duct elongation. Hence, our computational domain contains a fixed section of the TEB, as

illustrated in **Figure 4.2b**. Cells exit through the open end of the mature duct and out of the modeled domain but are counted to estimate the duct elongation rate. Moreover, as our primary goal is to understand the longitudinal cell distribution and the ductal elongation resulting from endocrine and paracrine signal mediated cell proliferation, we reduce the full three-dimensional structure of a TEB to its two-dimensional cross-section by assuming cylindrical symmetry. When a cellular proliferation event occurs, the daughter cell is placed at a neighbor position of the mother within the appropriate region of the TEB. If the selected position is already occupied, the occupant is displaced to make room, and in turn further displaces one of its neighbors. Cells are assumed infinitely compliant to displacement, so the process continues until an agent is displaced either into an unoccupied position previously cleared by apoptosis or out of the computational domain. Because we do not currently model the entire mammary gland, any agents displaced out of the computational domain are counted by phenotype and removed from the simulation.

Apoptosis within the TEB model occurs stochastically, with higher apoptosis percentages (14.5% per cell cycle) proximal to the lumen-formation region (region 0 in **Figure 4.2b**) and lower apoptosis percentages (7.9% per cell cycle) distal to the lumen-formation region, based on apoptotic populations observed in the murine mammary gland [45]. Here, we use the reported percentage of cells undergoing apoptosis at a snapshot as the apoptosis percentage in one cell cycle, based on the observation that apoptosis and subsequent clearance by macrophages is a rapid process [46]; accordingly we take clearance of apoptotic cells time to be roughly the same as or less than our cell cycle time (see **Table 4.1**). Positions freed by an apoptosis event may be filled by agents displaced from a proliferation event elsewhere in the TEB or at a later time step. Agents extract the

values of molecular concentrations at their location for every time step and use these values to make decisions, and also modify molecular concentrations as a result of molecular uptake or production. Myoepithelial cells are ER-, while cells in the lumen may be ER+ or ER-. ER+ cells uptake estrogen, reducing the concentration at their locations, and respond to estrogen stimulation by proliferating and producing AREG, increasing local AREG supply. ER- cells may be stimulated into proliferation if the concentration of AREG satisfies a proliferation threshold. For both ER+ and ER- phenotypes, proliferation may only occur if they are not entering necrosis or apoptosis. Progenitor cells may also differentiate due to extended quiescence (as is commonly accomplished in confluent cells in vitro).

Cellular proliferation rates are bounded by cell cycle duration, which has been demonstrated to be in the 16 hour range in the case of mammary gland [19]. To satisfy this proliferation threshold, agents count the time since their last mitosis event, and may not proliferate again until at least 16 hours of simulated time has passed. Both the molecular signaling thresholds (AREG for ER- and estrogen for ER+) and the cell cycle time threshold are implemented as binary step functions, where the proliferation of an agent is disallowed below the threshold. Upon satisfaction of the thresholds, an agent with a stem or progenitor phenotype may proliferate with a given probability. This proliferation probability is set to 100% for this study, as we focus our investigation on the effects of phenotypic distribution and AREG and estrogen thresholds. In future development, this probability can be regulated by various incorporated microenvironment conditions, such as the oxygen concentration, or to include the effects of abnormal behavior from perturbation from a healthy to a disease state. Subsequent to a proliferation event, the new

daughter cell displaces one of the agents around the mother cell according to the cellular displacement algorithm described above, moving the TEB forward. The phenotype of the daughter is determined stochastically and is based on mother type and partially on mother location.

To quantify the probability of the cell fate, we divide the TEB into proliferative, differentiation, immature, and mature ductal zones ([1] also see **Figure 4.2b**), based on a commonly adopted hypothesis. The proliferative zone is thought to be composed of proliferative body cells (region 5) and myoepithelial progenitors (region 1), and is capped

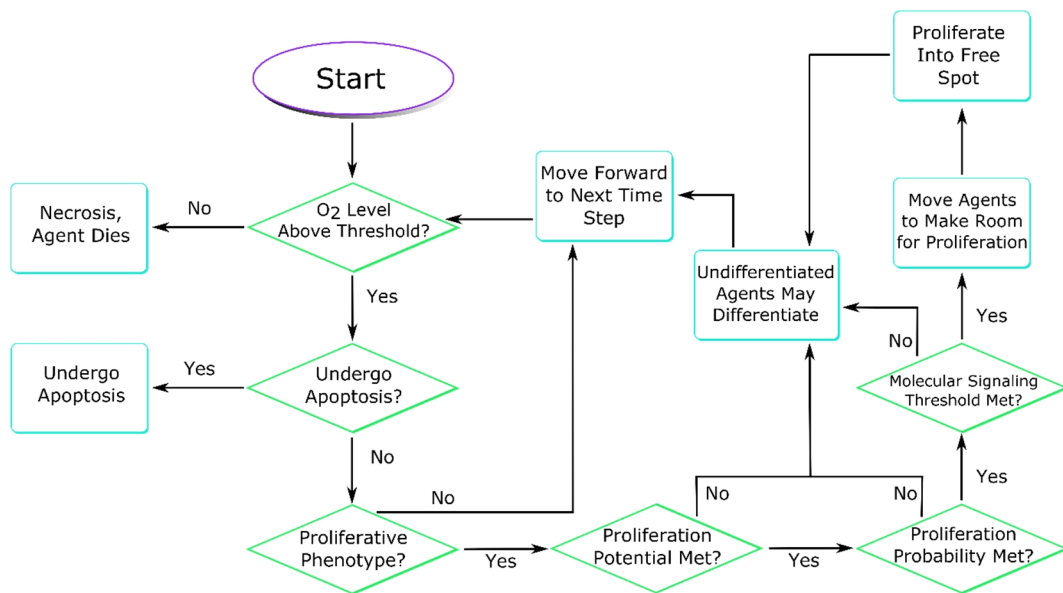


Figure 4.3: Agent phenotype decision flowchart. At each time step, agents query their environment to find the values of molecular concentrations of interest. If (i) agents do not enter necrosis, (ii) are not chosen to under apoptosis, (iii) they are progenitors, and (iv) it has been at least one cell cycle since they have proliferated, then they may proliferate, provided that a stochastic proliferation probability and molecular signaling thresholds are met. Agents that are not progenitors or do not meet the proliferation criteria wait for the next time step. Proliferation events displace surrounding agents to make room for the daughter, either filling a location freed by an apoptosis event or displacing an agent out of the computational domain as the TEB moves forward.

with cap cells. These are followed by regions with increasing number of differentiated cells as cells become farther away from the TEB tip [25]. Progenitors in the proliferation zone always proliferate symmetrically, while progenitors in the differentiation zone have a reduced symmetric proliferation probability (see **Table 4.1**), which is further reduced 25% (arbitrarily) after the mother moves out of the differentiation zone. Baseline symmetric proliferation probabilities are shown in **Table 4.1**. A more complete description of agent decision pathways is shown in **Figure 4.3**. In our model, stem cells may be either multipotent or unipotent, as determined by their location within the TEB. To maintain phenotypic separation between the lumen and myoepithelium, stem cells within these regions are restricted to unipotent phenotype, where they may only give rise to the surrounding phenotype. Stem cells at the leading cap of the TEB tip are allowed to be multipotent, giving rise to either unipotent stem or progenitor daughters, as determined by which region the daughter is placed into. We note that for the purpose of simplifying visualization output, we show both multipotent and unipotent stem cells using the same color (**Figures 4.1, 4.4 and 4.9**).

IV. Results

We have enlisted, to our best knowledge, literature-supported values into our model studies whenever possible. When these values were not available, we sought to determine a baseline value for the model parameter that result in model behavior in agreement with physically verifiable values. In brief, baseline values must result in biologically relevant ductal elongation rates (previously reported at 500 μm per day [47, 48]), cellular distributions, and reasonable phenotypic transition from the highly proliferative zone

within the TEB to the mature, mostly differentiated duct. The chosen baseline values as

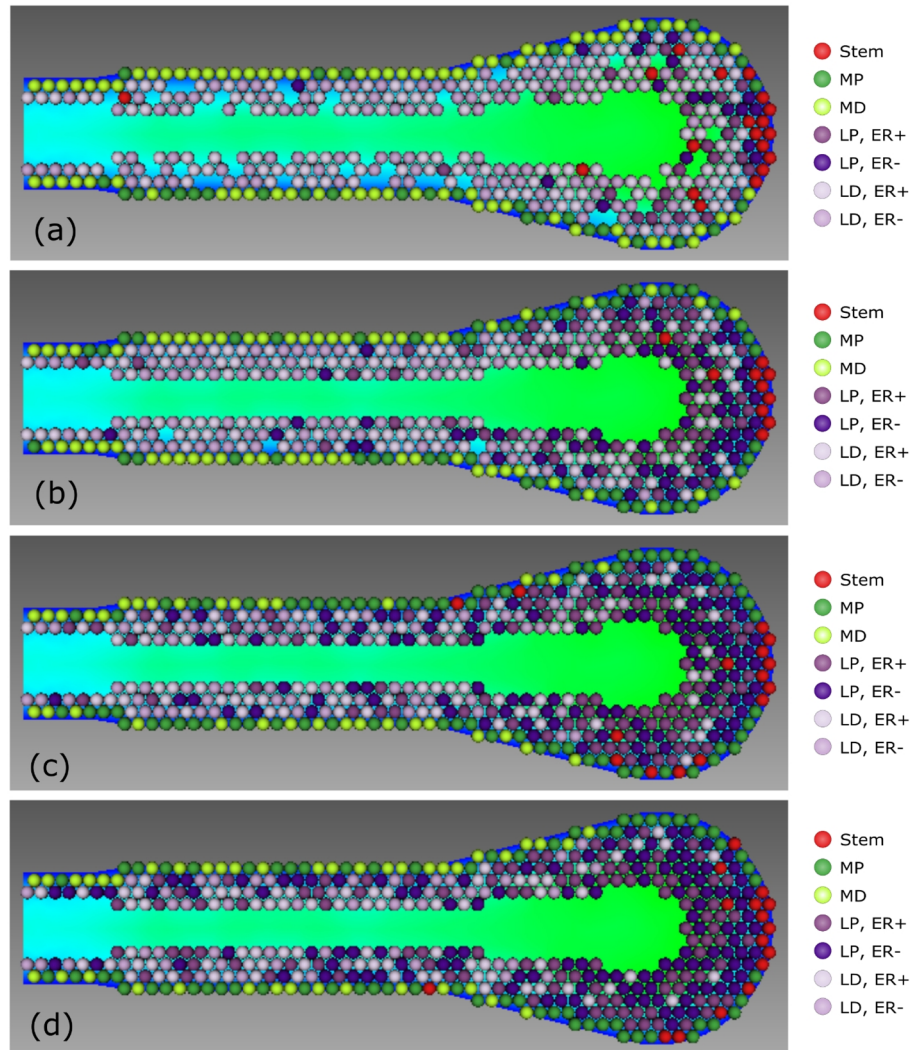


Figure 4.4: Effects of proliferation cycles before differentiation. (a) One cycle before differentiation results in progenitor depletion, and apoptosis events overtake proliferation, disrupting TEB morphology, seen here as numerous holes disrupting confluency in the TEB. Morphology disruption shown is after three simulated cell cycles. (b) Two cell cycles before differentiation maintains TEB homeostasis, with noticeable differentiated population within the proliferation zones. (c) Three cycles before differentiation reduces differentiated population in the proliferation zone and results in increased progenitor population within the differentiation zone. (d) Four cycles before differentiation; the proliferation zone is now mostly free of differentiated agents. Background colors within the TEB show a graphical representation of the numerical solution of oxygen concentration, with blue corresponding to higher normalized concentration (up to 1.0) around the boundary and green corresponding to the lower concentration. See the online version of this article for better distinction of the phenotypic color codes.

quantified from the literature or quantified in agreement with literature-supported values are summarized in **Table 4.1** (we note that normalized and/or phenomenologically determined values are not included, as they are not directly translatable to biologically measured values). In all simulations described, any model parameter not explicitly varied was assigned the baseline value.

i. Cell cycles before differentiation

Within the TEB, myoepithelial and luminal progenitors are restricted in the number of mitosis cycles they may undergo before differentiation into a non-progenitor phenotype, while stem cells are allowed to proliferate indefinitely. In our model, if progenitor cells were only allowed to proliferate once before differentiation, it was insufficient to maintain a progenitor population, resulting in growth arrest and loss of confluency in the TEB (**Figure 4.4a**). Without a sufficient progenitor population, apoptosis events dominated and the TEB cellular population was diminished, with greatly arrested ductal elongation rates and disruption of correct organ structure. Conversely, in the case of four proliferation cycles before differentiation (**Figure 4.4d**), many progenitors did not remain in the TEB for sufficient cell cycles to differentiate, resulting in mature duct with a biologically irrelevantly large progenitor cell population. Reduction to three proliferation cycles before differentiation (**Figure 4.4c**) reduced this number, with fewer than 30% of cells entering the mature duct with progenitive phenotype, and reduction to two proliferation cycles before differentiation (**Figure 4.4b**) further reduced the percentage of progenitor cells in the mature ductal zone to around the 10% range. This result is in good accordance with the literature, where percentages of progenitor cells within the mature mammary gland are

found to be under 10% (or slightly over 10% for the nulliparous gland) [49]. Accordingly, we identify 2-3 ($2x-3x$) cycles before differentiation (a quantity we will henceforth refer to as the *proliferation cycle threshold*) as the most likely to be biologically relevant, and this is also in agreement with experimental measurements as well [1]. Together, we have determined that TEB growth is highly dependent on the number of progenitor proliferation cycles before differentiation. Note that because we only model the TEB, we do not consider differentiation events that may occur after cells enter the mature duct.

ii. *Symmetric vs. asymmetric division*

The phenotypic fate of daughter cells has been reported to contain high heterogeneity amongst different tissues and developmental stages. Our model allowed us to specify the stochastic probability that a progenitor will divide symmetrically (increasing the progenitor population) or divide asymmetrically, giving rise to a differentiated daughter. We have made the assumption that, at the onset of mammary gland pubertal growth, all progenitors may undergo the maximum allowed number of proliferations before differentiation. This resulted in initially increasing numbers of progenitors as new cells generated from symmetric proliferation events displace differentiated cells that were initially seeded at the beginning of the simulation until the proliferation cycle threshold was reached (see **Figure 4.5**). Subsequent to reaching this threshold, differentiation events reduced progenitor population and the entire cell population transitioned towards progenitor/differentiated homeostasis.

In the model, cell agents differentiate immediately upon hitting their proliferation cycle threshold. In the case of no signaling threshold, proliferation events were more frequent relative to the signaling limited case, with progenitors always proliferating as soon as they had waited one cell cycle (provided all other conditions were met). Increased proliferation events also led to an increase in differentiation events as cells reached the proliferation threshold, and thus a faster transition to population homeostasis (**Figure 4.5a,b**), resulting in reduced temporal fluctuation of total progenitor population count in

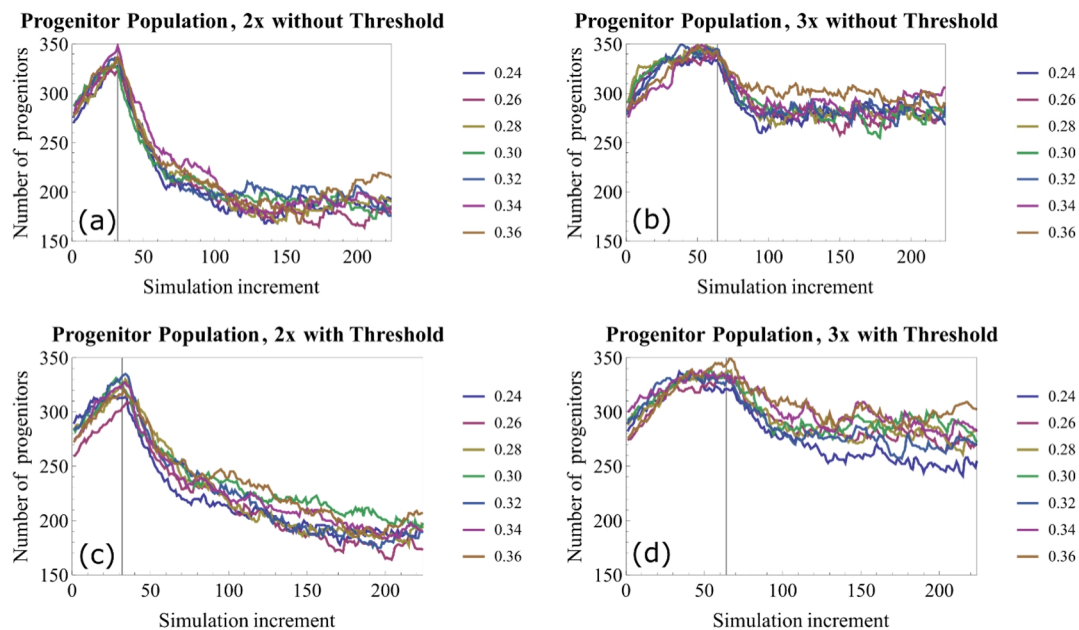


Figure 4.5: Progenitor population within the TEB with different symmetric proliferation probabilities (1.0 = 100% symmetric proliferation). (a,b) Progenitor population vs. simulation iteration without signaling threshold in place. (c,d) Progenitor population after incorporation of signaling thresholds. 3x proliferation events maintains a larger progenitor population within the TEB relative to 2x. In each case, progenitor population is seen to increase until differentiation events start (indicated by vertical lines), reducing the progenitor population until it reaches homeostasis. Each curve represents one simulation, and each simulation step corresponds to 30 minutes of simulated time, thus 32 simulation increments correspond to one simulated cell cycle.

subsequent cell cycles. As expected, higher percentages of symmetric proliferations resulted in higher total percentage of progenitors in the TEB (**Figure 4.5**). Ductal elongation rates were lower for two proliferation cycles relative to the three proliferation cycle case (**Figure 4.6a,b**) because increased proliferation cycles maintain a larger progenitor population, allowing for more proliferation events per cell cycle.

iii. *Signaling thresholds*

Perturbation simulations of the percentage of symmetric proliferation events were then repeated with molecular signaling threshold restrictions in effect (**Figure 4.6c, d**), where baseline signaling thresholds were set equal to continuum molecular concentration

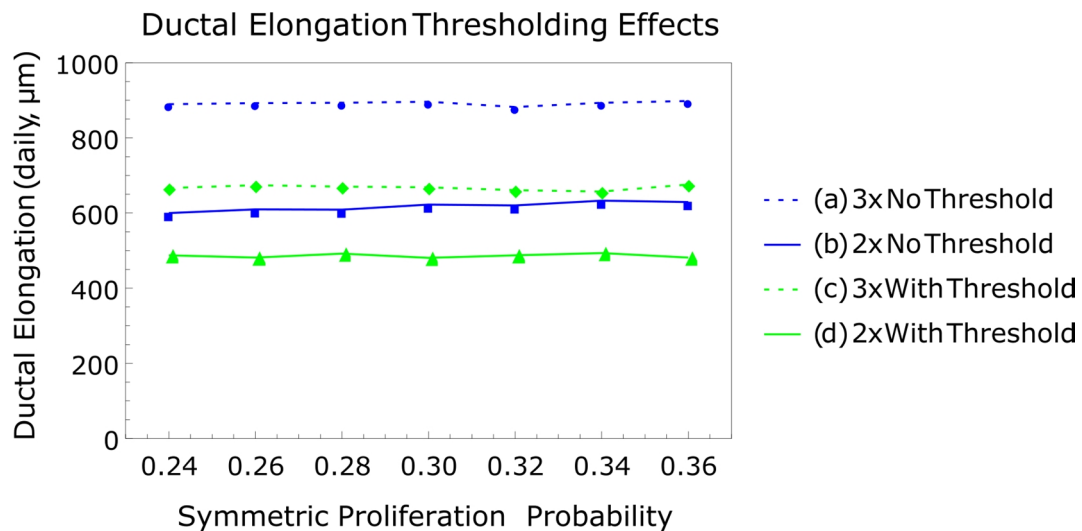


Figure 4.6: Ductal elongation growth rates with 2x and 3x proliferation cycles before differentiation with symmetric proliferation probability perturbation (1.0 = 100% symmetric proliferation). (a,b) Daily elongation rates without molecular signaling threshold and (c,d) daily elongation rates with molecular signaling threshold. In both cases, higher elongation rates are observed with 3x proliferation cycles before differentiation, and molecular signaling thresholds reduce elongation rates relative to the unregulated, purely proliferative case. All plots show elongation rates observed over 7 simulated cell cycles.

(set with the same normalized value for all simulations at time $t=0$; molecular perturbation values are relative to this initial concentration). Interestingly, varying progenitor symmetric proliferation percentages did not have an impact on elongation rates, as observed from the uniform simulated elongation rates for each parameter variation case (**Figure 4.6a-d**). The number of cycles before differentiation still influenced elongation rates, as higher progenitor populations allowed for more proliferation events both in the presence and absence of a molecular signaling threshold.

We then sought to gain insight on the effects of specific perturbations in molecular parameters (i.e., thresholds for estrogen and AREG) on model output (i.e., ductal elongation rate). Initially, thresholds for both molecular parameters were varied together (**Figure 4.7**). Signaling threshold was found to closely control simulated ductal elongation rates. **Figure 4.7** reveals how the threshold affects ductal elongation rates. An increase of

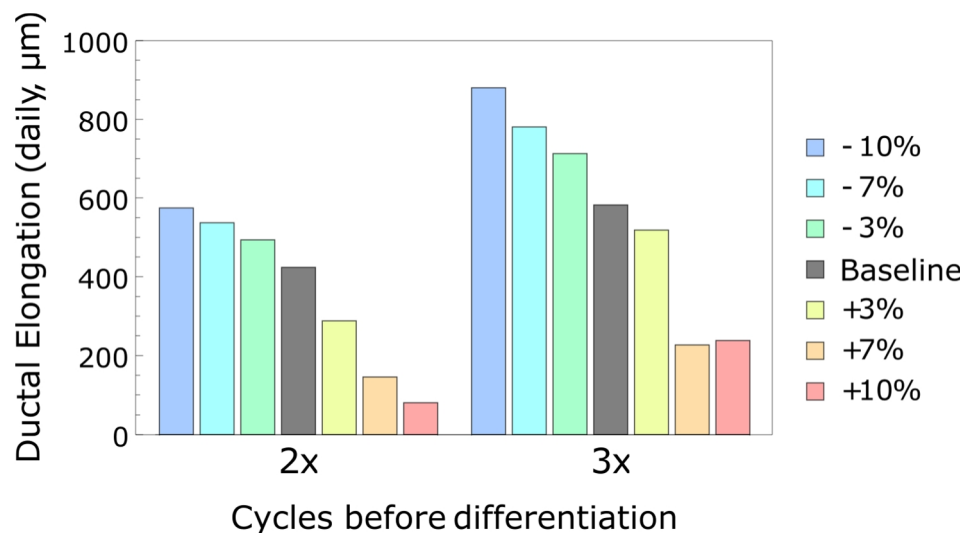
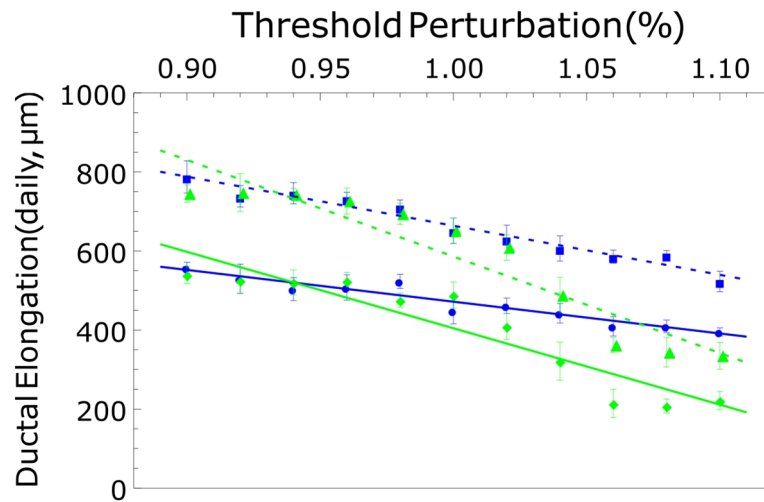


Figure 4.7: Effects of synchronized $\pm 10\%$ estrogen and AREG signaling threshold variation on ductal elongation rates. Proliferation events are sensitive to molecular signaling thresholds when both estrogen and AREG thresholds are perturbed in unison (shown here). Higher (+) thresholds inhibit proliferation events, stunting ductal elongation rates, while lower (-) thresholds are less restrictive, resulting in more proliferation events and higher elongation rates. All plots show elongation rates observed over 7 simulated cell cycles.

as little as 7-10% above the baseline led to a 60-80% reduction in ductal elongation rate (from 423.75 to 80.25 $\mu\text{m}/\text{day}$ for 2x before differentiation, and from 582.2 to 226.9 $\mu\text{m}/\text{day}$ for 3x), which is low compared to the established level in literature, where pubertal ductal elongation rates have been reported to be around 500 $\mu\text{m}/\text{day}$ [47].

Simulations were then conducted with independent perturbation of each individual molecular threshold ($\pm 10\%$ signaling threshold; **Figure 4.8**). One threshold was subjected to $\pm 10\%$ perturbation, while the other remained fixed at the baseline value (see **Table 4.1**). Ductal elongation rates were reduced at higher thresholds for both cases, with greater reduction in the case of high estrogen thresholds relative to high AREG thresholds. Linear best-fit curves were generated for the ductal elongation rate data to provide quantification of threshold growth arrest effects. Then, the magnitude of the slope of each regression line was used as a measure to estimate the rate of change of output for one unit of change in input; the greater the magnitude of the slope, the greater the rate of change, and thus the bigger impact the parameter has on model output. As a result, for both cases, estrogen signaling was found to have more impact on ductal elongation rate than AREG signaling (slope magnitude (AREG vs. estrogen perturbation) increased from 804.36 to 1933.98 for the 2x case, and from 1242.10 to 2442.78 for the 3x case). In the case of high AREG thresholds, ER- cells show significant population decrease (due to reduced proliferation events), while ER+ cells proliferate uninhibited at their baseline threshold (data not shown). Imposition of high estrogen thresholds, however, resulted in reduction of proliferation events in both ER+ and ER- phenotypes.



— (a) AREG 2x, $\beta = -804.36$, $p < 0.001$ - - - (b) AREG 3x, $\beta = -1242.10$, $p < 0.001$
 — (c) Estrogen 2x, $\beta = -1933.98$, $p < 0.001$ - - - (d) Estrogen 3x, $\beta = -2442.78$, $p < 0.001$

Figure 4.8: Effects of independent $\pm 10\%$ signaling threshold variation on ductal elongation rates. AREG restricted growth (a, b) shows reduced daily elongation reduction relative to estrogen restricted ductal elongation. Estrogen restricted growth resulted in more than twice the ductal elongation reduction relative to the AREG restricted case. Each data point represents the mean of 5 simulations with standard deviations; linear best-fit curves are shown as dashed lines. β : the slope of a regression line.

iv. *Cell types in each region*

We have quantified the types of cells in each region (see **Figure 4.2b** for region definitions) through longer simulation runs (two weeks of simulated growth) using baseline values as identified in **Table 4.1**. At the end of each simulation step, agents of each type were counted across the computational domain. Simulation results are shown in **Figure 4.9**. Regions closer to the TEB tip (i.e., regions 1 and 5) maintained larger populations of progenitors than differentiated agents, with 3x proliferation before differentiation maintaining larger total progenitor populations relative to the 2x case. In the 2x before differentiation case (**Figure 4.9a**), differentiated population quickly overtook progenitor

population in regions 2 and 6. In regions 3 and 7 cellular population was primarily differentiated. For the 3x proliferation before differentiation case (**Figure 4.9b**), increased proliferation events slowed the transition from progenitor dominated to differentiated populations, as differentiated populations did not overtake progenitors until

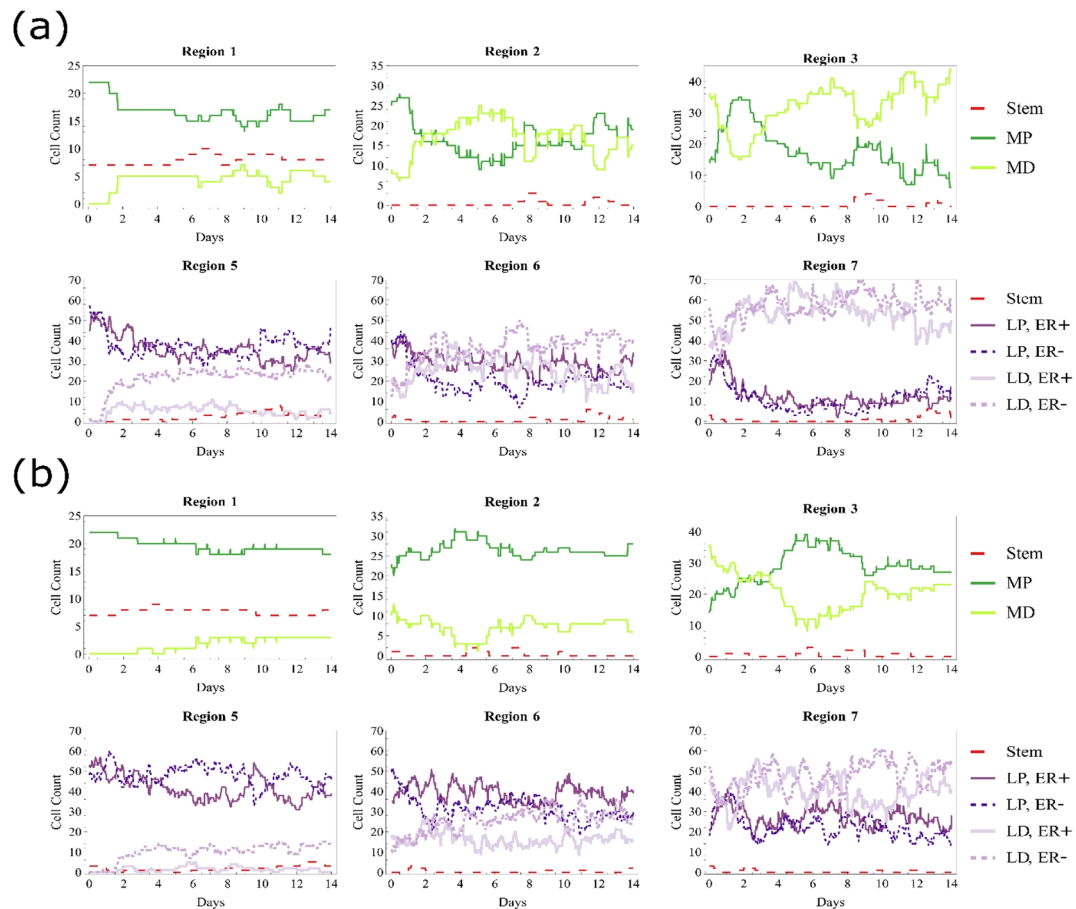


Figure 4.9: Cell types in each region for (a) two cycles before differentiation and (b) three cycles before differentiation (cell counts in the mature duct not shown). Data shown in both cases are taken from one sample simulation with baseline molecular signaling thresholds in effect, and myoepithelial plot colors correspond to cellular phenotype coloration shown in **Figure 4.1**, while the luminal color scheme has been simplified to increase readability. Regions closer to the TEB tip contain primarily progenitors with some differentiated agents that have hit the proliferation threshold limit, while regions farther from the TEB tip have increased differentiated populations. More proliferation cycles before differentiation maintain larger progenitor populations in all regions.

regions 3 and 7. In both cases, phenotypic population was volatile in the short portion of mature duct that we model (i.e., regions 4 and 8), and many of the cells that move into this region move out of the computational domain before they are counted; accordingly cell counts in these regions are not shown. Note that because counts were taken at the end of each simulation step, it is possible that an agent may have passed through a region in the simulation step and accordingly not been counted during its short residence that region.

V. Discussion

Through a hybrid multiscale ABM, we have explored the contribution of cellular phenotypic hierarchy, phenotypic distribution, and the effects of endocrine and paracrine signaling on ductal elongation rates within the developing mammary gland. We examined the effects of proliferation cycles before differentiation, symmetric vs. asymmetric proliferation probabilities, and the influence of molecular signaling threshold on elongation rates and phenotypic populations within the TEB. Under our assumption that all daughters within the proliferation zone will be progenitors, we demonstrate that elongation rates were driven primarily by proliferating population renewal within the proliferation zone. Molecular signaling thresholds were found to provide consistent ductal elongation rate regulation, with elongation rates shown to be sensitive to molecular signaling intensity. The model also demonstrated that 2-3x cell proliferation cycles before differentiation accurately reproduced biologically relevant ductal elongation rates and cellular phenotypic distributions within the TEB; this result confirms previous experimental data as well [1]. Achieving a primarily differentiated population within the mature mammary gland necessitates rapid phenotypic transition from primarily progenitor phenotypes within a

short residence time in the TEB. We find that reduction of symmetric proliferation events in the differentiation zone in combination with the proliferation cycle threshold was sufficient to induce this phenotypic transition, in agreement with literature reported values [49].

In our simplified model of cellular phenotypic hierarchy within the TEB (**Figure 4.1**), we observed that the number of proliferation cycles before differentiation in progenitor cells plays an important role on simulated replication of biologically correct TEB growth and functionality. Inadequate proliferation cycles before differentiation (**Figure 4.4a**) resulted in a TEB that rapidly exhausts its supply of progenitors, all but halting mammary gland growth and disrupting proper TEB structure as the few remaining progenitors and stem cells competed with apoptosis events to maintain the proper gland structure. This ultimately resulted in loss of confluency, and is seen as holes that have developed throughout the TEB in **Figure 4.4a**. Conversely, greater than 3 proliferation cycles before differentiation (**Figure 4.4d**) prevented adequate time for many progenitors to differentiate prior to exiting the TEB, resulting in biologically unrealistic numbers of progenitors in the mature duct. Our results show that 2-3 proliferation cycles before differentiation (**Figure 4.4b,c**) resulted in mammary gland growth which is in good agreement with the literature, both in terms of ductal elongation rates [47, 48] and phenotypic populations within the mature gland [49]. While it is likely that the number of proliferation cycles will vary from cell to cell *in vivo*, we demonstrate evidence that the distribution is likely centered around the 2-3 proliferation cycles range.

Effects from changing the stochastic probability of symmetric divisions was found to be minimal, likely due to short cellular residence times within the TEB (see **Figure 4.6**).

At 2x, cells average three cell cycles in the TEB before being displaced into the mature duct and out of the computational domain, while average residence time is reduced to two cycles in the 3x case. In both cases, residence time in the TEB is shorter than or equal to the number of cycles necessary for a cell to differentiate due to hitting the proliferation threshold, thus minimizing the effects of different symmetric proliferation probabilities. Ductal elongation rates were consistently higher in the 3x case due to larger progenitor populations, with increased symmetric proliferation events contributing only minimally to the higher elongation rates.

Our results demonstrate that imposition of signaling molecule thresholds onto the proliferation with apoptosis model resulted in reliable TEB cellular proliferation and mammary gland ductal elongation rate regulation. The ductal elongation rates were lower than the unrestricted case of pure proliferation in the absence of any signaling threshold (**Figure 4.6c, d**). This indicates that signaling thresholds may act as an elongation rate regulation mechanism in the pubertal mammary gland by reducing the cellular proliferation rates. The observed reduction of proliferation events and ductal elongation rates due to molecular threshold effects implies that the mammary gland has the potential to elongate at faster rates than reported in the literature [47] if molecular signaling is increased in intensity, and this can occur with a proliferation cycle threshold as low as two cycles before differentiation. It should be noted that molecular production rates and boundary values, uptake rates, diffusion constants, and signaling threshold are not independent. All have a direct influence on and contribution to the time dependent solutions of the molecular profiles. Unfortunately, we have not been able to obtain literature-based quantified values

for all parameters; thus, we have calibrated a set of parameter baseline values that gave rise to biologically realistic elongation rates and phenotypic distributions.

Ductal elongation rates were found to be consistently reduced with higher proliferation thresholds, and, under the conditions implemented in the simulations presented here, cellular proliferation rates exhibited higher sensitivity to increased estrogen-mediated proliferation than in the AREG-mediated case. When cellular proliferation events within the ER- phenotype were restricted by the AREG threshold, ER+ phenotype cells were able to proliferate as normal, as estrogen signaling is not affected by downstream signaling events. However, restriction of proliferation events of the ER+ phenotype due to higher estrogen thresholds constituted an upstream interruption in the signaling pathway, and lead to interruption of downstream AREG mediated proliferation in the ER- population. Initially, estrogen-mediated reduction in ER+ proliferation events resulted in increased ER- population within the TEB as the ER+ proliferation events decreased. This population shift lead to a change in AREG signaling effectiveness, as AREG production decreased concurrently with an increase in AREG consumption. Ultimately, this resulted in reduced ER- proliferation events due to upstream reduction of ER+ proliferation and AREG production. Thus, our results indicate that, under simulation conditions as presented here, mammary gland ductal elongation is more sensitive to disruptions in estrogen signaling than AREG signaling, as estrogen signaling disruption ultimately decreases proliferation in both ER+ and ER- phenotypes, while AREG signaling disruption only affects the ER- population. Ductal elongation rates were also observed to be more sensitive to estrogen signaling in the 2x case relative to the 3x case. It is likely that the larger progenitor population maintained by the greater number of proliferation

cycles is able to offset some of the cellular proliferation restriction effects of reduced signaling molecule intensity.

Cell types in each region were found to be variable, with stochastic events resulting in population shifts over time. However, trends can clearly be seen, with progenitor population consistently decreasing farther away from the TEB tip, primarily due to differentiation events after progenitors reach their maximum cycle before differentiation, and with differentiated population also subsidized from decreased symmetric proliferation events as progenitors are distanced from the TEB tip. Increased proliferation cycles before differentiation resulted in larger progenitor populations in each region of the TEB, including greater percentages of progenitors left behind in the mature duct trailing the TEB. While two proliferation cycles before differentiation resulted in progenitor populations in the mature duct closer to values reported in the literature, this likely does not elucidate the full picture, as additional differentiation events after agents enter the mature duct may have downstream effects on cellular population distribution in the fully formed mature gland.

It should be noted that ductal elongation rates predicted with a two-dimensional model may be lower than elongation rates possible in the three-dimensional case, as in the 3D case the ratio of progenitors in the TEB to number of cells necessary to elongate the duct is higher. Similarly, under identical boundary, diffusion, and molecular uptake conditions, internal molecular concentrations would also be higher in a 3D model. However, this simplified case sheds valuable insights onto the effects cellular differentiation pathways and phenotypic transition decisions play in the morphological development of the mammary gland. Future development of the model will transition to a three-dimensional computational domain and remove the restriction of on-grid agent

movement. A model of healthy organogenesis can also provide a jumping-off point for transition to disease state. In future computational experiments, we will incorporate another type of stem cell into the model (alveolar stem cells) and then break the rules that maintain homeostasis to seek insight into the signaling and phenotypic transitions involved in disruption of normal mammary gland development.

Model Parameter	Baseline Value	Reference
Necrosis threshold (normalized)	0.2	
D_{oxygen}	$2.5 \times 10^{-6} \text{cm}^2 \text{s}^{-1}$	[41]
D_{estrogen}	$2.45 \times 10^{-6} \text{cm}^2 \text{s}^{-1}$	*
D_{AREG}	$3.18 \times 10^{-7} \text{cm}^2 \text{s}^{-1}$	[50]**
Proliferation rate	≤ 1 per 16 hours	
Cell cycle time	16 hours	[19]
(Cell death + lysis) time	< 16 hours	[51]
Progenitor symmetric proliferation (regions 2,	30%	
Proliferation cycles before differentiation	2-3	
Stem cell symmetric proliferation probability	12%	[10]
Spontaneous differentiation probability	0.01%	
Apoptosis probability, proximal to lumen	14.5%	[45]
Apoptosis probability, distal to lumen	7.9%	[45]

Table 4.1: Baseline values of key model parameters. When not available in the literature, diffusion constants are interpolated from values from structurally similar molecules (*) or estimated from known values based on relative molecular weights (**). Other uncited values were determined from model calibration. Stem cell symmetric proliferation rate has been reduced 1% from the value reported in [10].

VI. Acknowledgements

This work has been supported in part by the National Science Foundation (NSF) Grant DMS-1562068 (V.C., Z.W.), the National Institutes of Health (NIH) Grant 1U01CA196403 (V.C., Z.W.), 5U54CA151668-05 (V.C.), the University of Texas System STARS Award (V.C.), the Deanship of Scientific Research (DSR), King Abdulaziz

University, under Grant no. (HiCi/54-130-35) (E.S., A.S.A., S.R.M., V.C.), and the Methodist Hospital Research Institute (V.C.). The funders had no role in study design, data collection and analysis, decision to publish, or preparation of the manuscript.

Conflicts of Interest Disclosures

The authors declare no conflicts of interest.

This chapter is reproduced with permission from: Butner, J.D., et al., *A hybrid agent-based model of the developing mammary terminal end bud*. J Theor Biol, 2016. **407**: p. 259-70. Full text available at <http://www.sciencedirect.com/science/article/pii/S0022519316302235>.

VII. Works Cited, Chapter 4

1. Paine, I., Chauviere, A., Landua, J., Sreekumar, A., Cristini, V., Rosen, J., and Lewis, M.T., *A Geometrically-Constrained Mathematical Model of Mammary Gland Ductal Elongation Reveals Novel Cellular Dynamics within the Terminal End Bud*. PLoS Comput Biol, 2016. **12**(4): p. e1004839.
2. Dontu, G., El-Ashry, D., and Wicha, M.S., *Breast cancer, stem/progenitor cells and the estrogen receptor*. Trends Endocrinol Metab, 2004. **15**(5): p. 193-7.
3. Visvader, J.E. and Stingl, J., *Mammary stem cells and the differentiation hierarchy: current status and perspectives*. Genes & Development, 2014. **28**(11): p. 1143-1158.
4. Shackleton, M., Vaillant, F., Simpson, K.J., Stingl, J., Smyth, G.K., Asselin-Labat, M.L., Wu, L., Lindeman, G.J., and Visvader, J.E., *Generation of a functional mammary gland from a single stem cell*. Nature, 2006. **439**(7072): p. 84-8.
5. Asselin-Labat, M.L., Shackleton, M., Stingl, J., Vaillant, F., Forrest, N.C., Eaves, C.J., Visvader, J.E., and Lindeman, G.J., *Steroid hormone receptor status of mouse mammary stem cells*. J Natl Cancer Inst, 2006. **98**(14): p. 1011-4.
6. Visvader, J.E. and Lindeman, G.J., *The unmasking of novel unipotent stem cells in the mammary gland*. The EMBO Journal, 2011. **30**(24): p. 4858-4859.
7. LaMarca, H.L. and Rosen, J.M., *Estrogen regulation of mammary gland development and breast cancer: amphiregulin takes center stage*. Breast Cancer Res, 2007. **9**(4): p. 304.
8. Clayton, E., Doupe, D.P., Klein, A.M., Winton, D.J., Simons, B.D., and Jones, P.H., *A single type of progenitor cell maintains normal epidermis*. Nature, 2007. **446**(7132): p. 185-189.
9. McKenzie, J.L., Gan, O.I., Doedens, M., Wang, J.C., and Dick, J.E., *Individual stem cells with highly variable proliferation and self-renewal properties comprise the human hematopoietic stem cell compartment*. Nat Immunol, 2006. **7**(11): p. 1225-33.
10. Giebel, B., Zhang, T., Beckmann, J., Spanholtz, J., Wernet, P., Ho, A.D., and Punzel, M., *Primitive human hematopoietic cells give rise to differentially specified daughter cells upon their initial cell division*. Blood, 2006. **107**(5): p. 2146-52.
11. Yatabe, Y., Tavaré, S., and Shibata, D., *Investigating stem cells in human colon by using methylation patterns*. Proceedings of the National Academy of Sciences, 2001. **98**(19): p. 10839-10844.
12. Osawa, M., Hanada, K., Hamada, H., and Nakauchi, H., *Long-term lymphohematopoietic reconstitution by a single CD34-low/negative hematopoietic stem cell*. Science, 1996. **273**(5272): p. 242-5.
13. Takano, H., Ema, H., Sudo, K., and Nakauchi, H., *Asymmetric division and lineage commitment at the level of hematopoietic stem cells: inference from differentiation in daughter cell and granddaughter cell pairs*. J Exp Med, 2004. **199**(3): p. 295-302.
14. Citron, M.L., Berry, D.A., Cirrincione, C., Hudis, C., Winer, E.P., Gradishar, W.J., Davidson, N.E., Martino, S., Livingston, R., Ingle, J.N., Perez, E.A., Carpenter, J., Hurd, D., Holland, J.F., Smith, B.L., Sartor, C.I., Leung, E.H., Abrams, J., Schilsky, R.L., Muss, H.B., and Norton, L., *Randomized trial of dose-dense versus*

- conventionally scheduled and sequential versus concurrent combination chemotherapy as postoperative adjuvant treatment of node-positive primary breast cancer: first report of Intergroup Trial C9741/Cancer and Leukemia Group B Trial 9741.* J Clin Oncol, 2003. **21**(8): p. 1431-9.
15. Bultje, R.S., Castaneda-Castellanos, D.R., Jan, L.Y., Jan, Y.-N., Kriegstein, A.R., and Shi, S.-H., *Mammalian Par3 Regulates Progenitor Cell Asymmetric Division via Notch Signaling in the Developing Neocortex.* Neuron, 2009. **63**(2): p. 189-202.
 16. Noctor, S.C., Martinez-Cerdeno, V., Ivic, L., and Kriegstein, A.R., *Cortical neurons arise in symmetric and asymmetric division zones and migrate through specific phases.* Nat Neurosci, 2004. **7**(2): p. 136-44.
 17. Kim, Y.H., Larsen, H.L., Rue, P., Lemaire, L.A., Ferrer, J., and Grapin-Botton, A., *Cell cycle-dependent differentiation dynamics balances growth and endocrine differentiation in the pancreas.* PLoS Biol, 2015. **13**(3): p. e1002111.
 18. Nomura, T., Gotoh, H., and Ono, K., *Changes in the regulation of cortical neurogenesis contribute to encephalization during amniote brain evolution.* Nat Commun, 2013. **4**.
 19. Brummer, T., Schramek, D., Hayes, V.M., Bennett, H.L., Caldon, C.E., Musgrove, E.A., and Daly, R.J., *Increased proliferation and altered growth factor dependence of human mammary epithelial cells overexpressing the Gab2 docking protein.* J Biol Chem, 2006. **281**(1): p. 626-37.
 20. Ciarloni, L., Mallepell, S., and Briskin, C., *Amphiregulin is an essential mediator of estrogen receptor alpha function in mammary gland development.* Proc Natl Acad Sci U S A, 2007. **104**(13): p. 5455-60.
 21. Mallepell, S., Krust, A., Chambon, P., and Briskin, C., *Paracrine signaling through the epithelial estrogen receptor alpha is required for proliferation and morphogenesis in the mammary gland.* Proc Natl Acad Sci U S A, 2006. **103**(7): p. 2196-201.
 22. Luetke, N.C., Qiu, T.H., Fenton, S.E., Troyer, K.L., Riedel, R.F., Chang, A., and Lee, D.C., *Targeted inactivation of the EGF and amphiregulin genes reveals distinct roles for EGF receptor ligands in mouse mammary gland development.* Development, 1999. **126**(12): p. 2739-50.
 23. Sternlicht, M.D., Sunnarborg, S.W., Kouros-Mehr, H., Yu, Y., Lee, D.C., and Werb, Z., *Mammary ductal morphogenesis requires paracrine activation of stromal EGFR via ADAM17-dependent shedding of epithelial amphiregulin.* Development, 2005. **132**(17): p. 3923-33.
 24. Ciarloni, L., Mallepell, S., and Briskin, C., *Amphiregulin is an essential mediator of estrogen receptor α function in mammary gland development.* Proceedings of the National Academy of Sciences of the United States of America, 2007. **104**(13): p. 5455-5460.
 25. Gjorevski, N. and Nelson, C.M., *Integrated morphodynamic signalling of the mammary gland.* Nat Rev Mol Cell Biol, 2011. **12**(9): p. 581-93.
 26. Edgerton, M.E., Chuang, Y.L., Macklin, P., Yang, W., Bearer, E.L., and Cristini, V., *A novel, patient-specific mathematical pathology approach for assessment of surgical volume: application to ductal carcinoma in situ of the breast.* Anal Cell Pathol (Amst), 2011. **34**(5): p. 247-63.

27. Xu, Y. and Gilbert, R., *Some inverse problems raised from a mathematical model of ductal carcinoma in situ*. Mathematical and Computer Modelling, 2009. **49**(3–4): p. 814-828.
28. Anderson, A.R., Chaplain, M.A., and Rejniak, K.A., *Single-Cell-Based Models in Biology and Medicine*. 1 ed. Mathematics and Biosciences in Interaction. 2007, Switzerland: Birkhäuser Basel. 349.
29. Walker, D.C. and Southgate, J., *The virtual cell--a candidate co-ordinator for 'middle-out' modelling of biological systems*. Brief Bioinform, 2009. **10**(4): p. 450-61.
30. Wang, Z., Butner, J.D., Kerketta, R., Cristini, V., and Deisboeck, T.S., *Simulating cancer growth with multiscale agent-based modeling*. Semin Cancer Biol, 2015. **30**: p. 70-8.
31. Tang, J., Enderling, H., Becker-Weimann, S., Pham, C., Polyzos, A., Chen, C.Y., and Costes, S.V., *Phenotypic transition maps of 3D breast acini obtained by imaging-guided agent-based modeling*. Integr Biol (Camb), 2011. **3**(4): p. 408-21.
32. Boghaert, E., Radisky, D.C., and Nelson, C.M., *Lattice-based model of ductal carcinoma in situ suggests rules for breast cancer progression to an invasive state*. PLoS Comput Biol, 2014. **10**(12): p. e1003997.
33. Lowengrub, J.S., Frieboes, H.B., Jin, F., Chuang, Y.L., Li, X., Macklin, P., Wise, S.M., and Cristini, V., *Nonlinear modelling of cancer: bridging the gap between cells and tumours*. Nonlinearity, 2010. **23**(1): p. R1-R9.
34. Deisboeck, T.S., Wang, Z., Macklin, P., and Cristini, V., *Multiscale cancer modeling*. Annu Rev Biomed Eng, 2011. **13**: p. 127-55.
35. Vander Heiden, M.G., Cantley, L.C., and Thompson, C.B., *Understanding the Warburg Effect: The Metabolic Requirements of Cell Proliferation*. Science (New York, N.Y.), 2009. **324**(5930): p. 1029-1033.
36. Shumate, S.D. and El-Shenawee, M., *Computational model of ductal carcinoma in situ: the effects of contact inhibition on pattern formation*. IEEE Trans Biomed Eng, 2009. **56**(5): p. 1341-7.
37. Gatenby, R.A., Smallbone, K., Maini, P.K., Rose, F., Averill, J., Nagle, R.B., Worrall, L., and Gillies, R.J., *Cellular adaptations to hypoxia and acidosis during somatic evolution of breast cancer*. Br J Cancer, 2007. **97**(5): p. 646-653.
38. Macklin, P., Edgerton, M.E., Thompson, A.M., and Cristini, V., *Patient-calibrated agent-based modelling of ductal carcinoma in situ (DCIS): from microscopic measurements to macroscopic predictions of clinical progression*. J Theor Biol, 2012. **301**: p. 122-40.
39. Hyun, A.Z. and Macklin, P., *Improved patient-specific calibration for agent-based cancer modeling*. J Theor Biol, 2013. **317**: p. 422-4.
40. Macdougall, J.D.B. and McCabe, M., *Diffusion Coefficient of Oxygen through Tissues*. Nature, 1967. **215**(5106): p. 1173-1174.
41. Sidell, B.D., *Intracellular oxygen diffusion: the roles of myoglobin and lipid at cold body temperature*. J Exp Biol, 1998. **201**(Pt 8): p. 1119-28.
42. Long, K., Kirby, R., and van Bloemen Waanders, B., *Unified Embedded Parallel Finite Element Computations via Software-Based Fréchet Differentiation*. SIAM Journal on Scientific Computing, 2010. **32**(6): p. 3323-3351.

43. Manni, A., *Endocrinology of Breast Cancer*. 1st ed. 1999, New York: Springer Science+Business Media.
44. Gusterson, B.A. and Stein, T., *Human breast development*. *Seminars in Cell & Developmental Biology*, 2012. **23**(5): p. 567-573.
45. Humphreys, R.C., Krajewska, M., Krnacik, S., Jaeger, R., Weiher, H., Krajewski, S., Reed, J.C., and Rosen, J.M., *Apoptosis in the terminal endbud of the murine mammary gland: a mechanism of ductal morphogenesis*. *Development*, 1996. **122**(12): p. 4013-22.
46. Hochreiter-Hufford, A. and Ravichandran, K.S., *Clearing the dead: apoptotic cell sensing, recognition, engulfment, and digestion*. *Cold Spring Harb Perspect Biol*, 2013. **5**(1): p. a008748.
47. Hinck, L. and Silberstein, G., *Key stages in mammary gland development: The mammary end bud as a motile organ*. *Breast Cancer Research*, 2005. **7**(6): p. 245 - 251.
48. Williams, J.M. and Daniel, C.W., *Mammary ductal elongation: differentiation of myoepithelium and basal lamina during branching morphogenesis*. *Dev Biol*, 1983. **97**(2): p. 274-90.
49. Chepko, G. and Smith, G.H., *Three division-competent, structurally-distinct cell populations contribute to murine mammary epithelial renewal*. *Tissue Cell*, 1997. **29**(2): p. 239-53.
50. Thorne, R.G., Hrabetova, S., and Nicholson, C., *Diffusion of epidermal growth factor in rat brain extracellular space measured by integrative optical imaging*. *J Neurophysiol*, 2004. **92**(6): p. 3471-81.
51. Shimizu, S., Eguchi, Y., Kamiike, W., Itoh, Y., Hasegawa, J., Yamabe, K., Otsuki, Y., Matsuda, H., and Tsujimoto, Y., *Induction of apoptosis as well as necrosis by hypoxia and predominant prevention of apoptosis by Bcl-2 and Bcl-XL*. *Cancer Res*, 1996. **56**(9): p. 2161-6.

CHAPTER 5

Development of a Three Dimensional, Lattice-free Multiscale Model of the Mammary Terminal End Bud

Joseph D. Butner, Vittorio Cristini, and Zhihui Wang, Member, IEEE

This work has been supported in part by the National Science Foundation (NSF) Grant DMS-1562068 (V.C., Z.W.), the National Institutes of Health (NIH) Grant 1U01CA196403 (V.C., Z.W.), and the University of Texas System STARS Award (V.C.).

J.D.B. is with the Department of Chemical Engineering and Center for Biomedical Engineering, University of New Mexico, Albuquerque, NM 87131, USA.

V. C. and Z.W. are with the Department of NanoMedicine and Biomedical Engineering, and Brown Foundation Institute of Molecular Medicine, University of Texas Medical School at Houston, Houston, TX 77054, USA, and also with Department of Imaging Physics, University of Texas MD Anderson Cancer Center, Houston, TX 77230, USA (corresponding author, phone: 713-486-5425; fax: 713-796-9697; e-mail: Zhihui.Wang@uth.tmc.edu).

I. Abstract

The terminal end bud (TEB) is a bulbous structure composed of highly proliferative cells that is responsible for mammary gland development during the pubertal stage. This is a highly organized process, involving cellular differentiation hierarchies regulated by endocrine and paracrine signaling. Here, we present development of a lattice-free, three dimensional multiscale agent based model of the TEB to study the effects of cellular phenotypic hierarchies, endocrine and paracrine signaling, and proliferation demographics on pubertal mammary gland development. Cells in the TEB experience complex physical interaction during the active growth involved in pubertal ductal elongation, which we represent mathematically based on the physical forces involved in cell-cell and cell-microenvironment interactions. We observe that maximum ductal elongation rates are achievable due to each progenitive phenotype cell only undergoing a couple proliferation cycles before losing the progenitive capability, and that molecular signaling is necessary to restrict ductal elongation to biologically relevant rates. Cellular proliferation and growth is sufficient to achieve these elongation rates in the absence of other cellular behaviors such as migration or conformational changes. This model serves as a valuable tool to gain insights into the cell population dynamics of mammary gland development, and can serve as a foundation to study the early stages of breast cancer development based on endocrine-mediated phenotypic population shifts.

II. Introduction

The mammary gland serves an essential role in mammalian biology. Consisting of only a rudimentary ductal tree structure at birth, the majority of glandular development is delayed until puberty, when a branched tree-like structure develops and invades the fat pad away from the nipple in response to upregulation of endocrine and paracrine signaling [1]. This growth and ductal elongation is driven by terminal end buds (TEBs), bulbous structures composed (in part) of a population of highly proliferative epithelial cells. The TEB is dual-layered in structure, with an outer layer of myoepithelial cells (regions 1-4, **Figure 5.1**) and an inner region of highly proliferative luminal epithelial cells (regions 5-8, **Figure 5.1**), corresponding to the dual layered structure in the mature mammary duct. Proximal in the TEB, highly proliferative luminal cells may be layered 5-6 cells thick (region 5, **Figure 5.1**). High cellular proliferation rates within the TEB allow for rapid ductal elongation, which has been observed as high as 0.5mm per day [2].

Pubertal ductal growth and branching is induced by upregulation of estrogen signaling and the associated response by estrogen receptor α positive (ER+) progenitor cells within the TEB [3]. Among other signaling molecules (see e.g., [4]), amphiregulin (AREG) production is upregulated in ER+ cells within the TEB [5], and serves as a secondary indirect downstream stromal signaling mechanism to the estrogen receptor negative (ER-) phenotype population within the TEB in pubertal cellular proliferation upregulation and ductal elongation [5, 6]. The progenitor population is maintained by progenitor self-renewal and a small number of multipotent ER- stem cells distributed randomly within the TEB [7], which may self-renew (divide symmetrically, giving rise to

two stem type daughters), or divide asymmetrically, giving rise to one stem and one progenitor daughter [6].

Within the TEB, a structured hierarchy of cellular development plays an important role in regulating ductal elongation rates. The proliferative population maintains rapid cellular proliferation necessary for ductal elongation, while the mature duct trailing the TEB is composed primarily of terminally differentiated, non-proliferative cells. This requires an organized transition from proliferative to differentiated phenotypes in a relatively short physical and temporal space. Here, we present a three dimensional, lattice-free multiscale agent based model of the TEB structure with cellular phenotype hierarchy and estrogen and AREG signaling to study the dynamics of cellular populations within the TEB. This serves as an expansion of our previous two-dimensional TEB modeling work [8].

III. Methods

i. Continuum Scale

Tissue scale parameters include oxygen, endocrine and paracrine molecular distributions throughout the TEB, which are assumed to diffuse freely through the tissue. These are represented mathematically by the reaction diffusion equation, a modification of Ficks's second law of diffusion:

$$\frac{\partial u}{\partial t} = D\nabla^2 u + R(u), \quad (1)$$

where u is time-dependent molecular concentration, with corresponding molecular diffusion constant (D) and reaction term (R). Diffusion constants for each molecule of interest are determined from the literature where available [9, 10], or estimated based on similar molecules. We obtain time dependent continuum solutions using finite element methods (FEM) with direct linear solvers in C++ through implementation of Sundance, a FEM package available as part of Trilinos (an open source numerical solver library developed by Sandia National Laboratory). Molecules that enter the TEB from the surrounding tissue (i.e. oxygen and estrogen) are introduced numerically as constant Dirichlet boundary conditions, while molecules which are sourced from within the computational domain (i.e. AREG) are allowed to diffuse freely within and out of the TEB through implementation of far-field homogeneous Neumann boundary conditions. Time-dependent FEM solutions are obtained for each time step on a 3D tetragonal mesh (a schematic of the computational domain is shown in **Figure 5.1**) and time-dependent numerical FEM solutions are incremented with the same time step as the discrete scale.

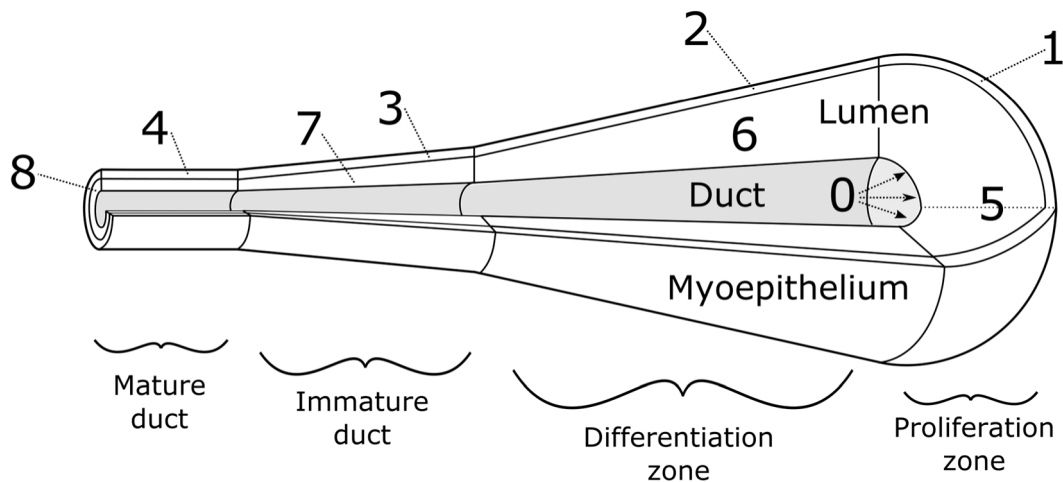


Figure 5.1: A schematic of the 3D computational domain of TEB. Regions 1-4 compose the myoepithelial layer, and 5-8 the luminal layer. Region 0 is the ductal formation zone. All Dirichlet boundary conditions are applied on the outermost layer of the myoepithelium.

ii. *Discrete Scale*

At the discrete cellular scale, every cell is represented by a unique agent, each with its own phenotype, signaling molecule sensitivity, and position, using a method known as agent based modeling (ABM) [11]. Agents may proliferate, move, uptake or produce signaling molecules, consume oxygen, grow, and undergo apoptosis. Apoptosis within the luminal layer is instrumental in formation of the duct cavity, and occurs stochastically in the model based on biologically observed rates of 7.9% distal to the duct formation region (region 0, **Figure 5.1**) and 14.5% proximally [12]. Agents may also experience hypoxia and necrosis, although due to the small scale of the TEB relative to the Krogh length for oxygen this behavior is not observed in the normal TEB. When an agent with progenitor phenotype undergoes a mitosis event, the cytoplasmic volume is divided evenly between both daughters. Subsequent to a mitosis event, agents enter G1 phase for 7.5 hours of growth (taken relative to the percentage of time spent in G1 in a 24 hour cell cycle time), where growth is taken to be a function of cellular volume [13]. Thus cells experience an exponential growth pattern until they reach full size, at which point they enter into S phase. The events of S and G2 phases are not explicitly modeled as they are not the focus of this study. Cells may repeat the cell division cycle until they hit a threshold for maximum number of divisions (previously determined to be 2-3 cycles), at which point they differentiate into a non-proliferative phenotype. Proliferation events may only occur if molecular signaling thresholds (as described in **Figure 5.2**) are satisfied.

In our lattice-free 3D model, physical interactions between agents are determined computationally based on an approximation of the real-world physics of cellular

interactions. Although agents are free to move without the restrictions of a lattice structure, they are subjected to an imposed TEB geometry based on data from [14]. Cells adhere to other cells with a preferential adhesion towards same or alike phenotypes [15], and to the external basement membrane (for myoepithelial cells). While we explicitly model the basement membrane ECM that defines the outer boundary of the TEB, the structural effects of ECM between cells internally in the TEB is implicitly approximated mathematically as a summation of adhesion forces between agents and forces that resist cells sliding or rolling against each other. Proliferation events and cellular growth displace their neighbors (without a preference for a particular direction (i.e. towards or away from the TEB tip) based exclusively on the physical interaction between cells. In this way, ductal elongation is driven through cellular proliferation and growth. Cells interact inelastically, and are allowed to deform due to pressure from surrounding cells. Although we do not explicitly model this conformational change in each individual agent, we implement this mathematically through a coefficient of restitution, where some energy of interaction is lost as it is converted into deformational energy in the agent. Cells also experience motion dampening due to the aqueous environment, and will lose kinetic energy over time in the absence of external forces or any contact between other cells or ECM.

iii. Hybrid Modeling Methods

In the model, discrete and continuum methods and scales are explicitly linked to form a multiscale model [16]. Cells interact with the continuum solutions of molecular concentration bidirectionally, and dependent on phenotypic characteristics. At each time step, agents query their environment to determine local molecular concentrations, which

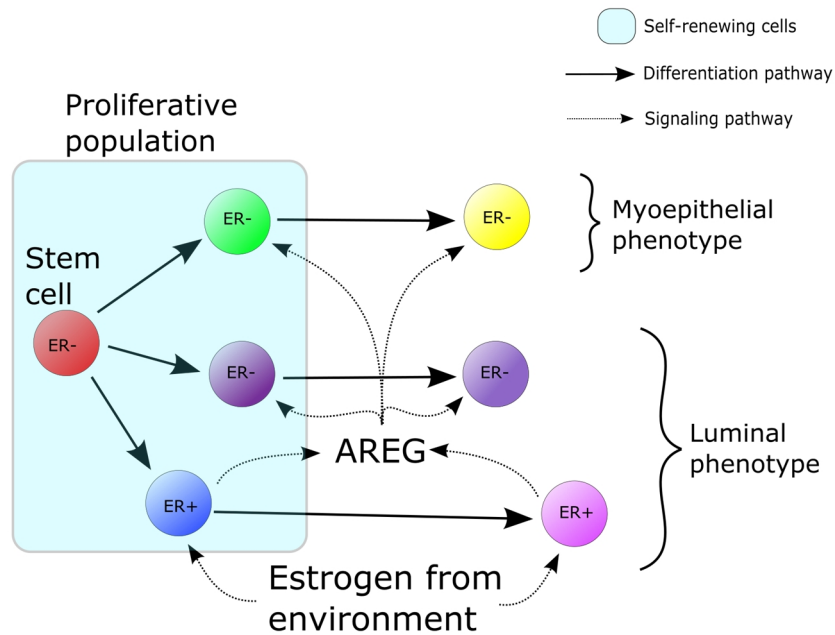


Figure 5.2: Cellular phenotypic types, differentiation pathways and signaling. Cells within the proliferative population possess the ability to self-renew, where they divide symmetrically into two phenotypically similar progenitor cells, or to divide asymmetrically, where one daughter is proliferative and the other is differentiated. Upon hitting a built-in proliferation threshold, progenitors divide symmetrically into two differentiated daughters. Proliferation events are dependent on a signaling molecule threshold based on phenotype, which must be satisfied before mitosis can occur.

are linearly interpolated to the agent's location from the solutions at the nearest nodes in the FEM solution. Agents consume oxygen, and may either uptake or produce signaling molecules base on agent phenotype (see **Figure 5.2**). These molecular concentration changes are added to the continuum solutions through imposition of Dirac delta functions on the nearest node, as identified through Voronoi tessellation (a method where the computational domain is divided into regions which encompasses the volume closest to each individual node). Agents with progenitive phenotype may only undergo a mitosis event if molecular concentration thresholds are satisfied, and only after completing a full cell cycle from their last proliferation event, which we take to be 16 hours based on [14].

IV. Results and Discussion

Based on previous work [8], we determined that progenitor cells in the TEB likely undergo 2-3 mitosis cycles before differentiation (which we refer to as 2x-3x in this document). In [8], the ductal elongation rate could reach roughly 625-895 $\mu\text{m}/\text{day}$ in the absence of growth restriction due to molecular signaling threshold limitation (i.e., by removing the effects of signaling threshold on ductal elongation). To perform validation of the 3D model, we repeated this experiment and compared maximum theoretical growth rates to those observed biologically and in the 2D model. Note that currently we assume axial symmetry, and only simulate half of the TEB (as shown in **Figure 5.3**). Due to geometry differences between the 2D and 3D cases, seeding the 3D TEB (under the same probabilities as the 2D model) results in $\sim 12\%$ higher progenitor density in the total cellular population at the start of the simulation. Our preliminary results show that the maximum possible growth rates have increased roughly 60% over rates observed in the 2D modeling case (61.6% and 60.1% in the 2x and 3x cases, respectively), consistent with our expectations (**Figure 5.4a**). This is expected because ductal elongation in the 3D case only requires 9.5 as many cells per unit of elongation as the 2D model (relative to the $\sim 14\text{x}$ more progenitors in the 3D TEB), so we expect to see higher maximum possible growth rates in the 3D case. The maximum possible ductal elongation rates we observe are higher than those observed in nature, suggesting that molecular signaling mechanisms play a crucial role in regulation of pubertal mammary gland cellular proliferation and the resulting ductal elongation.

Interestingly, we observed that ductal elongating rates are slow in the early stage of all simulations (**Figure 5.4b**, time steps 1-16). Although proliferation is occurring at a

comparable rate to later time steps, total cellular volume increases slowly at first because daughter growth is a function of cytoplasmic volume. Thus new daughters grow slowly

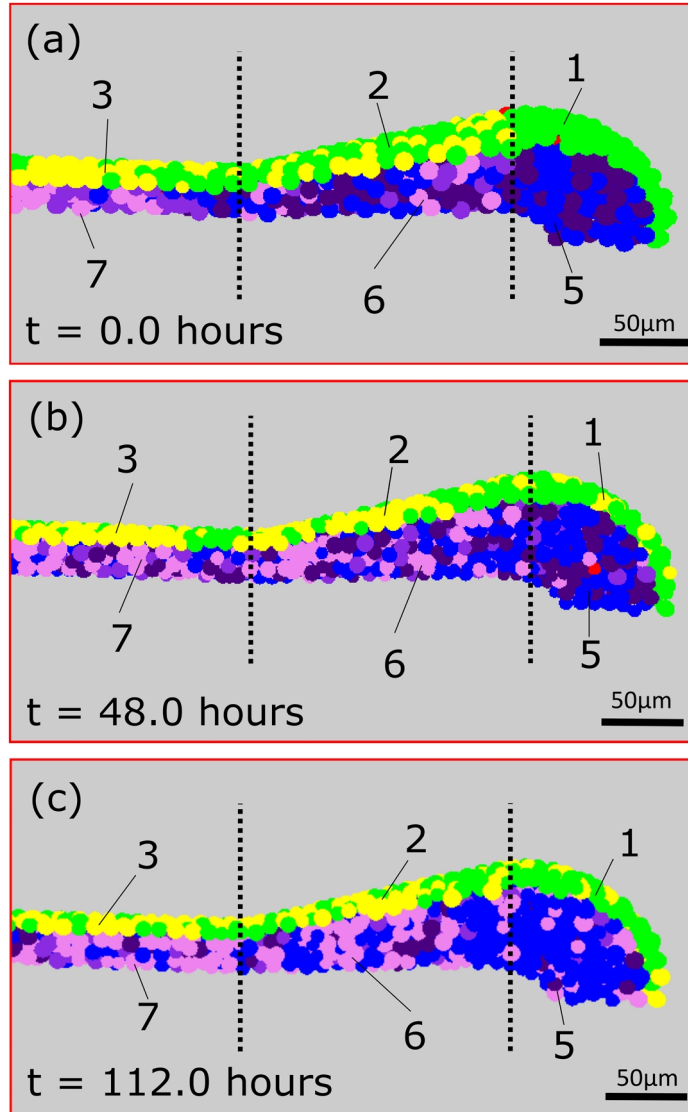


Figure 5.3: Sample simulation output. (a) Interior view of the TEB at the start of a simulation; regions 1 & 5 are seeded with only proliferative phenotype, with increasing differentiated population away from the TEB tip (left). (b) Simulation after 3 cell cycles, note that there are now differentiated agents in the proliferation zone (regions 1&5) due to agents reaching their proliferation cycle threshold. (c) Simulation after 7 cell cycles, shows further mixing of phenotypes in the proliferation zone as self-renewal events are balanced by differentiation events. Simulated time is shown in the bottom left, and all images shown are for the 3x before differentiation case. Color scheme as shown in **Figure 5.1**.

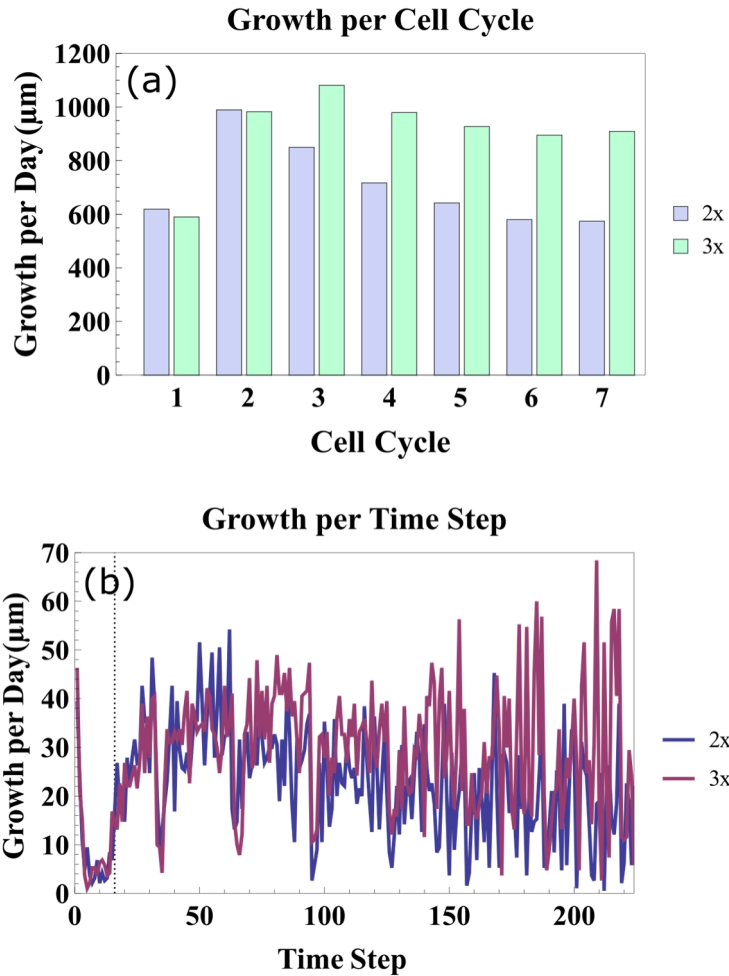


Figure 5.4: (a) Ductal elongation per cell cycle. After initial seeding, growth rates increase until differentiation events start to occur due to progenitors reaching their proliferation threshold (for either 2x or 3x cycles before differentiation). Growth is seen to be higher in the 3x case, as more self-renewal cycles maintains a larger total progenitor population. (b) Ductal elongation per time step. Note decreased elongation rates for $t < 16$ (indicated by dashed line); reduced cellular volume allows for tighter cell packing in new daughters. Subsequent to this initial stage, elongation rates are variable but consistent, and can be seen to be higher for the 3x case. One time step = 30 minutes.

immediately after mitosis, contributing less to ductal elongation than when they are closer to being fully grown. When combined with the fact that the smaller daughters can be packed together more tightly, the early proliferation events do not contribute to ductal elongation as much as cellular growth does later in simulation time. Thus ductal elongation is observed to be primarily a result of cellular growth subsequent to proliferation events.

We have made the assumption that proliferation events are more likely towards the TEB tip (based on biologically observed higher concentration of progenitors in this region, in what we call the proliferation zone (**Figure 5.1**)), and are relatively unlikely in the mature duct, as progenitor populations are found to be small in the nulliparous mature duct [17]. Combined with differentiation events due to hitting the proliferation threshold, this results in reliable maintenance of a progenitor population in the proliferation zone, and progressively reduced progenitive population in the differentiation, immature, and mature zones, respectively. Differentiation events due to hitting the proliferation threshold still occur in the proliferation region, resulting in a small population of differentiated agents in this region, which is inversely proportional to the number of proliferation cycles before differentiation. Thus the assumption of proliferation and differentiation zones is supported by our model, and model validation is supported both by observed growth rates and phenotypic distribution observed in living systems.

In our next work, we will further investigate how changes in molecular signaling impact ductal elongation. We will also incorporate this model with the phenotypic hierarchy and estrogen/AREG signaling pathways into a breast cancer (ductal carcinoma in situ, DCIS) model to study ER+ vs. ER- DCIS with the aim of gaining new insights into how hormonal concentrations influence the development of the phenotypically distinct (and with very different prognoses) types of DCIS.

V. Acknowledgements

We thank M Lewis and J Rosen (Baylor College of Medicine), J Lowengrub (UC Irvine), and Y-L Chuang (California State University, Northridge). We also acknowledge support from the Methodist Hospital Research Institute (V.C.).

© 2016 IEEE. Reprinted, with permission, from Butner, J.D., V. Cristini, and W. Zhihui, *Development of a three dimensional, lattice-free multiscale model of the mammary terminal end bud*. Conf Proc IEEE Eng Med Biol Soc, 2016. **2016**: p. 6134-6137.

VI. Works Cited, Chapter 5

1. Hennighausen, L. and Robinson, G.W., *Signaling pathways in mammary gland development*. Dev Cell, 2001. **1**(4): p. 467-75.
2. Hinck, L. and Silberstein, G.B., *Key stages in mammary gland development: The mammary end bud as a motile organ*. Breast Cancer Research, 2005. **7**(6): p. 245-251.
3. Sternlicht, M.D., *Key stages in mammary gland development: The cues that regulate ductal branching morphogenesis*. Breast Cancer Research, 2006. **8**(1): p. 201-201.
4. Gjorevski, N. and Nelson, C.M., *Integrated morphodynamic signalling of the mammary gland*. Nat Rev Mol Cell Biol, 2011. **12**(9): p. 581-93.
5. Ciarloni, L., Mallepell, S., and Briskin, C., *Amphiregulin is an essential mediator of estrogen receptor alpha function in mammary gland development*. Proc Natl Acad Sci U S A, 2007. **104**(13): p. 5455-60.
6. Dontu, G., El-Ashry, D., and Wicha, M.S., *Breast cancer, stem/progenitor cells and the estrogen receptor*. Trends Endocrinol Metab, 2004. **15**(5): p. 193-7.
7. Asselin-Labat, M.L., Shackleton, M., Stingl, J., Vaillant, F., Forrest, N.C., Eaves, C.J., Visvader, J.E., and Lindeman, G.J., *Steroid hormone receptor status of mouse mammary stem cells*. J Natl Cancer Inst, 2006. **98**(14): p. 1011-4.
8. Butner, J.D., Cristini, V., and Zhihui, W., *A modeling approach to study the normal mammary gland growth process*. Conf Proc IEEE Eng Med Biol Soc, 2015. **2015**: p. 1444-7.
9. MACDOUGALL, J.D.B. and MCCABE, M., *Diffusion Coefficient of Oxygen through Tissues*. Nature, 1967. **215**: p. 1173 - 1174.
10. Sidell, B.D., *Intracellular oxygen diffusion: the roles of myoglobin and lipid at cold body temperature*. J Exp Biol, 1998. **201**(Pt 8): p. 1119-28.
11. Wang, Z., Butner, J.D., Kerketta, R., Cristini, V., and Deisboeck, T.S., *Simulating cancer growth with multiscale agent-based modeling*. Semin Cancer Biol, 2015. **30**: p. 70-8.
12. Humphreys, R.C., Krajewska, M., Krnacik, S., Jaeger, R., Weiher, H., Krajewski, S., Reed, J.C., and Rosen, J.M., *Apoptosis in the terminal endbud of the murine mammary gland: a mechanism of ductal morphogenesis*. Development, 1996. **122**(12): p. 4013-22.
13. Bryan, A.K., Goranov, A., Amon, A., and Manalis, S.R., *Measurement of mass, density, and volume during the cell cycle of yeast*. Proc Natl Acad Sci U S A, 2010. **107**(3): p. 999-1004.
14. Paine, I., Chauviere, A., Landua, J., Sreekumar, A., Cristini, V., Rosen, J., and Lewis, M.T., *A Geometrically-Constrained Mathematical Model of Mammary Gland Ductal Elongation Reveals Novel Cellular Dynamics within the Terminal End Bud*. PLoS Comput Biol, 2016. **12**(4): p. e1004839.
15. Muschler, J. and Streuli, C.H., *Cell-matrix interactions in mammary gland development and breast cancer*. Cold Spring Harb Perspect Biol, 2010. **2**(10): p. a003202.

16. Deisboeck, T.S., Wang, Z., Macklin, P., and Cristini, V., *Multiscale Cancer Modeling*. Annual review of biomedical engineering, 2011. **13**: p. 10.1146/annurev-bioeng-071910-124729.
17. Chepko, G. and Smith, G.H., *Three division-competent, structurally-distinct cell populations contribute to murine mammary epithelial renewal*. Tissue Cell, 1997. **29**(2): p. 239-53.

CHAPTER 6

*Development of a Three Dimensional, Multiscale Agent-Based Model of Ductal Carcinoma in Situ**

Joseph D. Butner, Vittorio Cristini, and Zhihui Wang, Member, IEEE

*This work has been supported in part by the National Science Foundation (NSF) Grant DMS-1562068 (V.C., Z.W.), the National Institutes of Health (NIH) Grant 1U01CA196403 (V.C., Z.W.), the Rochelle and Max Levit Chair in the Neurosciences (V.C.), and the University of Texas System STARS Award (V.C.).

J.D.B. is with the Department of Chemical Engineering and Center for Biomedical Engineering, University of New Mexico, Albuquerque, NM 87131, USA.

V. C. and Z.W. are with the Center for Precision Biomedicine, Brown Foundation Institute of Molecular Medicine, University of Texas McGovern Medical School at Houston, Houston, TX 77054, USA, and also with Department of Imaging Physics, University of Texas MD Anderson Cancer Center, Houston, TX 77230, USA (corresponding author, phone: 713-486-5425; fax: 713-796-9697; e-mail: Zhihui.Wang@uth.tmc.edu).

I. Abstract

Ductal carcinoma in situ (DCIS) is the most commonly diagnosed form of non-invasive breast cancer, constituting 20% of all new breast cancer cases in the United States. Although non-invasive, DCIS is usually treated surgically through resection. Interestingly, long-term survival studies have shown that patient survival rates are not significantly impacted by the type or resection, indicating that increased breast conservation through minimized surgical resection may indeed be possible. This requires a greater understanding of disease development, so that clinicians may more accurately determine surgical margins which minimize patient impact while maintaining survival rates. To this end, we have developed a three-dimensional, lattice-free multiscale agent based model of DCIS designed to help quantify ductal invasion rates, in order to allow clinicians to better estimate disease age and extent of invasion, and to predict surgical margins based on parameters obtainable from non-invasive testing (i.e., mammography). Here, we present the model development to date, and discuss some preliminary results.

II. Introduction

DCIS accounts for roughly 20% of newly detected breast cancers [1], with upwards of 60,000 new cases annually. DCIS is characterized by loss of luminal epithelial cell homogeneity, resulting in invasive epithelial cell growth into (but constrained within) the mammary ductal cavity. Although not malignant in itself (in fact, all DCIS is considered stage 0 breast cancer), DCIS is associated with invasive breast cancer and a higher risk of

recurring breast cancer, thus usually necessitating treatment through lumpectomy followed by radiation and sometimes hormone therapy, or in other cases even full mastectomy.

Breast cancers are categorized according to estrogen receptor (ER), progesterone receptor (PR), and HER2 receptor status; as many as 75% of DCIS cases are reported to be ER α positive (ER+) [2], with lower instances of PR+ and HER2+ DCIS. Furthermore, transition to an invasive phenotype has been shown to be more frequently associated with ER+ DCIS [3], and roughly 70% of all breast tumors are ER+ [4]. DCIS is categorized histologically through cell distribution (archeology) and cytological structural features (grade, i.e. DCIS cell proliferation rate, where higher grades are associated with higher cell proliferation rates and increased invasive behavior).

Successful treatment of DCIS by surgical resection while achieving minimal patient impact requires accurate assessment of surgical margins. DCIS invasion requires epithelial cell motility, which may be initiated by epithelial to mesenchymal transition (EMT) [5], and is shown to be associated with loss of ER α functionality [6]. Estrogen signaling to ER α results in increased mammary epithelial proliferation through downstream paracrine epithelial to stromal signaling in the ER- cell population [7], while reduced estrogen availability has been shown to restrict cellular proliferation and mammary gland development while increasing ER density in the ER+ mammary epithelial population within bovine heifer pubertal gland development [8]. Estrogen signaling to the ER+ population results in upregulation of amphiregulin (AREG) production within this population, which signals to EGF receptors in the stroma, and induces downstream stromal to endothelial upregulation of proliferation within the ER- population through fibroblast growth factor (i.e. FGF-2,7) signaling (among others, which are not examined in this

model) [9]. Contrary to the normal pubertal gland development, estrogen signaling to the ER+ population has been shown to induce proliferation within ER+ breast cancer cells [7].

We have been developing integrated mathematical models to understand cancer biology and treatment [10, 11]. Here, we present a three-dimensional, lattice-free multiscale agent based model (ABM) [12] to study the effect of estrogen endocrine and downstream AREG through FGFs paracrine signaling in DCIS ductal invasion, invasion rates, and development of DCIS architectures. The duct is modeled as two cylindrical cell layers, an outer myoepithelial (basal) layer, and an inner luminal layer, which together represent the mature mammary duct. Because our focus is the effects of cell dynamics and signaling within the mammary duct, we have restricted our modeling efforts to only model a section of a single duct branch, approximated with a cylindrical geometry. Cells in the mature duct layers (myoepithelial and luminal) are confined to their respective layers, but may be displaced within the region by growth/movement events in the surrounding cells.

III. Methods

i. Discrete Scale

Within the discrete portion of the model, all cells are represented as unique discrete agents. Each agent has its own physical location, phenotype, and contribution to both discrete and continuum scales (all cells consume oxygen, and signaling molecules are consumed or produced based on agent phenotype as shown in **Figure 6.1**). All agents in the model are free to move based on environmental events, such as the physics of cell growth, movement, and proliferation, but constrained by the mature duct geometry and resistance to displacement in neighboring agents. Agent movement and displacement is

determined mathematically through solving the physics of cell-cell interactions, and includes force balance of cell-cell physical interaction, cell-cell adhesion, cell deformation through inelastic interaction (not explicitly modeled, but implemented mathematically as a coefficient of restitution), and viscous motion dampening from the fluid environment.

Cells in the model must satisfy a set of biologically-based conditions before they proliferate, including verification of adequate nearby room in which to divide, the satisfaction of local cell proliferation upregulating signaling molecule concentrations, adequate local oxygen concentration (i.e. the cell is not hypoxic, as is common in tumors), and completion of all phases of the cell's previous proliferation cycle. Upon a mitosis proliferation event, the mother's cytoplasmic volume is divided evenly between both daughters, with the cleavage furrow occurring at a random orientation, but within the geometric restrictions of the model (e.g. a mitosis event in a cell monolayer must occur in an orientation that maintains the monolayer). Daughters experience cytoplasmic growth exponentially as a function of cytoplasmic volume [13] during the G1 phase for 7.5 hours, while the subcellular events in the S-G2 phases are not explicitly represented. New daughters have a phenotype as determined by **Figure 6.1** with a stochastic chance the mitosis event may result in symmetric division (two daughters the same phenotype as the mother) or asymmetric division (one daughter is the same phenotype as the mother, while the other takes a more differentiated phenotype). We note that we assume all mothers of a cancer phenotype retain their progenitor ability as a result of the cancer mutation, and thus one daughter in a mitosis event will always retain the mother's progenitor (or CSC) phenotype. Furthermore, cancerous phenotypes are only minimally limited in proliferation potential, and may undergo numerous mitosis cycles, although agents are limited by

molecular signaling and cell cycle time restrictions, and may proliferate only when molecular thresholds are satisfied and the last mitosis cycle (16 hours) is complete.

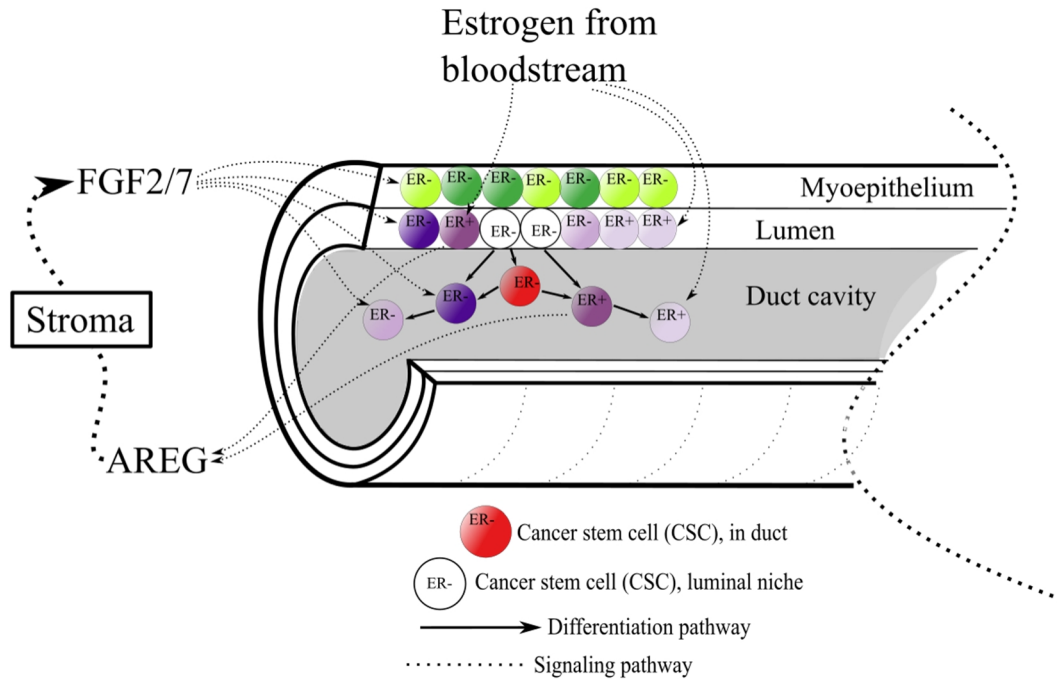


Figure 6.1: Computational domain; a section of mature mammary duct with myoepithelial, luminal, and luminal duct cavity regions. Upon an EMT cancer initiation event, a CSC niche is seeded in the luminal layer (shown in white) Cell proliferation hierarchy and signaling pathways are modeled as shown. CSCs may proliferate into the luminal niche, contributing to the DCIS population, as both stem and progenitor phenotypes. Progenitors may give rise to progenitive or differentiated daughters. Estrogen, AREG, and FGF signaling pathways are as shown.

ii. *Continuum Scale*

Within the model, several key molecular profiles are represented numerically: oxygen, estrogen, AREG, and FGF molecular profiles are all described as continuums, and are allowed to move freely through the computational domain according to Fick's law of diffusion. Continuum profiles are solved for each time step numerically on a three-dimensional tetragonal mesh using the finite element method (FEM). Oxygen and estrogen

are taken to be delivered from the blood supply surrounding the duct (assumed to be a large reservoir relative to concentrations that enter the duct), and are thus implemented numerically as constant Dirichlet boundary conditions on the outer boundary of the duct myoepithelial region. AREG is produced internally in the duct by ER+ cells, and is free to diffuse throughout the duct and out into the surrounding stroma numerically through the implementation of far field homogenous Neumann boundary conditions. Epithelial to stromal signaling downstream from AREG (through the FGF7/2-FGFR2b/c pathway [9]) is introduced onto the outer duct boundary as a Dirichlet boundary condition through a time-dependent function of the AREG concentration exiting the duct boundary. We assume a 1:1 relationships between AREG entering the stroma and FGF entering the gland from the stroma; to this end, we implement the boundary condition for FGF entering the gland by reading the values of the AREG solution at each boundary node for each time step and using the same values as Dirichlet values at each boundary node in the corresponding FGF solution time step. Continuum solutions are advanced using finer time steps than the discrete ABM component for increased solution precision and stability.

iii. Hybrid Modeling Method

In the model, explicit linking between discrete and continuum modeling components results in a hybrid, multiscale model [14]. At the beginning of each ABM time step, agents determine the local concentration of all molecules included in the model from the continuum solutions, as a linear tetrahedral interpolation from the values at the nodes nearest the agent to the agent center of mass. Agents may modify the continuum molecular profile solutions bidirectionally through either uptake or secretion of the

respective molecules, implemented numerically as Dirac delta functions imposed on the nearest FEM node to the agent's center of mass (as determined through Voronoi tessellation). Estrogen signaling to ER⁺ epithelial cells upregulates AREG production in these agents, which diffuses out of the duct and signals to the surrounding stroma, upregulating stromal FGF secretion back into the duct. Due to lack of literature supported concentration quantification for estrogen, AREG, and FGF's within the mammary gland, we implement these values as normalized quantities. All simulations and results presented were run on the Texas Advanced Computing Center (TACC) Lonestar 5 machine at the University of Texas at Austin [15].

In the model, DCIS is initiated as an EMT event in one or more adjacent luminal epithelial stem cells within the inner luminal layer of the mature duct, resulting in a cancer stem cell (CSC) niche. We implement the EMT phenotypic change through loss of quiescence and a permanent commitment to a proliferative, cancer stem cell phenotype. Subsequent to EMT transition, CSCs may place cancer phenotype daughters (according to the cell hierarch shown in **Figure 6.1**) into the lumen, initiating DCIS. Subsequent to DCIS initiation, proliferators in the DCIS population will also place their daughters into the luminal cavity, which are assigned a phenotype stochastically according to the differentiation pathway shown in **Figure 6.1**. Invasion of the luminal cavity by DCIS is driven by proliferation events and subsequent cell growth. Agent proliferation and the resulting agent distribution is restricted to the duct cavity, but otherwise unregulated, in order to simulate the unregulated growth observed in cancer; thus agents are allowed to invade the duct cavity in a purely stochastic fashion. Agents within the outer myoepithelial layer do not contribute to DCIS, but do contribute to bidirectional continuum profile

modifications, and thus are included in the model for sake of completeness and to increase accuracy and model predictive power.

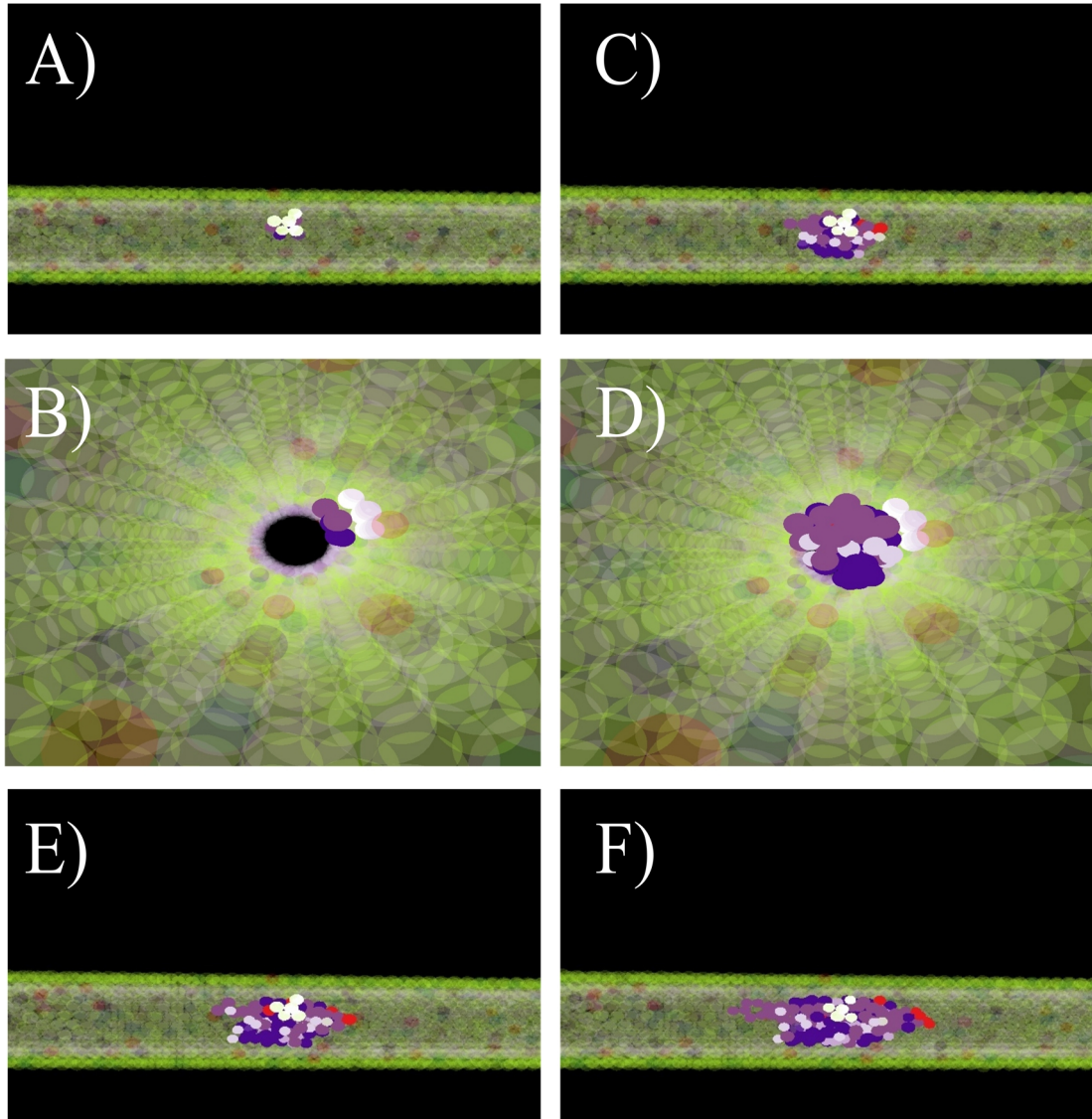


Figure 6.2: A section of simulated mature mammary gland duct: diameter, $50\mu\text{m}$; length, $500\mu\text{m}$. A) DCIS is initialized in the luminal region in the form of a cancer stem cell niche (5 CSCs), shown in white. B) Zoomed in view of panel A, shown from the inside of the duct. CSC niches can be seen in the luminal wall in white, with the initial stages of DCIS (after 1 simulated cell cycle of invasive growth) invasion seen invading the ductal cavity (purple). C,D) DCIS growth after 4 cell cycles; cell growth has expanded across the duct diameter and is starting to invade the duct axially. E,F) DCIS growth after 6 and 8.5 cell cycles of DCIS growth, respectively; DCIS invades the duct axially as cancer cell population increases.

IV. Results and Discussion

Initial model validation was performed through two experiments: 1) a study varying the number of CSCs initially seeded in the CSC niche, and 2) perturbation of the sensitivity of the ER+ DCIS population to proliferation upregulation through estrogen signaling. An example of CSC seeding and DCIS invasion in the model is shown in **Figure 6.2**. In the case of estrogen threshold sensitivity, cells with low signaling thresholds are more sensitive to estrogen signaling, and correspond to an ER+ DCIS phenotype, while cells with high

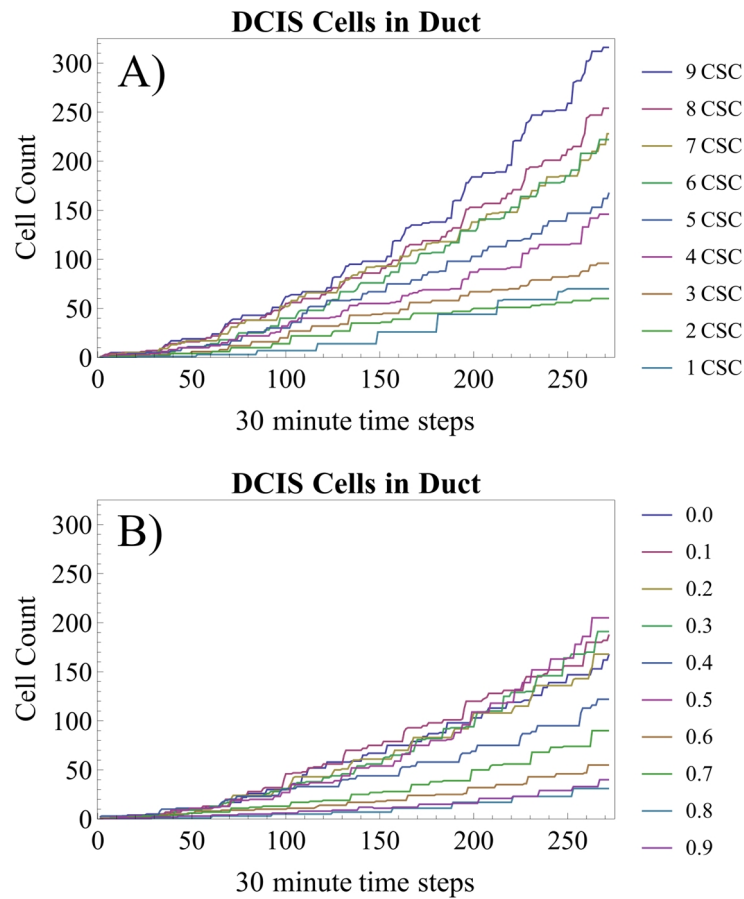


Figure 6.3: Total DCIS cell count in the duct cavity over time. A) CSC niche size variation, 1-9 CSCs seeded in the luminal CSC niche at time $t=0$. Greater numbers of CSCs in the niche result in more DCIS daughters per cell cycle and increased total cells in the niche. B) Cell proliferation with the ER+ phenotype limited by estrogen threshold; higher thresholds result in decreased proliferation, while low threshold so not show noticeable proliferation decrease. In the estrogen threshold limited case, the DCIS population is still increased by the ER- population and limited ER+ proliferation. One time step = 30 minutes.

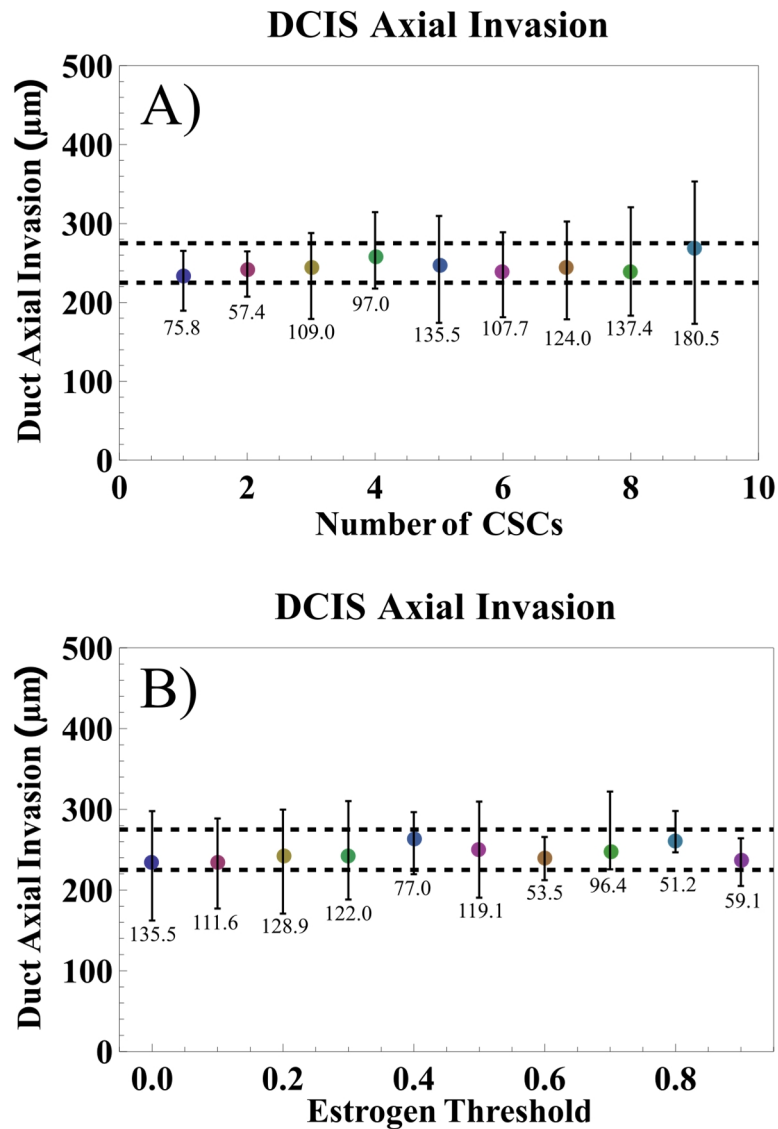


Figure 6.4: DCIS axial invasion extent. The CSC niche is constrained to roughly the center of the duct (but allowed to initiate stochastically within this region), indicated by the dotted lines. The location of the first DCIS cell to invade the duct cavity is shown by colored dots, with bars showing the total ductal invasion length \pm this location (y axis, as determined by the center of mass of the DCIS agent furthest from the initial DCIS invasion) after 272 time steps of simulated DCIS progression (8.5 simulated days). A) Duct invasion as a function of CSC niche size; B) duct invasion as limited by estrogen threshold. Numbers below bars indicate exact extent of DCIS invasion (μm).

thresholds are less sensitive to estrogen, and correspond to a more ER- phenotype. DCIS invasion was quantified as per the number of DCIS cells in the duct and length of DCIS axial invasion (Figures 6.3, 6.4).

In the CSC seed perturbation study, increased numbers of CSCs were associated with higher numbers of DCIS cells in the duct, increased ductal invasion, and increased DCIS cell density in the duct (density data not shown). Initial proliferation events were found to adhere to the mature duct luminal layer (**Figure 6.2b**) due to cell-cell adhesive forces, resulting in initial ductal invasion proceeding axially along the luminal wall, but with low cell density when considered across the entire duct radius. Subsequent proliferation events resulted in DCIS cells expanding across the duct radius in addition to growth in the axial direction, filling the entire duct radius and increasing the axial invasion rate due to the increased DCIS progenitor population. Increased cell proliferation resulted in increased DCIS cell density in the duct, which we define as the volume of cylindrical duct cavity which fully encases the entire DCIS population (e.g. bars in **Figure 6.4**), defined by the total volume of the cells in that cylindrical volume (calculated exactly for each time step from the known radius of each agent). We note that, due to the spherical representation of agents and the empty spaces between agents, DCIS cell density may never reach 100% of the duct volume; as limited by sphere packing rules.

Estrogen threshold sensitivity was shown to have a notable effect on cell populations, as ER⁺ cells restricted by a high estrogen threshold were unable to proliferate, significantly reducing the total DCIS cell population. However, because we did not place any signaling threshold restrictions on the ER⁻ population (that is, the cells that are proliferation dependent on downstream FGF signaling), this ER⁻ population was able to proliferate freely, and thus cell proliferation was not seen to halt completely even when the ER⁺ population was severely limited in proliferation ability. We also observe that the DCIS population towards the duct center was most affected by this limitation; because estrogen

enters the duct from the outer boundary, the estrogen concentration was lowest along the duct axis, thus allowing some ER+ proliferation in the proliferation-limited high threshold case along the outer edge of the duct cavity (data not shown).

In both experiments, the same effects of reduced cell proliferation due to a high estrogen signaling threshold or due to a reduced CSC population were manifested similarly: reduced proliferation lead to lower axial invasion rates and reduced DCIS cell density. In our next work, we will study the impact of the AREG-FGF signaling pathways on DCIS progression, as well as conduct studies in larger diameter ducts to study the effects of oxygen-restriction induced hypoxia, necrosis, and cell lysis and calcification on ductal invasive rates, surgical margins between calcified regions (as seen in mammography) and the viable edge of the DCIS, as well studies on how cell-cell physics and calcification influence the development of the four DCIS architectures.

V. Acknowledgements

We thank M Lewis and J Rosen (Baylor College of Medicine), J Lowengrub (UC Irvine), and Y-L Chuang (California State U, Northridge). We acknowledge support from the Methodist Hospital Research Institute (V.C.).

© 2017 IEEE. Reprinted, with permission, from Butner, J.D., V. Cristini, and W. Zhihui, In press, to be presented at EMBC 2017, July 11-15 2017.

VI. Works Cited, Chapter 6

1. Allegra, C.J., Aberle, D.R., Ganschow, P., Hahn, S.M., Lee, C.N., Millon-Underwood, S., Pike, M.C., Reed, S.D., Saftlas, A.F., Scarvalone, S.A., Schwartz, A.M., Slomski, C., Yothers, G., and Zon, R., *NIH state-of-the-science conference statement: diagnosis and management of ductal carcinoma in situ (DCIS)*. NIH Consens State Sci Statements, 2009. **26**(2): p. 1-27.
2. Dobrescu, A., Chang, M., Kirtani, V., Turi, G.K., Hennawy, R., and Hindenburg, A.A., *Study of Estrogen Receptor and Progesterone Receptor Expression in Breast Ductal Carcinoma In Situ by Immunohistochemical Staining in ER/PgR-Negative Invasive Breast Cancer*. ISRN Oncology, 2011. **2011**: p. 673790.
3. Malafa, M., Chaudhuri, B., Thomford, N.R., and Chaudhuri, P.K., *Estrogen receptors in ductal carcinoma in situ of breast*. Am Surg, 1990. **56**(7): p. 436-9.
4. Moerkens, M., Zhang, Y., Wester, L., van de Water, B., and Meerman, J.H.N., *Epidermal growth factor receptor signalling in human breast cancer cells operates parallel to estrogen receptor α signalling and results in tamoxifen insensitive proliferation*. BMC Cancer, 2014. **14**: p. 283-283.
5. Gjorevski, N. and Nelson, C.M., *Integrated morphodynamic signalling of the mammary gland*. Nat Rev Mol Cell Biol, 2011. **12**(9): p. 581-93.
6. Bouris, P., Skandalis, S.S., Piperigkou, Z., Afratis, N., Karamanou, K., Aletras, A.J., Moustakas, A., Theocharis, A.D., and Karamanos, N.K., *Estrogen receptor alpha mediates epithelial to mesenchymal transition, expression of specific matrix effectors and functional properties of breast cancer cells*. Matrix Biol, 2015. **43**: p. 42-60.
7. Li, M., Fu, X., Ma, G., Sun, X., Dong, X., Nagy, T., Xing, C., Li, J., and Dong, J.T., *Athf1 regulates pubertal mammary gland development likely by inhibiting the pro-proliferative function of estrogen-ER signaling*. PLoS One, 2012. **7**(12): p. e51283.
8. Berry, S.D., Jobst, P.M., Ellis, S.E., Howard, R.D., Capuco, A.V., and Akers, R.M., *Mammary epithelial proliferation and estrogen receptor alpha expression in prepubertal heifers: effects of ovariectomy and growth hormone*. J Dairy Sci, 2003. **86**(6): p. 2098-105.
9. Sternlicht, M.D. and Sunnarborg, S.W., *The ADAM17-amphiregulin-EGFR axis in mammary development and cancer*. J Mammary Gland Biol Neoplasia, 2008. **13**(2): p. 181-94.
10. Pascal, J., Bearer, E.L., Wang, Z., Koay, E.J., Curley, S.A., and Cristini, V., *Mechanistic patient-specific predictive correlation of tumor drug response with microenvironment and perfusion measurements*. Proceedings of the National Academy of Sciences of the United States of America, 2013. **110**(35): p. 14266-14271.
11. Wang, Z., Kerketta, R., Chuang, Y.L., Dogra, P., Butner, J.D., Brocato, T.A., Day, A., Xu, R., Shen, H., Simbawa, E., Al-Fhaid, A.S., Mahmoud, S.R., Curley, S.A., Ferrari, M., Koay, E.J., and Cristini, V., *Theory and Experimental Validation of a Spatio-temporal Model of Chemotherapy Transport to Enhance Tumor Cell Kill*. PLoS Comput Biol, 2016. **12**(6): p. e1004969.

12. Wang, Z., Butner, J.D., Kerketta, R., Cristini, V., and Deisboeck, T.S., *Simulating cancer growth with multiscale agent-based modeling*. *Semin Cancer Biol*, 2015. **30**: p. 70-8.
13. Bryan, A.K., Goranov, A., Amon, A., and Manalis, S.R., *Measurement of mass, density, and volume during the cell cycle of yeast*. *Proc Natl Acad Sci U S A*, 2010. **107**(3): p. 999-1004.
14. Deisboeck, T.S., Wang, Z., Macklin, P., and Cristini, V., *Multiscale Cancer Modeling*. *Annual review of biomedical engineering*, 2011. **13**: p. 10.1146/annurev-bioeng-071910-124729.
15. Pascal, J., Ashley, C.E., Wang, Z., Brocato, T.A., Butner, J.D., Carnes, E.C., Koay, E.J., Brinker, C.J., and Cristini, V., *Mechanistic modeling identifies drug-uptake history as predictor of tumor drug resistance and nano-carrier-mediated response*. *ACS Nano*, 2013. **7**(12): p. 11174-82.

CHAPTER 7

A Multiscale, Agent-Based Model of Ductal Carcinoma in Situ

Joseph D. Butner, Vittorio Cristini, and Zhihui Wang

I. Abstract

Ductal Carcinoma in Situ (DCIS) is the most common noninvasive breast cancer, and is characterized by atypical epithelial cell invasion into the mammary gland duct cavity. In order to gain a detailed understanding of the cell-scale population dynamics, phenotypic distributions, and the associated interplay of important molecular signaling pathways are involved in DCIS invasion, we have implemented a multiscale agent-based model of the early stages of disease development. We find that duct invasion rates occur in two distinct regimes, characterized by an early exponential population expansion, followed by long-term steady linear region of population expansion and duct invasion rate. Our results showed that in both regimes, DCIS invasion is influenced most strongly by molecular signaling thresholds and the effects of quiescence induced by cell density within the DCIS population. Furthermore, we show evidence that a complex interplay between phenotypic diversity may provide a tumor adaption mechanism to overcome proliferation limiting conditions, allowing for dynamic phenotypic populations shift in response to variation in molecular signaling intensity. This model serves as a useful tool to study the cell-scale dynamics involved in DCIS initiation and ductal invasion, and may provide insights into promising areas of future experimental research.

II. Introduction

Breast cancer was the most prevalently diagnosed form of cancer in the United States in 2013, with roughly 233,000 new cases diagnosed that year alone [1]. This translates to roughly 12% of women experiencing a positive diagnosis within their lifetime. Carcinomas in situ constitute roughly 20% of all cancers of the breast [2], with the majority (~83%) occurring within the mammary gland duct, known as ductal carcinoma in situ (DCIS). DCIS is a cancer of the luminal epithelial cells, and is characterized by loss of heterogeneity of the luminal cells composing the inner layer of the mammary gland duct, resulting in dysregulated proliferation into the duct cavity. Epithelial cancers are the most common type of human cancers, comprising as many as 90% of all cancer diagnoses [3], making the pursuit of a better understanding of the underlying developmental mechanisms within this cancer subset of utmost importance.

DCIS is hypothesized to develop through a multi-step process, through the initiation of hyperplasia, transition to atypical hyperplasia, and ultimately into ductal carcinoma (we note that we lump these together into one category here, and simply refer to all stages collectively as DCIS) [4]. By definition, DCIS is a stage zero pre-invasive cancer (as it remains contained within the duct despite transition to an unregulated cancer phenotype), and has been associated with increased risk of invasive or recurring breast cancer, although the causal link between the two remains elusive [2]. In order to mitigate this risk, DCIS is usually treated with lumpectomy, often followed by localized radiation treatment. Successful surgical resection of the complete tumor while minimizing patient impact can only be accomplished with clinical identification of accurate and precise surgical margins – a challenging prospect, dependent on thorough understanding of disease

progression and the link between diagnostic imaging (e.g. mammography) and the full extent of disease invasion. In this work, we present a hybrid, multiscale, three-dimensional model of DCIS, which incorporates a cellular phenotypic hierarchy, endocrine and paracrine signaling, and also includes mathematical representation of other factors involved in the DCIS disease state (including signaling pathway disruption, cell-cell interactions and their effect on disease architecture, and hypoxia, necrosis, and post-necrotic cell lysis), in order to help gain a more complete understanding on these clinically relevant parameters.

The mammary gland is a highly branched ductal structure, originating at the nipple, branching out and away from the nipple through the extent of the fat pad, and terminated at the opposite ends by lobules. The duct is a bilayered structure, consisting of an outer myoepithelial layer and an inner luminal layer (see **Figure 7.1**). Both cell populations are maintained by stem cell niches: small subpopulations within the gland of bipotent stem-like epithelial cells [5, 6]. The mammary gland exists only as a rudimentary placode derived structure at birth, and develops primarily during puberty in response to pubertal upregulation of endocrine estrogen signaling. This initiates a complex downstream signaling cascade within the gland, that functions in part by estrogen-induced upregulation of amphiregulin (AREG) production, signaling to downstream phenotypes through an epithelial to stromal paracrine mechanism; in part, this is accomplished through an AREG induced increase in FGF2/7 production in the stroma [7, 8].

Within the mammary gland, epithelial cells are phenotypically distinct based on the presence or lack of estrogen receptor α (here, we refer to the phenotype which expresses the estrogen receptor as estrogen receptor positive: ER+) or fibroblast growth factor

receptor (FGFR), and also based on stem, proliferative, or terminally differentiated phenotype. This results in distinct niches within the signaling pathway, where cells that express ER do not express FGF, and vice versa. Upstream estrogen signals to ER⁺ cells and results in upregulation of AREG production in these cells, followed by an AREG to stroma to epithelial FGF signaling cascade, ultimately signaling to the estrogen receptor α negative (ER⁻)/FGF receptor positive (FGFR⁺) phenotype. Estrogen and FGF are of special importance, as they are shown to induce proliferation within the associated phenotype, both for pubertal development and gland maintenance.

AREG exists as a membrane-bound protein in ER⁺ mammary epithelial cells, and is cleaved into the extracellular space by ADAM17, subsequently signaling to EGFR in the stroma [7-9]. This results in an upregulation of stromal fibroblast growth factor (FGF) production (specific to mammary gland development, at least FGF2 and FGF7 (pubertal) and FGF10 (embryonic) [10]), which reenters the mammary gland epithelium from the stroma, signaling to its receptor FGFR2B (and its isoforms, i.e. IIIc for FGF2 and IIIb for FGF7) [11-13]. This is an important factor in mammary epithelial cell proliferation within the pubertal terminal end bud, as the AREG-FGF pathway has been shown to induce the formation of normal mammary gland architectures in mammary organoid models (and indeed both must be present for pubertal ductal elongation) [13, 14], while pathway inhibition has been shown to hinder pubertal mammary epithelial cell proliferation in FGFR2B mosaic inactivated mice [11]. This pathway persists within mammary gland subsequent to pubertal development, and is involved in mature gland maintenance (and, when broken, may contribute to a breast cancer state). Although not the complete signaling pathway present in the mammary epithelium, this important cascade is critical in inducing

proliferation in the phenotypes not directly stimulated by the estrogen-ER pathway, and is the focus of the molecular cell-cell signaling portion of this study. The cell population in the mature mammary gland ducts becomes largely differentiated subsequent to pubertal development, but retains these distinct phenotype populations, including limited niches of stem/proliferative phenotypes (reported to be ~5% total (or 9% for nulliparous) in the murine gland) [15]. The molecular mechanisms of cell proliferation upregulation (and the associated membrane-bound receptors) are of particular interest in DCIS, as these are often found in excess in the DCIS population.

Cancers of the breast are classified by the presence or absence of three main surface expressed hormone receptors: estrogen receptor (ER), progesterone receptor (PR), and human epidermal growth factor receptor 2 (HER2), as these have been shown to be most associated with cell proliferation in breast cancer. Breast cancers may be positive for one or more of these, or even negative for all three (triple-negative). It has been reported that as many as 75% of DCIS cases are ER α ⁺ (with fewer incidences of PR⁺ and HER2⁺ detected) [16], and the ER⁺ phenotype is associated with greater incidences of transition from DCIS to an invasive phenotype [17]; indeed as many as 70% of all breast cancers are reported as ER⁺ [18]. Estrogen receptor α is of particular interest in disease initiation, as receptor loss of function has been shown to be associated with transition to a DCIS state [19], which may result from an epithelial to mesenchymal transition initiation event (EMT) [9]. DCIS is also classified histologically, based both on cytological features (grade, representative of aggressiveness of DCIS cell proliferation and invasiveness; higher grades are reflective of increased proliferation and invasion) and cellular architecture (cell distribution and density within the duct). The most aggressive phenotype is comedo-type

[20], indicated by aggressive cell proliferation and ductal invasion, axial necrosis, and

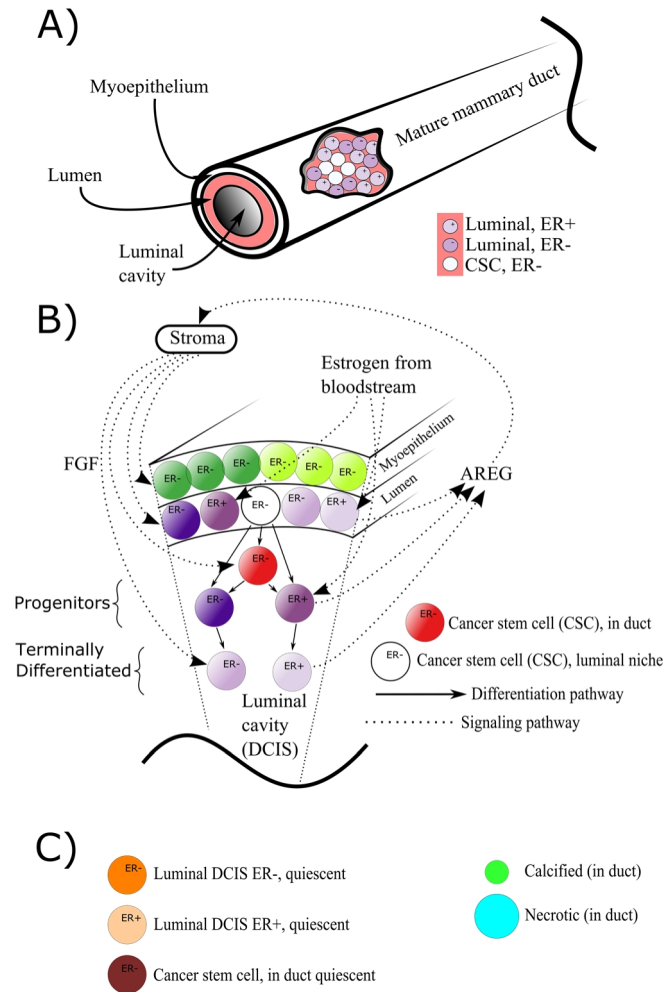


Figure 7.1: Computational domain, cell phenotype hierarchy, and signaling pathways. A) The mature mammary gland duct is composed of an outer myoepithelial layer and an inner liminal layer, both surrounding the duct cavity. At time $t=0$, we initiate an EMT transition to a cancer stem cell (CSC) phenotype within the luminal population, initiating the onset of DCIS. B) Cell hierarchies and signaling pathways are as shown in an expanded view of the duct from A. Cancer stem cells in the liminal layer may proliferate symmetrically, with one daughter remaining in the luminal region to maintain the cell population, and the other daughter placed into the duct cavity. Stem cells may also divide asymmetrically, giving rise to one stem (red) and one progenitor (darker purple) daughter. Cancer stem cells are allowed to proliferate indefinitely, while progenitors may undergo a finite number of proliferations, at which point they become terminally differentiated (light purple). Cell signaling is as shown, with estrogen from the bloodstream signaling to the ER+ population and upregulating proliferation. These cells are stimulated to produce AREG, which leaves through the duct boundary and into the stroma, upregulating production of FGF, which reenters the duct, binding to and upregulating proliferation in the ER- phenotype. C) Quiescent, necrotic, and calcified agent color coding.

subsequent microcalcifications (small accumulations of hydroxyapatite) along the duct axis. Other DCIS architecture types are solid (duct completely filled), cribriform (small holes are seen in DCIS histology), and papillary (characterized by finger-like protrusions within the duct). These architectures are not autonomous, with multiple architectures often found within a single incident of DCIS [2].

In order to elucidate how disruption of the signaling pathways, cell-cell physics, and cellular phenotypic types and hierarchies involved in normal mammary gland development may contribute to DCIS, we implemented a hybrid, multiscale agent-based model (ABM) [21-23] of DCIS. Within the model, cells are represented as unique, discrete entities (agents), while molecular signaling profiles and molecular movement are represented as continuums through a mathematical description using partial differential equations (PDEs, see Continuum Methods below) which are solved numerically for each time step. Within the agent-based model, we implement a cellular phenotypic hierarchy as shown in **Figure 7.1B**. Agents are implemented in a three-dimensional, lattice free system, where all agent interaction and movement is determined exclusively based on cell-cell and molecular level physics. Continuum and discrete scales are explicitly linked mathematically, and feedback between the two scales is explicitly computed at each time step in the simulation. At each time step, agents probe the continuum solutions for information about the molecular concentrations within their microenvironment, and agents modify these profiles based on cellular phenotype and their associated molecular production or consumption. In this work, we use the terms “consumption” to describe any molecular concentrations which are reduced by cell behavior, (e.g. oxygen uptake and metabolism or the binding of signaling molecules to membrane-bound receptors), while

“production” refers to all cell behaviors which increase the concentration of the molecule of interest (for example, cells may produce proteins through RNA translation mechanisms, or they may release already-translated proteins, such as ADAM17 mediated cleavage of preexisting membrane-bound AREG). Agents are bound by rules which are coded to represent literature-supported behaviors, including signaling pathways, receptor expression and overexpression, cell cycle times and limitation of maximum mitosis cycles for proliferative phenotypes, proliferation behaviors, and growth rates and patterns, as well as cancer behaviors such as ductal invasion, phenotypic mutations, and the associated disruptions of cell health often seen accompanying these disruptions, such as increased oxygen consumption within the cancer population and oxygen depletion induced cell hypoxia, necrosis, and lysis.

The approach of studying DCIS through mathematical modeling precedes this work, and indeed inspired several aspects of our model design. Agent-based methods have shown good promise in elucidating the mechanisms of cell-scale factors and behaviors that influence DCIS invasion, such as the effects of cell proliferation and apoptosis [24], phenotypic hierarchies [25], and even treatment [26] on DCIS. Continuum approaches have shed further light into the contribution of proliferation and apoptosis indices on total tumor size [27], as well as other factors in DCIS growth tendencies [28]. Increasingly, these two methods (discrete and continuum) have been combined together to form hybrid models, with discrete representations of the cell scale and continuum representations of the molecular scale, in order to generate a more complete picture of the complex underlying biological system. This is an important step forward in modeling methodology, as biological systems are inherently complex, with dynamic links between and feedback

systems across many spatiotemporal scales, thus justifying the increased computational burden mandated by these increasingly complex hybrid modeling methods. This hybrid approach has been successfully implemented in the study of DCIS. Notably, Paul Macklin implemented a two-dimensional DCIS model, complete with hybridized discrete and continuum scales (including explicit cell-cell interaction physics and molecular diffusion within the gland), which was able to successfully predict DCIS ductal invasion rates, cell density, and transition to hypoxic and necrotic states (and the resulting viable rim thickness), as validated with patient data [29, 30]. Hybrid models of DCIS have also shed insights into the effects of contact inhibition, hypoxia and necrosis, and acidosis on DCIS architecture [31], and the selective influence of these and other factors on the development and evolution of the DCIS phenotype [32].

In the work presented here, we seek to expand upon previous modeling efforts in order to further elucidate the details of DCIS invasion. By inclusion of the estrogen→AREG→FGF signaling pathway, we were able to examine how phenotypic transitions within the DCIS cell population influenced DCIS invasion, including the effects on phenotypic distributions and duct invasion rates as limited by proliferation-dependent molecular signaling and the effects of cell density induced quiescence. At DCIS initiation time $t=0$, the only potential source of AREG production (and its initiation of downstream epithelial cell proliferation) is the ER⁻ population within the luminal layer of the mature gland; this necessitates inclusion of the cell population within the mature gland into the model. This layer also affects estrogen and oxygen concentrations within the duct (as these molecules are consumed or bound by the mature duct cells), as well as influencing the AREG→FGF epithelial to stromal signaling pathway, as both molecules most cross the

mature duct cell layers as a fundamental part of their signaling mechanisms, and their concentrations may be dynamically influenced or changed by the appropriate phenotype as they transverse these layers. Without inclusion of the mature duct cell layers in the model, we expect the model to overestimate the oxygen concentration in the duct (thus introducing an avoidable source of error to the prediction of hypoxic conditions), as well as experiencing similar sources of error within the molecular signaling pathways, such as notably reduced AREG concentrations, which could artificially impede proliferation within the ER- cancer phenotype. Reasonable accuracy in representation of these factors is paramount in studying their effects in DCIS; as such, we attempt to implement a more complete picture of the mammary gland environment surrounding the DCIS population through inclusion of the mature duct layers, in order to better obtain a more complete description of the complicated interplay of molecular- and cell-scale dynamics in DCIS disease progression.

III. Methods

i. Continuum Methods

Molecular signaling is represented as a continuum, described mathematically using a Fick's law description of the reaction-diffusion equation, as described in Equation 7.1,

$$\frac{du}{dt} = D \nabla^2 u + R(u), \quad (7.1)$$

and based on some of our previous modeling work [33]. This partial differential equation describes the time-dependent molecular concentration (u) within the computational domain (e.g. the simulated duct), as dependent on the diffusion constant (D), and as modified by a reaction term (R), which accounts for both molecular consumption/production $U(u)$, as

well as molecular degradation $L(u)$; i.e. $R(u) = U(u) - L(u)$. The distribution profile of each molecule of interest is described individually, and a unique solution is obtained for each molecule at each continuum time step. Time steps for continuum solutions are implemented to be shorter than ABM time steps; thus FEM solution steps are subdivided into even substeps between the ABM time steps to improve solution stability and accuracy (continuum solutions were incremented at $1/30^{\text{th}}$ the ABM time step in results presented here). FEM solutions are obtained on a three-dimensional tetragonal mesh (generated with

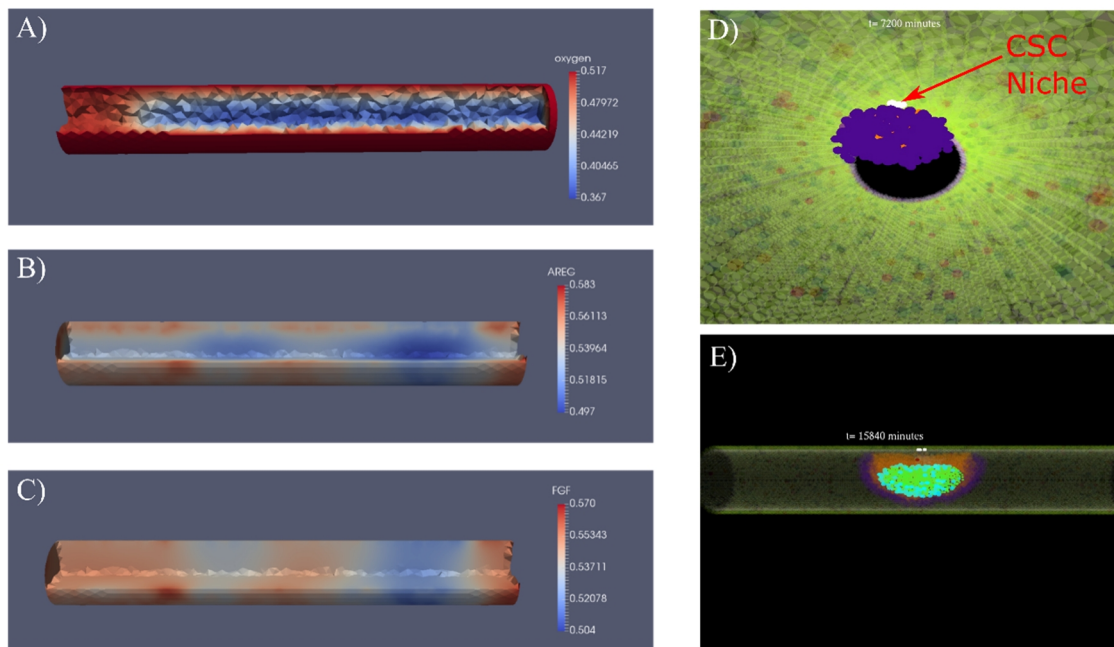


Figure 7.2: Examples of continuum (A-C) and discrete (D,E) model components. Continuum solutions from FEM are shown for A) oxygen, B) AREG, and C) FGF (an example of an estrogen solution is not shown). Oxygen enters into the duct from the boundary under Dirichlet conditions; regions shown in blue where DCIS has reduced the local oxygen conditions. B, C) AREG is produced in the duct by ER⁺ cells (red areas) and diffuses throughout the domain and out of the duct radial boundary. The FGF boundary conditions is derived from the AREG solution (the FGF solution shown in C is the result of the epithelial to stromal signaling mechanism from the AREG solution shown in B). D) Internal view of DCIS five days after the EMT DCIS initiation event; the CSC niche is shown in white. E) AQn example view of DCIS 11 days after the EMT event; the mature duct cells and healthy DCIS progenitors are shown as transparent so the stem phenotype, as well as hypoxia and calcification internal to the DCIS may be seen clearly. A-C, 100 μm diameter duct; D-E, 200 μm diameter duct.

Trelis meshing software, formerly Cubit, see **Figure 7.2A**) using Sundance [34], a high-level finite element method library included as part of Trilinos, a numerical methods package developed by Sandia National Laboratory (examples are shown in **Figure 7.2A-C**).

Boundary conditions are defined to best describe the biological conditions for each molecule of interest. Blood supply to the mammary gland is delivered through a system of surrounding capillaries [35], which we assume to be located directly on the outer duct surface and contain a rapidly replenished blood supply (through circulation) at all times, resulting in a constant concentration of molecules of interest (e.g. oxygen, estrogen) delivered to the duct through the circulatory system at the boundary. To this end, in our model, estrogen and oxygen enter into the system numerically as constant Dirichlet boundary conditions (BCs) for each molecule on the outer surface of the duct (the outer radius, but excluding the ends where we truncate the computational domain into a “duct section”. We apply a constant value u_m (the blood concentration of molecule m) on all boundary nodes $x_{boundary}$), as per

$$BC_m = C_{x_{boundary}}, u_m = Constant_{x_{boundary}} \quad (7.2)$$

and these molecules may diffuse into the domain freely (but according to appropriate diffusion constants) according to Equation 7.1. These molecules may be removed by agents from the local concentration ($R(u)$) due to molecular consumption (oxygen) or binding to the appropriate receptor (estrogen to ER+ agents, and FGF to ER- agents). This reduction in local molecular concentrations is combined with a molecular degradation term ($L(u)$), which accounts for a summation of potential molecular sinks, including molecules lost to agent necrosis/lysis/apoptosis, and the presumed uptake of molecules by other cells within

the mammary duct but not explicitly modeled in the ABM, among other biological factors. These molecular losses are taken to be small, that is $|L(u)| \ll |R(U)|$, but are included in the model for sake of completeness. Specifically, the total change in local molecular concentration u at location x is calculated as

$$R(x, u) = U(x, u) - L(u) = \pm \sum_{i=1}^N \lambda_i H(r_i - |x - a_i|) u - L(u), \quad (3)$$

where r_i and a_i are the radius and center of mass coordinates of the agent, respectively, $H(x)$ is the Heavyside function, and λ_i is the per-volume or per-surface area consumption or production value for the appropriate molecule (positive sign is production, and negative sign is uptake/consumption). We have made the assumption that all cells of the same phenotype (i.e. cancer vs. healthy, or as per cell receptor status, e.g. ER+/-) have the same λ values (and noting that some values are per-surface area or per-volume, such as membrane bound receptors for signaling (a function of cell surface area) vs. oxygen consumption (taken instead to be a function of cytoplasmic volume)).

Within discretized numerical approximations of mathematical functions, the solution is only known exactly at the nodes, and as such, these discrete modifications to the continuum solution must also be applied at the nodes (for more details, see Hybridization of Models section, below). The magnitudes of local molecular concentrations are computed as the average values from all agents with their center of mass a_i closest to each node (as determined through Voronoi tessellation, a method of subdividing the domain into regions which enclose the volume closest to each node), normalized into per-volume or per-surface area values, and applied to the appropriate node of interest numerically through application of a Dirac delta function, defined as

$$U(u) = \frac{\sum_{i=1}^n \lambda_i u}{n} \int_{-\infty}^{\infty} \delta(x - a_i) dx, \quad (4)$$

where n is the number of agents in the Voronoi cell. To simplify calculations, we take the total volume (and thus the total contribution to molecular molecule concentration profiles) of the agent to be within the Voronoi cell containing its center of mass; thus the total values for each cell are implemented into the continuum solution entirely at the nearest node. By subdividing the mesh into elements of similar length to the mature agent diameter (noting that when a cell divides, its daughters have reduced diameter, and both may at that time have increased likelihood of sharing the same nearest node until they grow in the G2 phase), we have attempted to ensure that only a small number of agents are associated with each node, thus maintaining an acceptable degree of precision within this approximation.

AREG is produced by the ER- phenotype within the myoepithelial and luminal duct layers, as well as within the ER- DCIS population, and we take these to be the only AREG source in the model, e.g. AREG is assumed not to enter from any sources in the region surrounding the duct, and the concentration of free AREG outside the duct is minimal (as AREG that enters this region is assumed to be rapidly bound to EGFR in the stroma). To this end, we assume that AREG is free to diffuse out of the domain across the outer radial boundary under the same conditions that it diffuses through the domain. This is accomplished through the implementation of homogenous Neumann boundary conditions, with molecular concentration attenuating toward equilibrium at the far-field. Biologically, the AREG that leaves the duct signals to EGFR in the stroma, stimulating an epithelial to stromal cascade which results in FGF reentering the duct. We assume a 1:1 relationship between the normalized concentration (C) of AREG that leave the duct and the corresponding normalized concentration of downstream FGF that reenters. Numerically, we implement this as a time-dependent Dirichlet boundary condition, defined for each time

step (t) as a function of the per-node values of the AREG solution from the previous time step (t-1) as

$$BC_{FGF_t} = C x_i, u_{AREG_i}{}_{t-1}, (i = 1 \dots n_i) \quad (5)$$

for each node n_i . At each time step, we store the value for the AREG solution at each boundary node, and then use these values for the Dirichlet boundary condition for the subsequent time step in the downstream FGF solution. In this way, a direct downstream epithelial to stromal signaling mechanism is implemented (but with a time delay of 1 ABM step, approximating the time delay for the occurrence of the signaling cascade steps which occur in the stroma, but are not explicitly modeled here), providing a reasonable approximation of the epithelial to stromal signaling pathway. An example of FEM solutions for the AREG→FGF epithelial to stromal pathway is shown in **Figure 7.2B, C**.

We have strived to, whenever possible, implement biologically relevant, literature supported values in these equations. Movement and consumption of oxygen at the cell level is well characterized, with oxygen diffusion constants reported in a wide range, of between 4×10^{-8} to 1.1×10^{-4} cm^2/s [36]; accordingly, we take a somewhat median value of $D = 2.57 \times 10^{-6}$ cm^2/s as reported in [37]. Oxygen consumption of a single cell is in the 10^{-18} – 10^{-16} $\text{Mol}/(\text{cell} \cdot \text{s})$ range; these are reported in the $2.5\text{-}45 \times 10^{-18}$ $\text{Mol}/(\text{cell} \cdot \text{s})$ range for healthy cells (depending on cell states, with lower consumption for mature/senescent cells and higher consumption for proliferating cells), with further increased consumption for cancer cells [38]. Specifically, oxygen consumption rates have been measured (in cell culture) up to 150×10^{-18} $\text{Mol}/(\text{cell} \cdot \text{s})$ for EMTGIRO murine mammary tumor cells in exponential growth (and lower in the plateau phase, at 100×10^{-18} $\text{Mol}/(\text{cell} \cdot \text{s})$), and up to 260×10^{-18} $\text{Mol}/(\text{cell} \cdot \text{s})$ for the MCF-7 breast cancer cell line [38] (estimated from Table

2 and Figure 2 in [38], and using a standard mammary cell diameter of $10\mu\text{m}$). We have used oxygen values with units of 10^{-18} Mol (e.g. atto-Mol) to be consistent with the units reported for per-cell oxygen consumption, and to maximize precision in our numerical solvers. Specifically, our FEM solver Sundance uses `std::double` variables (which give a maximum 16 reliable significant digits) to solve the FEM. This means that a value of 10^{-18} may be rounded to zero (depending on compiler implementation, etc.), and is not reliable for units in Mol; thus we avoid this possibility while increasing solution precision through use of atto-Mol.

For boundary conditions, blood oxygen concentrations is taken to be 100mmHg [39], while female pubertal blood estrogen concentrations are lower than oxygen concentrations (median of 70.3 pMol/liter [40]; and lower still post-menopause, when most DCIS occurs). Per-cell uptake rates for estrogen, as well as quantification of AREG and FGF local concentrations, were not found in the literature; accordingly, we have instead opted to use normalized concentrations for these values, with uptake/binding/secretion rates calibrated phenomenologically to accurately reproduce biologically appropriate behaviors, as we also did in a model of the developing pubertal mammary gland [33]. Likewise, diffusion constants for these molecules were estimated using a combination of known diffusion coefficients for similar molecules, linearly interpolated in order to estimate their diffusion constants, as based on relative molecular weights.

ii. *Discrete Methods*

Cells in the mature mammary gland and the DCIS population are represented discretely through implementation of an agent-based model. Each cell agent is unique, with

its own geographical coordinates, phenotype, receptor status, size, cell generation number, and cell state. Agents proliferate as instructed through molecular signaling, and as allowed by phenotype, neighbor density, and cell cycle time restrictions. Cells may only proliferate when molecular signaling thresholds are satisfied, when they are not induced into quiescence due to agent density restrictions, and only after a full cell cycle has occurred after their last mitosis event, taken to be ≥ 16 hours (see **Table 7.1**). For example, a new daughter cell of the ER+ phenotype must complete interphase (some parts we explicitly

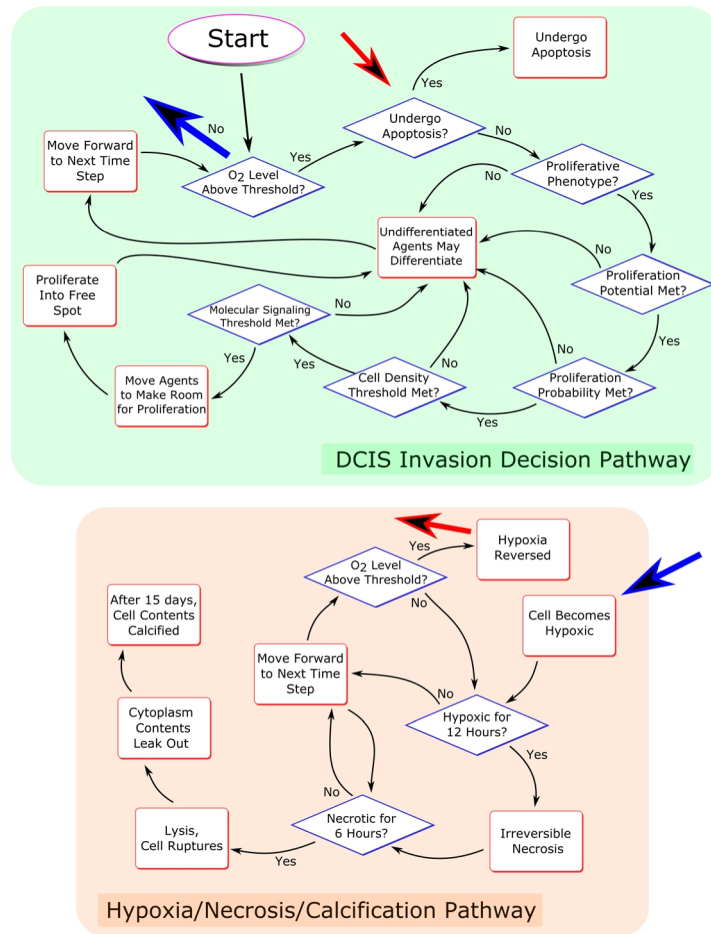


Figure 7.3: Agent decision flowchart. Agent decisions are made according to rules shown for each time step of the discrete model. Blue and red arrows indicate transition pathways between top and bottom boxes (shown without complete arrows connecting the two regions for clarity).

model, such as cell growth, and others we do not, such as subcellular processes, as they are not the focus of this study), before it is eligible to proliferate again. After the completion of interphase, our example cell (now mature) queries its local environment to determine the estrogen concentration at its location and to ensure oxygen levels are sufficient to avoid hypoxia, as well as to determine the local cell density. If the molecular concentrations are above a determined threshold, and local cell density is below the density threshold, then the agent chooses a random orientation for mitosis (e.g. mitotic spindle and cleave furrow orientation). When all conditions for the mitosis event are satisfied, the cell divides, splitting its cytoplasmic volume and plasma membrane contents evenly between its daughters. Likewise, similar conditions must be met for the other phenotype within the DCIS population as well, i.e. FGF signaling thresholds for ER- cells. This decision-making process is described graphically in **Figure 7.3**.

In order to ensure the simulated DCIS cancer growth remains in stage zero (the focus of this study), agents are bound to remain within the duct cavity (defined by the luminal inner layer of the mature duct), and may not metastasize to penetrate the duct. However, agent movement is not restricted within the duct, and agents may move freely within the duct as influenced by cell-cell physics, which are solved and updated after all cell conformational/position change events (i.e. mitosis, movement, growth, lysis-induced swelling and cell rupture, etc.). Cells may be displaced by events in neighboring agents (e.g. movement, proliferation, growth), and are infinitely complacent to displacement; thus growth or proliferation of a cell in the center of the DCIS population has the potential to cascade displacement throughout the entire DCIS population, even to the leading edge of the tumor, as determined though solving the system of equations describing the interactions

between all cells in the physics world. Cells adhere to neighboring cells through application of cell-cell adhesion forces, and are resistant to displacement due to these forces, which are implemented mathematically as a combination of forces which adhere the cells together (applied mathematically as force vectors at the center of mass of each cell along a vector between their centers of mass), as well as static, kinetic, and rolling friction. Cells may also deform due to forces applied from surrounding cells, which we represent mathematically as a loss of energy through a coefficient of restitution (and thus not modeled explicitly as a change in shape of the plasma membrane). However, because two cells may not occupy the same space, ultimately cells must be complacent to their neighbors, and thus displacement forces will always overcome the resistant forces to accommodate this requirement, although these forces do play a direct role in determining which displacements will occur.

Cells in the model follow a cell hierarchy as shown in **Figure 7.1A**. At time $t=0$, we allow a small number of cells in the luminal layer of the mature duct to undergo EMT to a cancer stem cell (CSC) phenotype (shown in white, **Figure 7.1A** and **Figure 7.2D**). Each CSC is seeded to be at a random time within the cell cycle, through implementation of an internal counter which records the time since the cell's last mitosis event. This counter is incremented for each agent each time the ABM time is stepped forward, and the agent may not proliferate again until the counter value is at least equal to the cell cycle time (16 hours, see **Table 7.1**), and provided the molecular and cell density thresholds are also satisfied. Stem cells are taken to have unlimited proliferation potential, and may thus proliferate an unlimited number of times. Within the simulated cell hierarchy, the luminal

progenitor phenotype is directly below cancer stem cells in the cell hierarchy, and these may proliferate over many cycles, as bounded by literature supported values.

Normal mammary epithelial cells have been observed to divide 55-60x in culture, and even up to more than 250 cycles through immortalization with *c-myc* or its direct transcriptional target, hTERT (the human telomerase subunit responsible for catalysis) [41, 42]. Although cancer cells are known to experience a level of immortalization, we choose to limit DCIS proliferation potentials to the lower end of this spectrum, to ≤ 50 mitosis cycles before differentiation. Cells are proliferation restricted by surrounding cell density, and will become quiescent if the density crosses a certain threshold; however, this restriction is reversible, and if density of the surrounding cells is reduced due to cell death or movement, then the cell may again proliferate (much like how cells are known to often cease population doublings when they become confluent in culture, but may resume mitosis once the confluent cells are split into a set of new dishes, thus relaxing the effects of confluent population density). Cells which proliferate the maximum number of cycles will spontaneously differentiate subsequent to their last mitosis event and become terminally differentiated. We note that it is possible for the maximum number of proliferation cycles before differentiation to exceed the time simulated in the model runs presented here; in this case, the differentiated phenotype is not observed. However, due to limitations in cell signaling and cell density, progenitors may often become quiescent (shown as orange, with different shades indicating phenotype), thus having a similar effect on total population dynamics without undergoing a terminal differentiation.

Aggressive cell proliferation in the absence of a properly developed vasculature (as often observed in solid tumors) often results in restrictions of oxygen availability, hypoxia,

and even hypoxia-induced necrosis. Hypoxia is commonly seen in DCIS in ducts over a certain size; hypoxia-induced necrosis has been reported in up to 94% of ducts of diameter $>360\mu\text{m}$, but only 34% of ducts with diameter $<360\mu\text{m}$, with an average viable rim thickness of $180\mu\text{m}$ before hypoxia onset [43]. This is due, in part, to increased oxygen consumption rates in mammary cancer cells, reported to be 150-260 attoMol/(cell*s) for EMTGIRo and MCF-7 cell lines, respectively, relative to 2.5-45 attoMol/(cell*s) for healthy cells (depending on cell type and cell phase, i.e. quiescence vs. mitosis phases) [38]; this translates into an increase of up to ~ 100 fold oxygen consumption in cancer cells. Cancer cells have been reported to enter hypoxia when local oxygen supply drops below 8-10 mmHg [39, 44], and at about 1/3 the normoxia concentration observed in the healthy tissue [39] (we use the 1/3 normoxia concentration quantifier in the work presented here), and cells in the model will enter irreversible hypoxia induced necrosis after 12 hours of continuous hypoxia based on values reported in [45]. Subsequent to necrotic death, cells enter a lysis phase, swell under lysis conditions until the plasma membrane ruptures after ~ 6 hours as per [46] (mammalian cells may swell from 1-5x up to at least 10x their original volume during lysis [47-49], although we use 2x in this work, as seen in previous DCIS modeling work [30]), resulting in their cytoplasmic contents being released into the luminal cavity. Leaked cytoplasmic contents may then form microcalcifications (as seen in mammographic imaging); here we take the calcified volume to be 30% of the volume of the cell volume at the time of lysis initiation (as cytoplasm is reported to be roughly 70% water [50]), with a calcification time of 15 days. In the model, hypoxic cells are shown in grey, and both cytoplasmic spilled from a lysis process and the subsequently calcified cytoplasmic remains are shown as bright green (for ease of visibility). We note that we

have made the assumption that, due to mutations resultant in the cancer phenotype, apoptosis pathways are turned off in the DCIS populations; thus all cell death in the model is due to this hypoxia and necrosis pathway.

iii. Hybridization of Models

In our model, the continuum and discrete components are explicitly linked mathematically, resulting in a hybrid model. Information is directly communicated between the scales at each time step in all simulations, and each scale component is directly affected by, and directly affects, the other. Agents in the discrete scale receives information about their microenvironments directly from the continuum scale. Each agent probes its microenvironment at the beginning of each time step in order to determine the local concentration of all molecules represented in the continuum scale at its location (for simplicity, agent location is taken to be its center of mass). Because the solutions of continuum molecular profiles are only known exactly at the node locations, agents must interpolate the concentration at their location from the values at its nearest nodes. Each agent identifies its nearest nodes at each time step (exactly 4 nodes per agent, as continuum solutions are determined on tetragonal meshes, consisting of the 4 nearest nodes which encompass the agent's center of mass), reads the values at each node, and interpolates the value at its location from these known node coordinates and values using linear barycentric interpolation (a method where the value at each node is weighted relative to the distance of each node from the agent location, and each weighted value is then summed to give the interpolated value). Agents also feedback into the continuum scale through direct modification of the continuum solutions, based in part on their phenotype (see **Figure**

7.1B), as described in detail in the Continuum Methods section. Through explicit linking of discrete and continuum scales, the model is able to provide detailed information about interplay between tissue and cell scales, and to give useful insights into the contributions of molecular factors involved in determining behavior observed at a cellular level, and thus providing information not available through either discrete or continuum method alone.

IV. Results

We have implemented our DCIS model to simulate the earliest stages of DCIS invasion in a section of simulated duct. Simulations were performed in three different diameters of mammary gland duct sections (50, 75, and 100 μm luminal cavity radii; i.e. the thickness of luminal and myoepithelial layers in the mature duct are not included in this measurement, but rather surround a luminal cavity of this diameter), each represented as a cylinder of duct 1mm in length axially. At the start of each simulation ($t=0$), a small number of cells in the mature luminal layer of the duct undergo an EMT transition into a cancer stem cell (CSC) phenotype. These CSCs may proliferate indefinitely, placing their daughters into the luminal cavity, as determined by cell phenotypic hierarchies shown in **Figure 7.1**. These and all daughter cells may continue to proliferate, as determined by mitosis threshold rules (see **Table 7.1**) and satisfaction of molecular signaling thresholds. CSCs are initiated at the center of the duct axis (e.g., in a 1,000 μm axial length duct section, they would be placed as close to axial location $x = 500\mu\text{m}$ as possible), with all CSCs in a contiguous location. For consistency, we seed a standard set of agent locations (though each non-CSC agent has a stochastically determined phenotype, unique to each simulation) in the mature duct layers, resulting in EMT transition at the same agent locations for all

simulations of a certain duct diameter. The DCIS population may invade the duct in both axial directions simultaneously (e.g. x^+ , x^-) away from this central locations; thus total ductal invasion is taken to be the summed magnitude of cell invasion bidirectionally from the CSC niche, as determined by the center of mass of the agent at the most extreme axial displacement in both directions (e.g. x_{\min} and x_{\max}). At each step, details of each agent (locations, phenotypes, cell states, etc.) are recorded, and results are detailed in the sections below.

Model outputs of interest reported here include the extent of DCIS invasion (measured as described in the previous paragraph), the associated DCIS axial invasion rates (calculated by linear fitting to the data to total invasion extent at each time point, e.g. $= |x_{\max,t} - x_{\min,t}|$, and extrapolated to a mm/year rate, corresponding to invasion units reported in the literature) and total DCIS cell population, as well as extent of hypoxia and calcification when appropriate. Furthermore, we have been diligent to correlate and compare model outputs to values available in the literature, when available. All model results presented here were obtained from simulations run in equal wall clock times on the Lonestar 5 supercomputer, located at the Texas Advanced Computing Center (TACC), The University of Texas at Austin [51].

i. Establishment of Baseline Values

We have strived, to the best of our ability, to obtain literature-supported values for variables implemented in this work. Commonly, this means selecting a value from the range of reported values, which we use as a baseline (or constant) value in all results presented. Other values, such as mammary gland duct diameter, are chosen from a range

of reported values which may allow us to observe behaviors of interest, while remaining within a computationally feasible continuum and discrete description. When values are not available from the literature, or when a quantity of interest remains underdetermined even with the variables we were able to find in the literature, then we have calibrated the model phenomenologically to accurately reproduce behaviors we are able to obtain from the literature. For example, while we do not know a reported value of cell mitosis events per time, we do know DCIS axial invasion per year. These two values are inherently linked, and we may calibrate the conditions which influence cell proliferation rate such that it results in ductal invasion rates which are known. We have tested the effects of perturbations of one or more baseline value in order to test its effect on the model results, with careful attention to avoid creating compounding variable situations through perturbations of many variables in parallel. Unless specifically stated, all variable values were set at the baselines for all results shown. The calibration of some of these is detailed below, and baseline values are provided in **Table 7.1**

ii. *The number of EMT-generated Stem Cells in the CSC Niche has Minimal Effect on DCIS Invasion Rates*

In our model, DCIS initiation occurs through a spontaneous EMT event, where one or more healthy cells in the mature luminal duct layer undergo a transition to a cancerous stem cell phenotype. In order to gain insights into the effects of the number of cells which experience this EMT event on DCIS initiation and early stage development, we performed a set of experiments testing the effects of the number of CSCs initiated at $t=0$ within a single CSC niche. In order to avoid the effects of confounding variables within the model,

we removed the effect of molecular signaling thresholds in this case; that is, we assume that each progenitor cell is always under favorable signaling conditions for proliferation, and it may undergo a proliferation event when it has completed the previous cell cycle, as allowed by cell density restrictions. We assumed that the number of cells undergoing this transition will be relatively small, and may occur in one or a small cluster of cells, as lineage tracing studies of the mature mammary gland homeostasis maintenance process have shown that over time, many contiguous cells may share a common mother and clonal lineage [5], and thus we assume they may also share a common susceptibility to the EMT

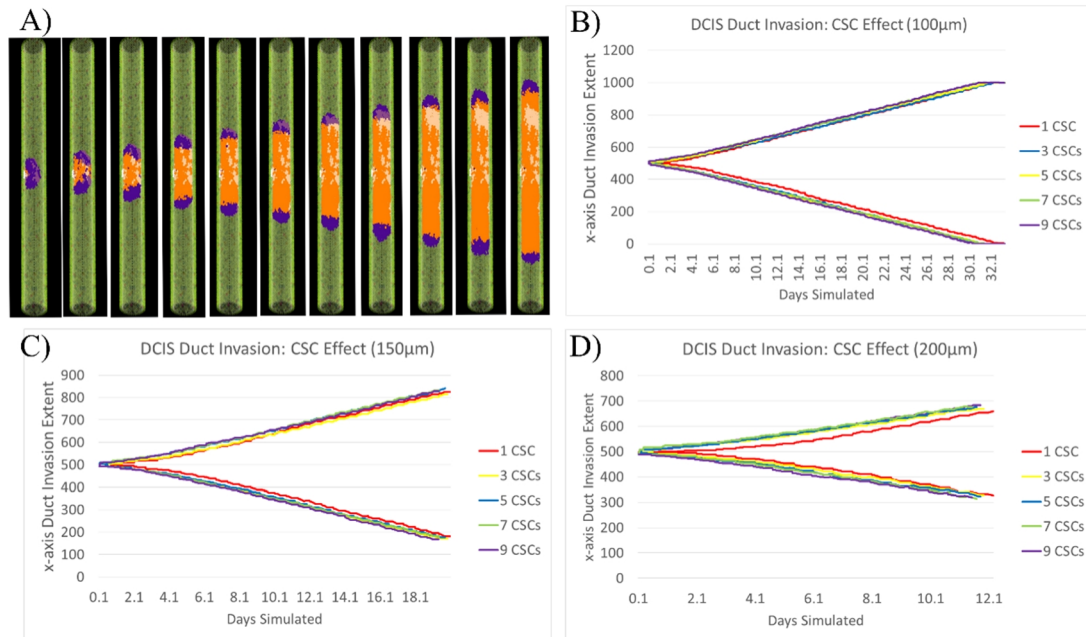


Figure 7.4: Effects of variation in CSC count within the EMT-generated niche on DCIS invasion. A) An example of simulation output over time (100 μ m duct, no thresholds); plots in B-D show the position over time of the DCIS agent with maximum axial duct invasion extent in both axial directions, taken as the agent's center of mass. B-D) Effects of variation within the number of CSC initiated at $t=0$ in three duct sizes (B=100 μ m, C=150 μ m, D=200 μ m). Duct axial invasion rates are seen to be relatively consistent, with only minor effects at early times (e.g. 1 CSC data (red) can be seen to show slower axial invasion at early times, while 9 CSCs (purple) shows the opposite effect); however these effects are seen to be overcome when growth enters the linear region (see **Figure 7.5** for more information).

transition. Under this assumption, we tested the effects of initiation of a CSC phenotype in 1-9 luminal cells (specifically, 1, 3, 5, 7, and 9 CSCs) at $t=0$ on DCIS population expansion rates and early duct invasion rates, as shown in **Figure 7.4**.

By examining the extent of DCIS invasion over time, we discovered that the number of CSCs initiated in the niche at time $t=0$ had a negligible influence on the total DCIS invasion extent and rate of invasion for all three duct sizes tested. Average growth rates over the time were estimated by linear fitting of data shown in **Figure 7.4**, and were found to increase from 11.84 to 11.87mm/year for the 100 μ m duct, 12.82 to 12.89mm/year for the 150 μ m duct, and 10.78 to 11.21mm/year for the 200 μ m duct (a 0.25%, 0.55%, and 3.99% difference, respectively); demonstrating only minimal influence of cell number variations in the CSC niche on duct axial invasion rates. Further insights and likely causes of this observation are provided in the Discussion section, below. Based on the minimal effect of variations in the number of cells in the initial SCS niche, we expect the number of CSCs chosen for the remainder of our simulations to impart only a small effect on DCIS population dynamics after enough simulated time (if at all), and thus chose a median value of 5 CSCs to serve as the baseline for the rest of the simulations presented here.

iii. Early-stage DCIS Invasion Occurs in Two Distinct Growth Regimes

Examination of the total DCIS cell count over time reveals two distinct regions of cell proliferation behavior: an early, transient exponential growth period, followed by an extended linear growth period. This behavior is observed in all duct sizes (see **Figure 7.5**), and for all numbers of CSCs seeded in the CSC niche niche (data not shown). The transition period between these regions is indicated in **Figure 7.5** by a set of vertical dashed lines,

with the exponential region to the left of this region (early times) and the linear growth regions to the right. The exponential growth region is shorter in smaller duct sizes, with an exponential growth period of ~ 4.25 days for the $100\mu\text{m}$ duct and ~ 5.9 days for the $200\mu\text{m}$ duct. This biphasic pattern of DCIS population increase is observed to be irreversible, and once a transition from exponential to linear growth occurs, the model will remain in the linear growth pattern for the rest of the simulation.

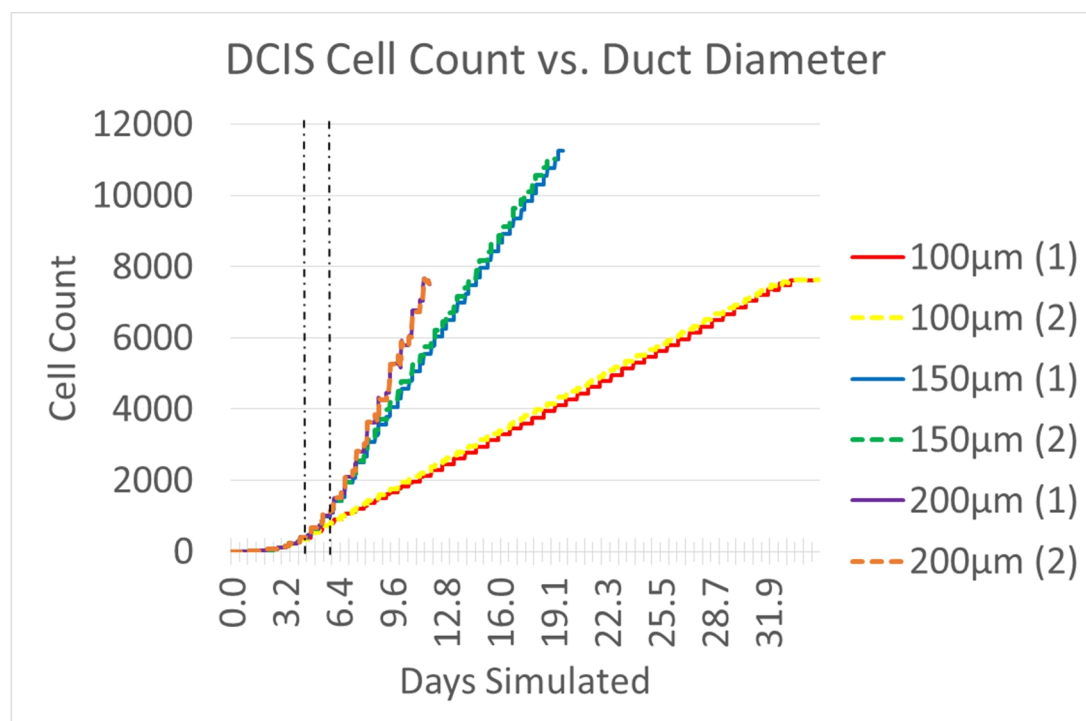


Figure 7.5: DCIS cell population expansion occurs over two distinct regimes. At early times after DCIS initiation, cell population is observed to undergo exponential growth (left of dashed lines), with population doublings occurring once per cell cycle (data shown here with no signaling threshold proliferation limiting effects; each test was performed in duplicate, data from both tests is shown (1 and 2)). Once the cell population has increased to a population size where cell density proliferation threshold effects are initiated, the population transitions from an exponential to a linear growth regime (observed between the dashed lines). Subsequent to this transition, the population remains in a linear growth pattern (right of dashed lines). All data shown with 5 CSCs initiated at $t=0$ and without signaling threshold effects.

iv. *DCIS Axial Invasion Rates are Consistent over all Duct Sizes Tested*

The mammary ductal structure possesses significant variation in duct diameter, which has been reported to range from tens of microns to several mm [27, 43]. Duct radius shows significant variation even within a single patient, and this effect is further exaggerated between healthy and ducts containing intraductal carcinoma. In a study measuring 1,285 excised human mammary ducts, Mayr et. al. reported a mean diameter of 90 μ m for the normal duct (520 samples, range 39-314 μ m), but a statistically significant increased mean diameter of 314 μ m (765 samples, range 60-1708 μ m) in ducts with intraductal carcinoma [43]. Of the ducts measured, ~97% of healthy ducts and ~30% of ducts containing intraductal carcinoma were found to be <200 μ m diameter. This significant variation in duct diameter between healthy and ducts containing DCIS is due (at least in part) to a DCIS invasion induced increase in duct diameter, where the duct is mechanically stretched beyond its initial diameter by the expanding tumor. We do not represent this phenomena in our current efforts; instead, we assume that, because we simulate the earliest stages of DCIS initiation and invasion, the duct does not expand under intraductal pressure from the DCIS expansion at this early stage of development. Accordingly, we select our duct sizes to be within this reported range of smaller ducts, and thus have implemented 100-200 μ m diameter ducts.

To test the influence of duct diameter on the ductal invasion rate of DCIS, we performed ran simulations (in duplicate) in all three duct diameters tested under baseline values, but without the effects of simulation thresholding, as shown in **Figure 7.6**. Because of the complex interplay between the distribution of cell phenotypes and the associated upstream (e.g. estrogen) and downstream (e.g. AREG, FGF) signaling, DCIS invasion rates

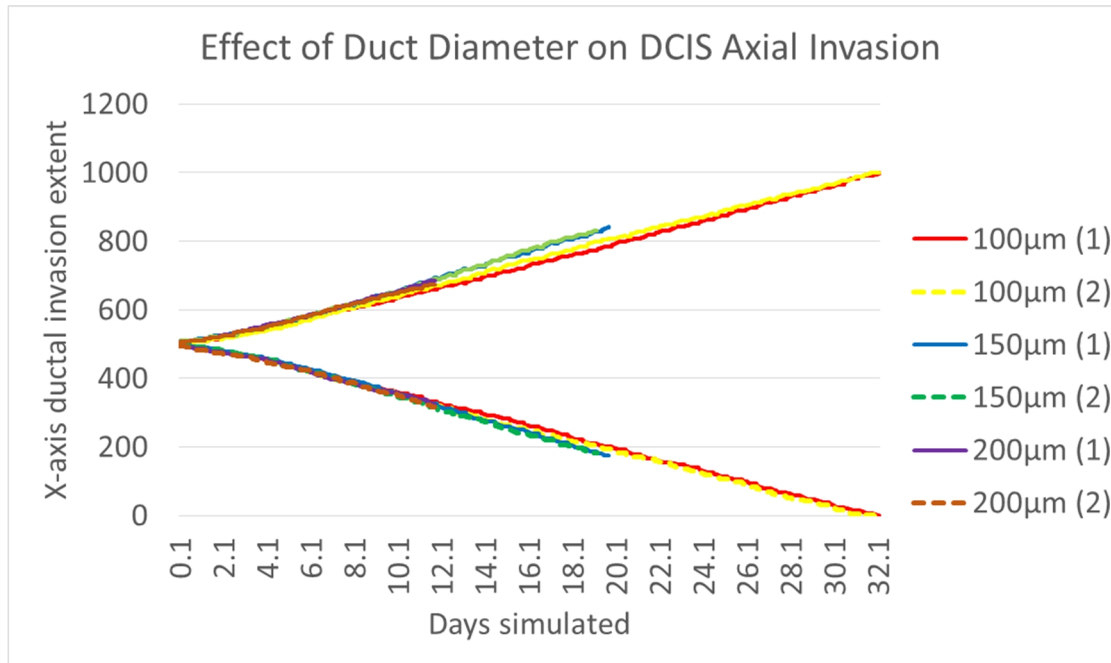


Figure 7.6: Effect of duct diameter on DCIS axial duct invasion extent over time. Measured DCIS axial invasion, corresponding to data shown in **Figure 7.5**. Axial invasion rate and extent of invasion is observed to be consistent across all duct axis tested.

under signaling threshold effects may experience significant variation; thus we remove this effect to eliminate interaction of these variables to better examine only the effects of variation of the duct diameter. Thus, as in the previous experiment testing effects of CSC number, we assume molecular signaling threshold are satisfied for all progenitor cells within the DCIS population. Interestingly, we observed that DCIS axial invasion rates were small between the different duct diameters, with average ductal invasion rates (as estimated by linear curve fitting) averaging from 11.23 mm/year for the 200μm duct to 12.95mm/year for the 150μm duct (and a more centralized rate of 11.91mm/year for the 100μm duct), for a total observed variation in DCIS axial invasion rate of 15.32% vs. a 100% duct diameter variation across all duct diameters tested. This relatively small variation of axial invasion rate relative to the variation in duct diameter is largely due to the effects of cell density in this case, and is examined more thoroughly in the Discussion section, below.

v. *Necrosis Acts as a Hypoxia Relief Mechanism*

Cells in our model will become hypoxic when their local oxygen concentration drops below a threshold, and cell that remain hypoxic for more than 6 hours will undergo necrosis, lysis until plasma membrane rupture, and then leak cytoplasmic contents, which become calcified after time (for details and values, please see Discrete Methods and **Table 7.1**). Oxygen enters the duct from the outer boundary, and must pass through the outer myoepithelial and luminal mature duct layers before entering the duct cavity; oxygen entering the duct cavity is reduced due to uptake by cells in these layers. Due to the relationship between duct radius and the Krogh length of oxygen in this tissue (based on values in **Table 7.1**, and noting that cancer cells have the greatest influence on Krogh length, as they consume more oxygen than the surrounding healthy duct), oxygen remains plentiful in the 100 μ m and 150 μ m diameter ducts, and hypoxic conditions were only observed in the 200 μ m duct; this is consistent with values reported by Mayr et. al. [43].

In the 200 μ m duct, hypoxic conditions were observed to follow the leading edge of the tumor, once tumor thickness has exceeded the Krogh length for oxygen radially. Because we assume a constant blood oxygen concentration at the duct boundary, the oxygen threshold at the center of the DCIS mass will remain below the hypoxia threshold unless local cellular oxygen consumption is reduced. While cells may be displaced out of this region, more commonly we observed that this is not the case, due to the high density of cells surrounding this region. Usually, hypoxic conditions were relieved through the course of hypoxia induced necrosis of agents in the hypoxic region – the death of these cells reduced the oxygen consumption burden in these regions, allowing oxygen concentration to increase slightly in these locations in subsequent time steps, and thus

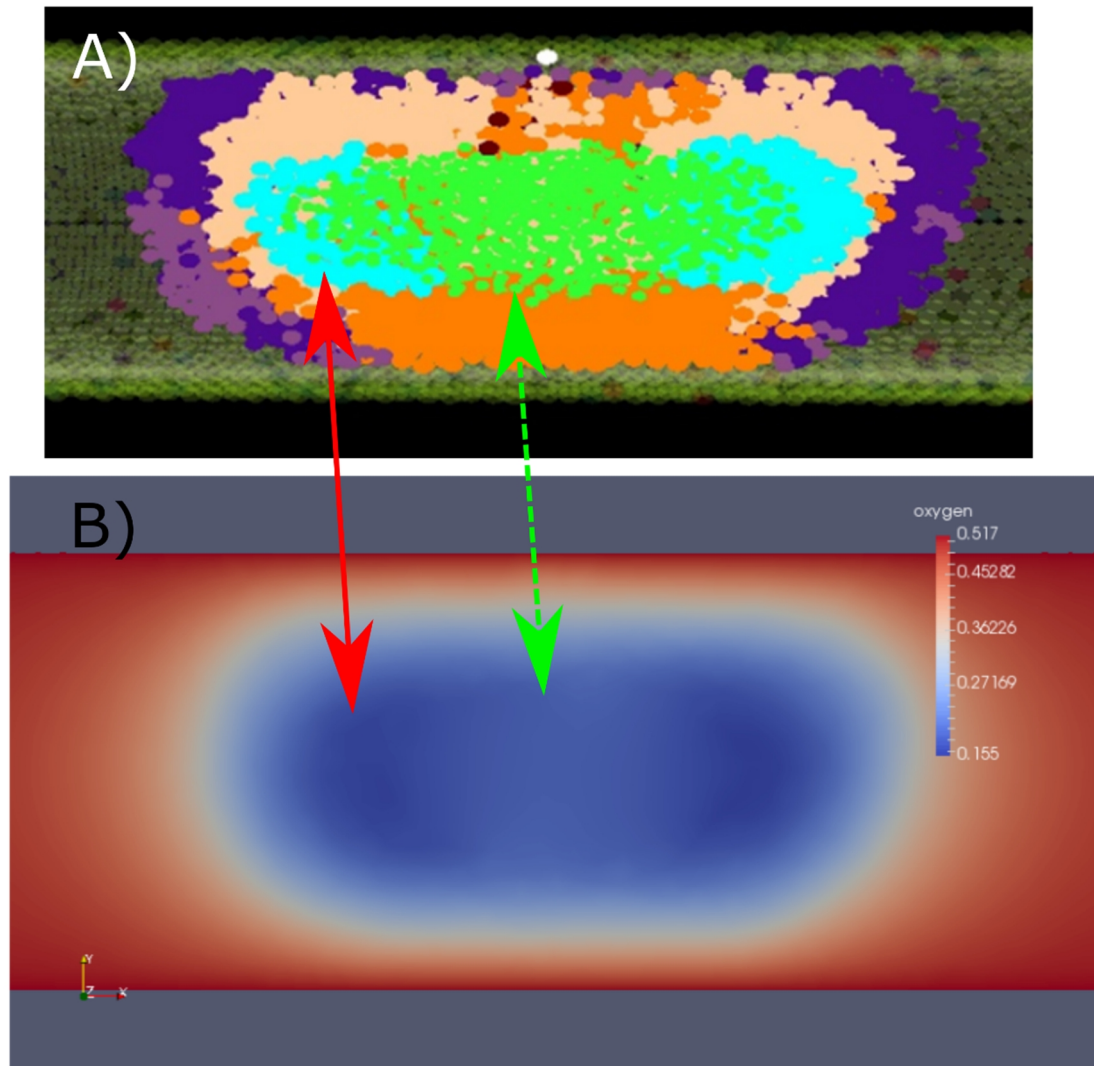


Figure 7.7: Necrosis acts as a partial relief mechanism for hypoxia. Lowest oxygen concentrations are observed in the location of necrotic agents in the DCIS population, following the leading edge of DCIS (red arrow, solid). In regions of calcification, oxygen concentrations are observed to raise slightly (green arrow, dashed), due to the relief mechanism of necrosis and calcification through reduction of oxygen consumption at these locations. Oxygen concentration units: $10^{-1} \frac{\text{atto-Mol}}{\mu\text{m}^3}$, for consistency with units for per cell oxygen consumption as provided in [38] (see Methods for more information). Both images are shown as a cross-section taken vertically through the duct to show cell and molecular profiles internal to the DCIS region.

reducing the slope of the oxygen gradient along the duct radius in these locations; this effect is shown in **Figure 7.7**. In this way, necrosis was observed to function as a relief

mechanism for hypoxic conditions, allowing local oxygen concentration to rebound slightly, ensuring the remaining cancer population is sufficiently oxygenated, as well as potentially allowing some cells to survive their hypoxia and return to normoxic conditions due to the local oxygen concentration recovery.

vi. *Molecular Signaling Effects*

In order to examine the effects of molecular signaling pathways, we tested the model in the case of both high and low signaling thresholds for both estrogen (upregulates ER+ cell proliferation) and FGF (upregulates ER- cell proliferation). We define the molecular signaling threshold as the signaling intensity above which a cell is upregulated to proliferate; when thresholds are high, the cell must be stimulated by high local molecular concentration before it experiences upregulation of a mitosis event, while conversely, when thresholds are low, a cell may be stimulated to undergo a mitosis event under low local molecular concentration. In order to test the effects of these pathways, we performed a series of threshold proliferation tests in the 100 μ m duct. In all tests, estrogen, AREG, and FGF release/uptake values are at the same value, i.e. ER+ cells bind to estrogen at the same rate, and release AREG at the same rate, in all tests performed, and likewise all ER- cells bind to FGF at the same rate. Thus, we perturb the sensitivity of the cells against a standard signaling intensity in order to simulate a potential phenotypic transition that causes a deviation in sensitivity to molecular signaling, potentially upregulating proliferation in the DCIS phenotype.

DCIS axial invasion rates were seen to be sensitive to signaling thresholds, as high thresholds limit mitosis events, resulting in slower population expansion and fewer DCIS

cells over time relative to the low threshold case (**Figure 7.8** curve 0; this low threshold case was also used in data presented in **Figures 7.4-6**). Furthermore, this effect was more pronounced in the high estrogen threshold case (**Figure 7.8** curves 4 and 5), while low estrogen signaling thresholds show lesser reduction in DCIS axial invasion, even with high FGF thresholds (**Figure 7.8** curve 2). This effect is attributed to the upstream to downstream effect of the estrogen to FGF epithelial to stromal signaling pathways.

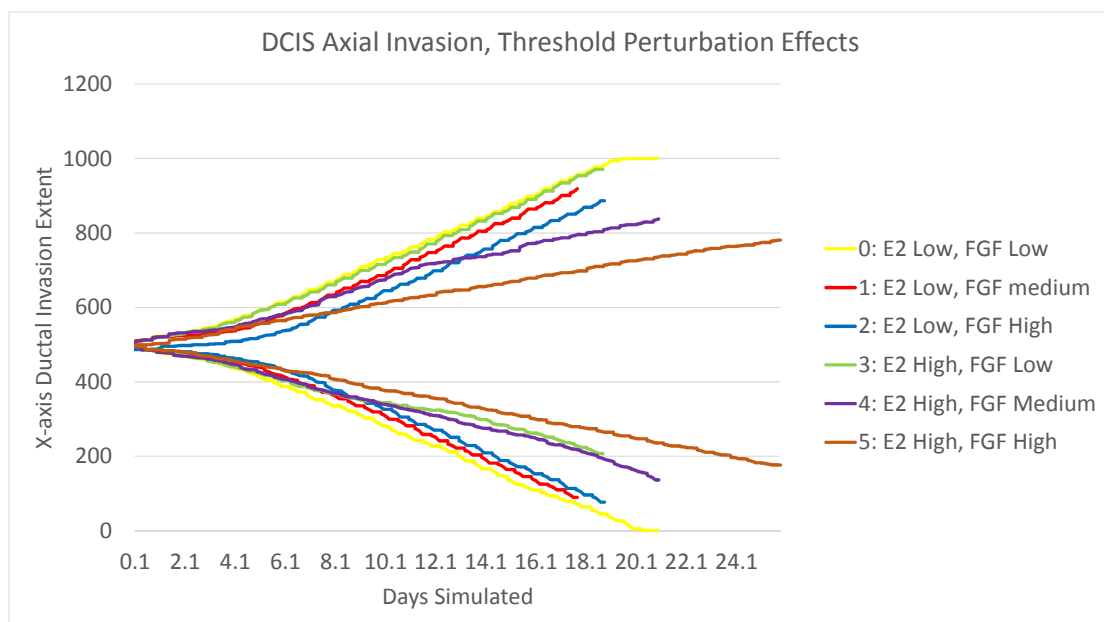


Figure 7.8: Effects of molecular signaling thresholds on DCIS axial invasion. Molecular signaling thresholding effects show a significant reduction in cell proliferation events and associated DCIS Axial invasion, with high thresholds showing the most effect. Estrogen thresholding is seen to have a more significant effect, as estrogen upregulates ER+ cell proliferation, which are directly responsible for increasing AREG and FGF concentrations in the duct above normal background levels (produced by ER+ cells in the mature duct luminal layer). Case 0 provides a baseline (i.e. without thresholding effects). All results shown are for a 100 μ m diameter duct.

Simulation output from several cases of interest (corresponding to the data shown in **Figure 7.8**) is shown in **Figure 7.9**. An example of a non-threshold limited case is shown in **Figure 7.9A**, with a cross-sectional view (cross-section taken vertically along the duct

axis) shown to show the phenotypic distribution internally within the DCIS mass. In this case, it can be seen that the viable rim on the right is completely composed of ER– phenotype, resulting in a large section of completely ER– agents, while the left side is

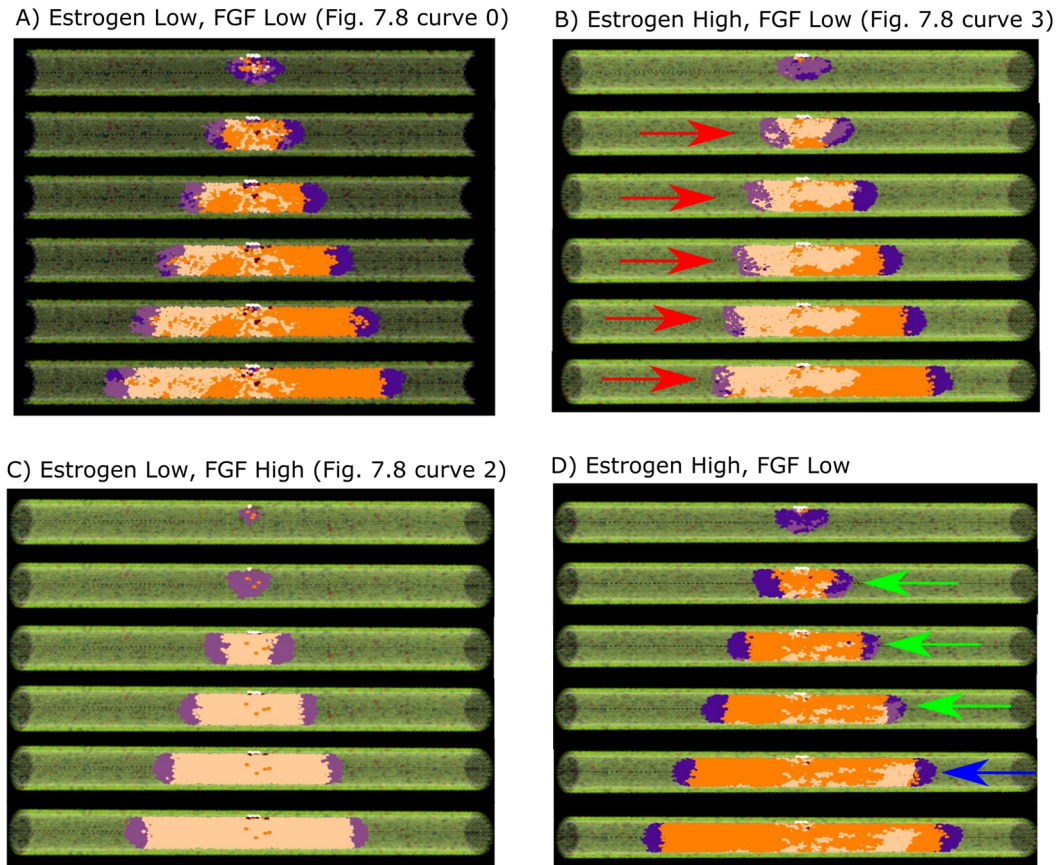


Figure 7.9: Example simulation results with signaling effects. A) Baseline example without signaling limited proliferation. B) Estrogen-limited case; the ER+ viable rim (red arrows) is seen to advance more slowly than the ER– (right side) viable rim due to estrogen limited ER+ proliferation. C) FGF limited proliferation; in this case, the ER– population is completely unable to proliferate at early model times, resulting in the viable rim being completely composed of ER+ cells, resulting in almost the entire DCIS population being an ER+ phenotype. D) Mixed viable rim (green arrows) is seen to overcome the proliferation limited ER+ population (due to high estrogen threshold), resulting in an ER+ viable rim (blue arrow) and demonstrating a possible adaptation mechanism to signaling limited cases in the DCIS cancer population. All results shown in a 100um duct; cases A-C correspond to curves shown in **Figure 7.8** (as indicated), data for D not shown. Time (descending) for each image in each case shown is 4, 6, 8, 10, 12, and 14 days after the EMT initiation event.

observed to be of mixed phenotype due to the mixed phenotypic distribution within the viable rim. We emphasize that due to the stochastic nature of the model, this is only one possible outcome, and it is also possible to see mixed phenotypes throughout, or even dominance of almost completely one phenotype, even without any molecular signaling thresholding effects in place, but derived exclusively from the stochastic nature of phenotypic selection in the model (data not shown).

Figure 7.9B shows a case of high estrogen thresholding; in this case, the ER⁺ dominated viable rim (red arrows) is substantially limited in axial advance rate due to high estrogen uptake in this area (many ER⁺ cells lower the local estrogen concentration in this region), while the ER⁻ viable rim (right side) shows substantially faster axial invasion due to low sensitivity to FGF signaling. Of note, the ER⁺ dominated viable rim is not completely arrested in proliferation events, as estrogen may diffuse down the duct (in the direction of the red arrows) from a higher estrogen concentration farther down the duct axis (where there are no ER⁺ DCIS cells), which maintains some limited proliferation at this location. **Figure 7.9C** shows a case of high FGF proliferation thresholds; in this case, the DCIS population is dominated by the ER⁺ phenotype, likely due to early stage establishment of a completely ER⁺ viable rim early in the simulation.

Lastly, **Figure 7.9D** shows a case of a mixed phenotype viable rim (green arrows), in the case of a high estrogen threshold (measurement data from this test is not shown). In this case, the viable rim was able to adapt to the threshold limitations. The ER⁻ phenotype, while not limited by the high estrogen threshold, and further stimulated into proliferation by AREG production in the adjacent ER⁺ population (through the AREG → FGF epithelial to stromal pathway), overtook the ER⁺ population in this case, and thus transitioned to a

viable rim of only the phenotype not limited by signaling thresholds (ER-, blue arrow). This suggests that the mixture of phenotypes of DCIS may serve as a tumor adaptation mechanism, allowing for tumor progression even when conditions are unfavorable for one or more phenotypes.

V. Discussion

Our model has shown good agreement with biologically reported values in the results presented, which we take to be affirmative evidence of its accurate replication of the disease state and predictive potential. With the model calibrated as presented, we note that the early exponential growth state of the disease is short-lived, with a rapid transition to a linear growth behavior. Clinically, the early stages of DCIS are hypothesized to be subdivided into hyperplasia and atypical hyperplasia, before transition to a full DCIS state [4]. Due to the short duration our model remains in the exponential growth phase, we justify our decision to lump all into our definition of DCIS, as the transition through the early stages was observed to occur rapidly.

We observed that the initial number of stem cells produced by an EMT transition at time $t=0$ only affected DCIS population dynamics at early times after the initial DCIS invasion event. This effect is due to the cell density limitations we impose on the system. At early times after DCIS initiation, an exponential growth is observed; at this time, the CSC number serves as the base of the exponential behavior, and has a direct influence on the rate of DCIS population increase. However, once the population reaches a cell number and density where proliferation becomes density-restricted, the early effects of the CSC niche on DCIS cell population are significantly reduced. This effect is contingent on all

CSCs occurring within a single niche, however; when multiple CSC niches are initiated apart from one another along the duct axis, this effect is mitigated until the DCIS populations resulting from each niche grow together into a confluent tumor (data not shown).

Cell density limits both the proliferation events within the CSC niche, as well as in the DCIS population located within the duct cavity. Under these conditions, DCIS invasion becomes primarily a function of proliferation events within the leading edge of the tumor, where cell density is lowest (due to the cell-free region in the duct opposite the DCIS mass, where the tumor has not yet invaded). This is opposed to early times after DCIS initiation, where the cell population may undergo a true population doubling each cell cycle (exponential growth), until cell density effects arrest this behavior. Subsequent to the exponential growth phase, DCIS axial invasion is accomplished through proliferation events in the leading edge of the tumor. This results in a linear duct invasion rate, at the leading edge remains of a somewhat consistent thickness, and may thus invade at most its own thickness per cell cycle, provided all progenitors in the leading edge undergo mitosis in a cell cycle. Because cell density is similar in all duct sizes (i.e. a cell on the absolute leading edge of the tumor may be completely surrounded by cells in the direction of the main tumor mass, while completely devoid of neighbors in the opposite axial direction, and in this case may experience ~50% neighboring cell density), the viable rim (under the same density conditions in all duct diameters) is of a similar number of cell layers thick in all duct diameters. This results in a consistent axial duct invasion rate in all diameters tested, but a larger total population increase in a larger duct due to the larger number of cells required to advance the tumor the same distance through a larger volume.

Necrosis functions as a relief mechanism for hypoxic conditions in the tumor, allowing a slight rebound of local oxygen concentration subsequent to necrotic cell death. In the tumor, this likely plays a key role in the natural selection mechanism for a hypoxia-resistant phenotype, where hypoxia-resistant cells are able to outlast the necrotic transition of their hypoxia-susceptible neighbors long enough to benefit from this transition. We note that we assume an equal rate of diffusion in the calcified region (and region of spilled but not yet calcified cytoplasmic contents) in this work – this is likely an overestimate, as oxygen diffusion is expected to be significantly reduced through hydroxyapatite. This will further reduce the hypoxic conditions, as oxygen is not lost to diffusion in regions of calcification (although we note that, due to lack of oxygen consumption in this location, the oxygen concentration profile reaches a steady-state in the calcified region in our model, and thus this effect may not be significant over time). Interestingly, we observe a predictable, regular distance between the extent of calcification (as would be seen in diagnostic tools in a patient, i.e. mammography) and the leading edge of the tumor. This may allow us to make predictions of an effective surgical margin around ducts where calcification is observed with our future modeling efforts.

Molecular signaling thresholds functioned as expected, with high thresholds limiting proliferation in the associated phenotype. Of particular interest, as shown in in **Figure 7.9C**, the DCIS was seen to be completely composed of the ER⁺ phenotype. Although there are ER⁻ cells near the CSC niche, proliferation at early times in the ER⁺ population resulted in the viable rim being completely composed of ER⁺ cells, and thus they advance the tumor into a completely ER⁺ phenotype. This ER⁺ population produced AREG, and thus the local FGF concentrations were plentiful to allow for ER⁻ phenotype

proliferation, but this did not occur as there were none of this phenotype in the leading edge. This demonstrates an important concept: *early molecular signing thresholds (or other events early in the DCIS initiation) play an important role in establishing the phenotypes found in the tumor leading edge.* If the leading edge is only composed of one phenotype after this period, then the DCIS advanced by these cells will be only this phenotype, even if the molecular signaling would support proliferation in the other phenotype at this location. This indicates that it is likely that future phenotypic diversity in the DCIS population may be due to further mutations within the cancer phenotype, or may also be due to de-differentiation events. It is established that de-differentiation events do occur in mammary cancers (i.e. a cell becomes less differentiated, potentially back to a stem-like phenotype) [52], although at this stage we do not include this phenomena in our model.

Even more interesting is the tumor adaptation effect observed in **Figure 7.9D**. In this case, one phenotype becomes dominant when a selective pressure results in reduced proliferation in the other phenotype. In this way, the tumor may adapt to be better suited to survival in its host – likely with ER+ favored in environments with high estrogen production, and ER– in cases of higher FGF signaling. Because estrogen functions through a system-wide endocrine mechanism, but FGF is a function of the local stroma, these two signaling pathways may experience different disruptions in a host, and these may favor one phenotype, analogous to sensitivity mutations in the different cell phenotypes in our model. Although this may potentially serve as a tumor adaptation mechanism, it does so at a cost as currently implemented in our model – it costs the tumor the phenotypic diversity that allowed it to make the adaptation, making it impossible for the viable rim to adapt back in

our model should molecular concentrations shift to favor the opposite phenotype. This effect could be overcome by a phenotypic plasticity mechanism (such as a de-differentiation pathway, resulting in more cancer stem-type cells), or by chemotaxis effects. In our next modeling work, we will add these effects to this model (among other) to further test this hypothesis, as well as comparing our results to *in vivo* animal data and studying a transition from an *in situ* cancer to an invasive cancer.

Model Parameter	Baseline Value	Reference
Hypoxia threshold	1/3 normoxia	[39, 44]
D_{oxygen}	$2.5 \times 10^{-6} \text{cm}^2 \text{s}^{-1}$	[37]
Blood oxygen concentration	100 mmHg	[39]
D_{estrogen}	$2.45 \times 10^{-6} \text{cm}^2 \text{s}^{-1}$	*
D_{AREG}	$3.18 \times 10^{-7} \text{cm}^2 \text{s}^{-1}$	[53]**
Proliferation rate	≤ 1 per 16 hours	
Cell cycle time	16 hours	[54, 55]
Progenitor symmetric proliferation	100%	
Proliferation cycles before differentiation	50	[41, 42]
Stem cell symmetric proliferation probability	12%	[56]
Spontaneous differentiation probability	0.0	
Mature mammary cell radius	$5 \mu\text{m}$	[38, 55]
Healthy cell oxygen uptake rate	$45 \text{attoMol} \cdot \text{cell}^{-1} \cdot \text{sec}^{-1}$	[38]
Cancer cell oxygen uptake rate	4.5x healthy cell rate	[38]
Hypoxia time to necrosis	12 hours	[45]
Lysis volume increase due to swelling	100%	[48, 49]
Lysis time	6 hours	[46]
Calcified volume % of pre-lysis cell volume	30%	[50]

Table 7.1: Important model parameter baseline values. When not readily available in the literature, diffusion constants were estimated either through interpolation from values from structurally similar molecules (*) or from known values based on relative molecular weights (**). Other uncited values were determined from model calibration. We have reduced the value for stem cell symmetric proliferation by 1% from [56].

VI. Acknowledgements

We graciously thank M. Lewis and J. Rosen (Baylor College of Medicine), J. Lowengrub (UC Irvine), and Y-L. Chuang (California State University, Northridge). We also acknowledge support from the Methodist Hospital Research Institute (V.C.).

Conflicts of Interest Disclosures

The authors declare no conflicts of interest.

VII. Works Cited, Chapter 7

1. U.S. Cancer Statistics Working Group. *United States Cancer Statistics: 1999–2013 Incidence and Mortality Web-based Report*. 2016; Available from: www.cdc.gov/uscs.
2. Allegra, C.J., Aberle, D.R., Ganschow, P., Hahn, S.M., Lee, C.N., Millon-Underwood, S., Pike, M.C., Reed, S.D., Saftlas, A.F., Scarvalone, S.A., Schwartz, A.M., Slomski, C., Yothers, G., and Zon, R., *NIH state-of-the-science conference statement: diagnosis and management of ductal carcinoma in situ (DCIS)*. NIH Consens State Sci Statements, 2009. **26**(2): p. 1-27.
3. SA, F., *Dynamics of Cancer: Incidence, Inheritance, and Evolution*. 2007, Princeton (NJ): Princeton University Press.
4. Liao, Y., *Cancer, stem cell misplacement and cancer stem cells*. Journal of Cellular and Molecular Medicine, 2013. **17**(9): p. 1194-1195.
5. Rios, A.C., Fu, N.Y., Lindeman, G.J., and Visvader, J.E., *In situ identification of bipotent stem cells in the mammary gland*. Nature, 2014. **506**(7488): p. 322-327.
6. Villadsen, R., Fridriksdottir, A.J., Ronnov-Jessen, L., Gudjonsson, T., Rank, F., LaBarge, M.A., Bissell, M.J., and Petersen, O.W., *Evidence for a stem cell hierarchy in the adult human breast*. J Cell Biol, 2007. **177**(1): p. 87-101.
7. Sternlicht, M.D., Sunnarborg, S.W., Kouros-Mehr, H., Yu, Y., Lee, D.C., and Werb, Z., *Mammary ductal morphogenesis requires paracrine activation of stromal EGFR via ADAM17-dependent shedding of epithelial amphiregulin*. Development, 2005. **132**(17): p. 3923-33.
8. Sternlicht, M.D. and Sunnarborg, S.W., *The ADAM17-amphiregulin-EGFR axis in mammary development and cancer*. J Mammary Gland Biol Neoplasia, 2008. **13**(2): p. 181-94.
9. Gjorevski, N. and Nelson, C.M., *Integrated morphodynamic signalling of the mammary gland*. Nat Rev Mol Cell Biol, 2011. **12**(9): p. 581-93.
10. Mailleux, A.A., Spencer-Dene, B., Dillon, C., Ndiaye, D., Savona-Baron, C., Itoh, N., Kato, S., Dickson, C., Thiery, J.P., and Bellusci, S., *Role of FGF10/FGFR2b signaling during mammary gland development in the mouse embryo*. Development, 2002. **129**(1): p. 53-60.
11. Lu, P., Ewald, A.J., Martin, G.R., and Werb, Z., *Genetic mosaic analysis reveals FGF receptor 2 function in terminal end buds during mammary gland branching morphogenesis*. Developmental biology, 2008. **321**(1): p. 77-87.
12. Turner, N. and Grose, R., *Fibroblast growth factor signalling: from development to cancer*. Nat Rev Cancer, 2010. **10**(2): p. 116-129.
13. Parsa, S., Ramasamy, S.K., De Langhe, S., Gupte, V.V., Haigh, J.J., Medina, D., and Bellusci, S., *Terminal end bud maintenance in mammary gland is dependent upon FGFR2b signaling*. Dev Biol, 2008. **317**(1): p. 121-31.
14. Pasic, L., Eisinger-Mathason, T.S., Velayudhan, B.T., Moskaluk, C.A., Brenin, D.R., Macara, I.G., and Lannigan, D.A., *Sustained activation of the HER1-ERK1/2-RSK signaling pathway controls myoepithelial cell fate in human mammary tissue*. Genes Dev, 2011. **25**(15): p. 1641-53.

15. Chepko, G. and Smith, G.H., *Three division-competent, structurally-distinct cell populations contribute to murine mammary epithelial renewal*. Tissue Cell, 1997. **29**(2): p. 239-53.
16. Dobrescu, A., Chang, M., Kirtani, V., Turi, G.K., Hennawy, R., and Hindenburg, A.A., *Study of Estrogen Receptor and Progesterone Receptor Expression in Breast Ductal Carcinoma In Situ by Immunohistochemical Staining in ER/PgR-Negative Invasive Breast Cancer*. ISRN Oncology, 2011. **2011**: p. 673790.
17. Malafa, M., Chaudhuri, B., Thomford, N.R., and Chaudhuri, P.K., *Estrogen receptors in ductal carcinoma in situ of breast*. Am Surg, 1990. **56**(7): p. 436-9.
18. Moerkens, M., Zhang, Y., Wester, L., van de Water, B., and Meerman, J.H.N., *Epidermal growth factor receptor signalling in human breast cancer cells operates parallel to estrogen receptor α signalling and results in tamoxifen insensitive proliferation*. BMC Cancer, 2014. **14**: p. 283-283.
19. Bouris, P., Skandalis, S.S., Piperigkou, Z., Afratis, N., Karamanou, K., Aletras, A.J., Moustakas, A., Theocharis, A.D., and Karamanos, N.K., *Estrogen receptor α mediates epithelial to mesenchymal transition, expression of specific matrix effectors and functional properties of breast cancer cells*. Matrix Biol, 2015. **43**: p. 42-60.
20. Espina, V. and Liotta, L.A., *What is the malignant nature of human ductal carcinoma in situ?* Nat Rev Cancer, 2011. **11**(1): p. 68-75.
21. Wang, Z., Butner, J.D., Kerketta, R., Cristini, V., and Deisboeck, T.S., *Simulating cancer growth with multiscale agent-based modeling*. Semin Cancer Biol, 2015. **30**: p. 70-8.
22. Wang, Z., Kerketta, R., Chuang, Y.L., Dogra, P., Butner, J.D., Brocato, T.A., Day, A., Xu, R., Shen, H., Simbawa, E., Al-Fhaid, A.S., Mahmoud, S.R., Curley, S.A., Ferrari, M., Koay, E.J., and Cristini, V., *Theory and Experimental Validation of a Spatio-temporal Model of Chemotherapy Transport to Enhance Tumor Cell Kill*. PLoS Comput Biol, 2016. **12**(6): p. e1004969.
23. Anderson, A.R., Chaplain, M.A., and Rejniak, K.A., *Single-Cell-Based Models in Biology and Medicine*. 1 ed. Mathematics and Biosciences in Interaction. 2007, Switzerland: Birkhäuser Basel. 349.
24. Boghaert, E., Radisky, D.C., and Nelson, C.M., *Lattice-based model of ductal carcinoma in situ suggests rules for breast cancer progression to an invasive state*. PLoS Comput Biol, 2014. **10**(12): p. e1003997.
25. Bankhead, A., 3rd, Magnuson, N.S., and Heckendorn, R.B., *Cellular automaton simulation examining progenitor hierarchy structure effects on mammary ductal carcinoma in situ*. J Theor Biol, 2007. **246**(3): p. 491-8.
26. Tang, J., Fernandez-Garcia, I., Vijayakumar, S., Martinez-Ruis, H., Illa-Bochaca, I., Nguyen, D.H., Mao, J.H., Costes, S.V., and Barcellos-Hoff, M.H., *Irradiation of juvenile, but not adult, mammary gland increases stem cell self-renewal and estrogen receptor negative tumors*. Stem Cells, 2014. **32**(3): p. 649-61.
27. Edgerton, M.E., Chuang, Y.L., Macklin, P., Yang, W., Bearer, E.L., and Cristini, V., *A novel, patient-specific mathematical pathology approach for assessment of surgical volume: application to ductal carcinoma in situ of the breast*. Anal Cell Pathol (Amst), 2011. **34**(5): p. 247-63.

28. Xu, Y. and Gilbert, R., *Some inverse problems raised from a mathematical model of ductal carcinoma in situ*. Mathematical and Computer Modelling, 2009. **49**(3–4): p. 814-828.
29. Hyun, A.Z. and Macklin, P., *Improved patient-specific calibration for agent-based cancer modeling*. J Theor Biol, 2013. **317**: p. 422-4.
30. Macklin, P., Edgerton, M.E., Thompson, A.M., and Cristini, V., *Patient-calibrated agent-based modelling of ductal carcinoma in situ (DCIS): from microscopic measurements to macroscopic predictions of clinical progression*. J Theor Biol, 2012. **301**: p. 122-40.
31. Shumate, S.D. and El-Shenawee, M., *Computational model of ductal carcinoma in situ: the effects of contact inhibition on pattern formation*. IEEE Trans Biomed Eng, 2009. **56**(5): p. 1341-7.
32. Gatenby, R.A., Smallbone, K., Maini, P.K., Rose, F., Averill, J., Nagle, R.B., Worrall, L., and Gillies, R.J., *Cellular adaptations to hypoxia and acidosis during somatic evolution of breast cancer*. British Journal of Cancer, 2007. **97**(5): p. 646-653.
33. Butner, J.D., Chuang, Y.L., Simbawa, E., Al-Fhaid, A.S., Mahmoud, S.R., Cristini, V., and Wang, Z., *A hybrid agent-based model of the developing mammary terminal end bud*. J Theor Biol, 2016. **407**: p. 259-70.
34. Long, K., Kirby, R., and Waanders, B.v.B., *Unified Embedded Parallel Finite Element Computations via Software-Based Fréchet Differentiation*. SIAM J. Sci. Comput., 2010. **32**(6): p. 3323-3351.
35. Sharma, N. and Jeong, D.K., *Stem cell research: a novel boulevard towards improved bovine mastitis management*. Int J Biol Sci, 2013. **9**(8): p. 818-29.
36. MacDougall, J.D. and McCabe, M., *Diffusion coefficient of oxygen through tissues*. Nature, 1967. **215**(5106): p. 1173-4.
37. Sidell, B.D., *Intracellular oxygen diffusion: the roles of myoglobin and lipid at cold body temperature*. Journal of Experimental Biology, 1998. **201**(8): p. 1119-1128.
38. Wagner, B.A., Venkataraman, S., and Buettner, G.R., *The Rate of Oxygen Utilization by Cells*. Free radical biology & medicine, 2011. **51**(3): p. 700-712.
39. Carreau, A., El Hafny-Rahbi, B., Matejuk, A., Grillon, C., and Kieda, C., *Why is the partial oxygen pressure of human tissues a crucial parameter? Small molecules and hypoxia*. J Cell Mol Med, 2011. **15**(6): p. 1239-53.
40. Courant, F., Aksglaede, L., Antignac, J.P., Monteau, F., Sorensen, K., Andersson, A.M., Skakkebaek, N.E., Juul, A., and Bizec, B.L., *Assessment of circulating sex steroid levels in prepubertal and pubertal boys and girls by a novel ultrasensitive gas chromatography-tandem mass spectrometry method*. J Clin Endocrinol Metab, 2010. **95**(1): p. 82-92.
41. Wang, J., Hannon, G.J., and Beach, D.H., *Cell biology: Risky immortalization by telomerase*. Nature, 2000. **405**(6788): p. 755-756.
42. Wang, J., Xie, L.Y., Allan, S., Beach, D., and Hannon, G.J., *Myc activates telomerase*. Genes Dev, 1998. **12**(12): p. 1769-74.
43. Mayr, N.A., Staples, J.J., Robinson, R.A., Vanmetre, J.E., and Hussey, D.H., *Morphometric studies in intraductal breast carcinoma using computerized image analysis*. Cancer, 1991. **67**(11): p. 2805-12.

44. Hockel, M. and Vaupel, P., *Biological consequences of tumor hypoxia*. Semin Oncol, 2001. **28**(2 Suppl 8): p. 36-41.
45. Steinbach, J.P., Wolburg, H., Klumpp, A., Probst, H., and Weller, M., *Hypoxia-induced cell death in human malignant glioma cells: energy deprivation promotes decoupling of mitochondrial cytochrome c release from caspase processing and necrotic cell death*. Cell Death Differ, 2003. **10**(7): p. 823-832.
46. Majno, G. and Joris, I., *Apoptosis, oncosis, and necrosis. An overview of cell death*. Am J Pathol, 1995. **146**(1): p. 3-15.
47. Groulx, N., Boudreault, F., Orlov, S.N., and Grygorczyk, R., *Membrane reserves and hypotonic cell swelling*. J Membr Biol, 2006. **214**(1): p. 43-56.
48. Wu, L.-Y., Ma, Z.-M., Fan, X.-L., Zhao, T., Liu, Z.-H., Huang, X., Li, M.-M., Xiong, L., Zhang, K., Zhu, L.-L., and Fan, M., *The anti-necrosis role of hypoxic preconditioning after acute anoxia is mediated by aldose reductase and sorbitol pathway in PC12 cells*. Cell Stress & Chaperones, 2010. **15**(4): p. 387-394.
49. Gronroos, M., Chen, M., Jahnukainen, T., Capitanio, A., Aizman, R.I., and Celsi, G., *Methotrexate induces cell swelling and necrosis in renal tubular cells*. Pediatr Blood Cancer, 2006. **46**(5): p. 624-9.
50. Luby-Phelps, K., *Cytoarchitecture and physical properties of cytoplasm: volume, viscosity, diffusion, intracellular surface area*. Int Rev Cytol, 2000. **192**: p. 189-221.
51. (TACC), T.A.C.C., The University of Texas at Austin
52. Chaffer, C.L., Brueckmann, I., Scheel, C., Kaestli, A.J., Wiggins, P.A., Rodrigues, L.O., Brooks, M., Reinhardt, F., Su, Y., Polyak, K., Arendt, L.M., Kuperwasser, C., Bierie, B., and Weinberg, R.A., *Normal and neoplastic nonstem cells can spontaneously convert to a stem-like state*. Proceedings of the National Academy of Sciences of the United States of America, 2011. **108**(19): p. 7950-7955.
53. Thorne, R.G., Hrabetova, S., and Nicholson, C., *Diffusion of epidermal growth factor in rat brain extracellular space measured by integrative optical imaging*. J Neurophysiol, 2004. **92**(6): p. 3471-81.
54. Brummer, T., Schramek, D., Hayes, V.M., Bennett, H.L., Caldon, C.E., Musgrove, E.A., and Daly, R.J., *Increased proliferation and altered growth factor dependence of human mammary epithelial cells overexpressing the Gab2 docking protein*. J Biol Chem, 2006. **281**(1): p. 626-37.
55. Paine, I., Chauviere, A., Landua, J., Sreekumar, A., Cristini, V., Rosen, J., and Lewis, M.T., *A Geometrically-Constrained Mathematical Model of Mammary Gland Ductal Elongation Reveals Novel Cellular Dynamics within the Terminal End Bud*. PLoS Comput Biol, 2016. **12**(4): p. e1004839.
56. Giebel, B., Zhang, T., Beckmann, J., Spanholtz, J., Wernet, P., Ho, A.D., and Punzel, M., *Primitive human hematopoietic cells give rise to differentially specified daughter cells upon their initial cell division*. Blood, 2006. **107**(5): p. 2146-52.

CHAPTER 8

Conclusions and Future Directions

Over the last chapters, we have examined several examples of hybrid, multiscale models of the mammary gland system, applied to both pubertal development and to study of a stage zero breast cancer, ductal carcinoma in situ. These models were implemented in a biologically inspired order, following the natural pattern of starting with early-life development followed by a subsequent later in life transition to a disease state. We gained valuable insights into quantified parameters and behaviors at the sub-organ scale, which were implemented in each subsequent modeling step to more fully and correctly describe the behaviors of interest. At each step, the new or improved model was validated against the literature through comparison of model output to other, independent literature-reported quantities, unrelated to model inputs. This important step lends validity to the model and the quantities and assumptions included. A model's ability to take a set of underlying biological rules and principles, and by combining them through sound mathematical and quantitative relations, to then solve for a quantity independent of (but related to) these values demonstrates the biological relevance of model assumptions and predictions.

In the case of the models presented here, both TEB models were able to take a set of rules for cell phenotypic hierarchies, biologically supported statistical information about the dynamics of cell proliferation probabilities, and molecular signaling pathways, and then combine these rules together to accurately reproduce biologically relevant duct elongation rates and cell phenotype distributions within the mature duct. Likewise, the DCIS model

was able to successfully reproduce DCIS axial invasion rates using a similar set of rules. This approach is analogous to the biological system being studied – a set of molecular, sub-cellular, and cell-scale rules, when combined together under the proper conditions, leads to the biological result of the development of the tissue (TEB) or disease state (DCIS). In this way, models are validated through their successful ability to reproduce both the sub-processes and the associated overall system-wide (in this case, taking the system to be the tissue of interest) behavior, as observed in nature. Indeed, this biologically relevant connection between model inputs and the resultant output is as should be expected, and provides validation of the rules and mathematical implementations chosen by the modelers, through demonstration of successful reproduction of known biological quantities.

The ability of mathematical models to replicate system-wide biological behaviors based on an equation based representation of the underlying mechanisms in the system suggests further power in the field of mathematical modeling, however: the ability to be used as a predictive tool of system response to both internal perturbations and external stimuli. This step requires absolute certainty in the reliability of the model, and mandates thorough testing of the model against biological data. In the models presented in this work, validation against literature-supported data was successfully achieved, but our efforts were limited by the quantified values we found already existent in the literature. To address this shortcoming, we are currently building relationships with wet-lab researchers, who will be able to design and conduct experiments in order to help provide needed quantification of variables in the models, provide expertise on the biological system (e.g. which important biological factors should be added to the models, and what resultant behaviors we should hope to observe). Specifically, these relationships will include increased access to animal

model data, quantified measurements of quiescent vs. proliferative states, as well as animal model data on early stage DCIS. This interaction will lend greater validity, accuracy, and predictive power to our models, while simultaneously allowing us to provide new insights we observe in simulation results for validation in a living system.

This collaborative effort will prove beneficial to both sides, and hopefully allow our models to receive sufficient validation to be implemented as predictive tools. One exciting avenue in this direction is in the area of DCIS treatment, which is now accomplished through a combination of surgical resection and other treatment methods, including post-surgical radiation therapy. Significant progress has been made in targeting the ER+ breast cancer (e.g. tamoxifen, aromatase inhibitors), resulting in more positive prognosis in ER+ breast cancers relative to cancers negative for these receptors, and HER2+ tumors may also be targeted, e.g. trastuzumab (although this pathway is not included in this study, we mention it here for sake of completeness). However, such novel treatments for the triple negative breast cancer phenotype have remained elusive, resulting in unfavorable patient prognosis relative to ER+ and HER2+ cases. Insights into the interplay of signaling mechanisms and the resultant phenotypic distribution within the DCIS population may allow the tumor to be “tuned” through novel treatment methods to a phenotype that has a more favorable response to these therapies. Likewise, further insights into the relationship between DCIS calcification (as obtainable through standard diagnostic methods, e.g. mammography) and the full tumor extent may help increase precision in surgical margins, allowing for greater reliability of complete surgical resection while minimizing patient trauma and treatment impact. Subsequent to further model validation, we will explore these areas (among others) in order to shed new light onto quantified

parameters of interest, with the goal of clinically relevant discoveries that may help improve treatment and patient outcomes.